Lidar and Satellite Studies of Noctilucent Clouds over Alaska

Jennifer H. Alspach

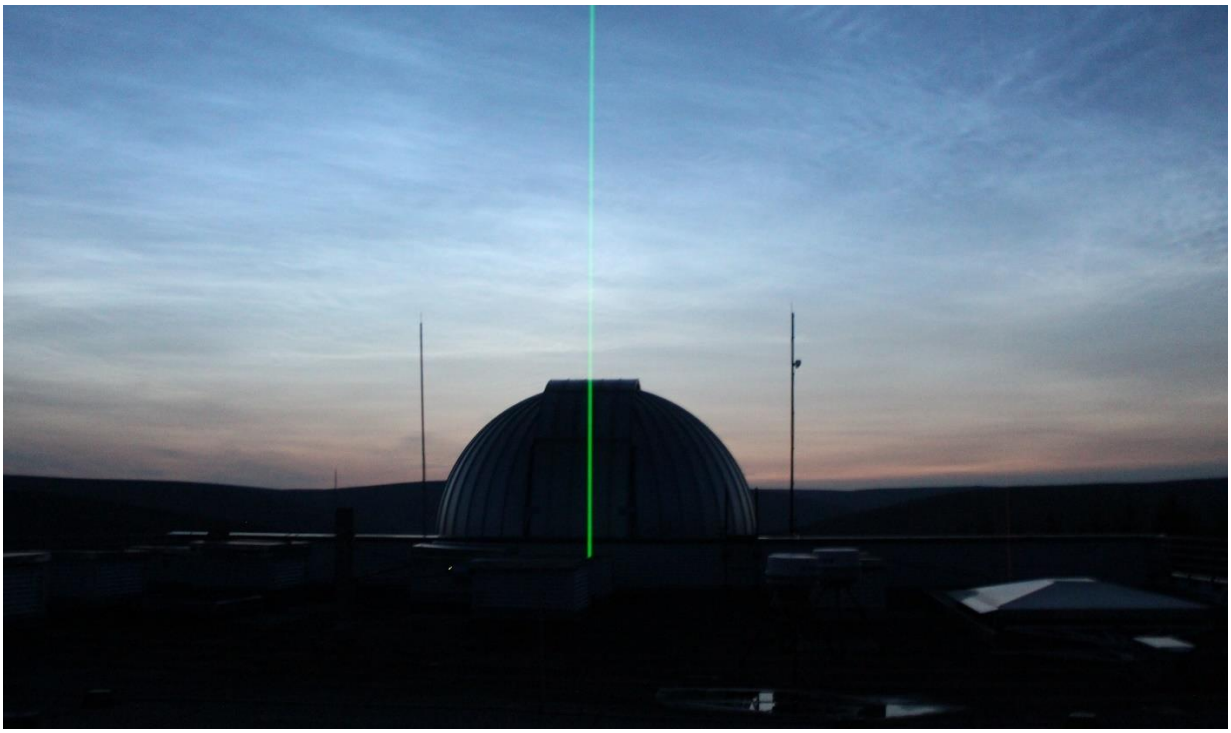

An M.S. Thesis
Department of Atmospheric Sciences
And Geophysical Institute
University of Alaska Fairbanks

May 2020

LIDAR AND SATELLITE STUDIES OF NOCTILUCENT CLOUDS OVER ALASKA

By

Jennifer Alspach, B.S.

A Thesis Submitted in Partial Fulfillment of the Requirements

for the Degree of

Masters of Science

in

Atmospheric Sciences

University of Alaska Fairbanks

May 2020

APPROVED:

Dr. Richard Collins, Committee Chair
Dr. Katrina Bossert, Committee Member
Dr. Denise Thorsen, Committee Member
Dr. Javier Fochesatto, Committee Member, Chair
Department of Atmospheric Sciences
Dr. Kinchel Doerner, Dean
College of Natural Science and Mathematics
Dr. Michael Castellini, Dean
The Graduate School

Abstract

This thesis presents studies of noctilucent clouds (NLCs) occurring in the summer polar mesosphere over Alaska. Lidar observations of NLCs conducted at Poker Flat Research Range in Chatanika, Alaska (65° N, 147° W) from 1998-2019 are analyzed. The NLCs detected by lidar are characterized in terms of their brightness properties and duration. NLCs were detected on ~51% of the nights when lidar observations have been conducted during NLC season. The brighter NLCs are found to exist at lower altitudes, indicating a growth-sedimentation mechanism.

Cloud Imaging and Particle Size (CIPS) data from the Aeronomy of Ice in the Mesosphere (AIM) satellite is used to examine NLC occurrence and brightness over the Alaska region (60-70° N, 130-170° W). In general, high frequency and brightness in the CIPS data corresponds to positive detections of NLCs by the lidar.

Microwave Limb Sounder (MLS) temperature and water vapor data from the Aura satellite is used to investigate the meteorological environment of the NLCs observed by lidar at Chatanika. The occurrence of NLCs at Chatanika is found to be driven by the temperature relative to the frost point. Low temperatures relative to the frost point (> 4 K below) correspond to observations when NLCs were present. High temperatures relative to the frost point (> 8 K above) correspond to observations when NLCs were absent. The MLS data is also used to investigate the stability of an ice cloud at different latitudes (64.7°-70.3° N) relative to the equilibrium water vapor mixing ratio. The stability study suggests that the weakest NLCs detected by lidar at Chatanika were in subsaturated conditions, and it is likely that the NLCs formed over several hundred kilometers to the north of Chatanika.

The Rayleigh three-channel receiver system was used to conduct NLC measurements during 2019. A technical overview of the three-channel system and the density and temperature retrieval methods is presented at the end of the thesis using observations from the winter of 2018 and the summer of 2019.

Table of Contents

List of Figures

List of Tables

Acknowledgments

First, I would like to thank my adviser, Dr. Richard Collins, for his guidance and support. I very much appreciate the opportunities he has made available to me and for providing the hands-on research experience I had desired in coming to Alaska. I'm grateful and proud to have been a part of his lidar lab.

I thank my committee members, Dr. Javier Fochesatto, Dr. Denise Thorsen, and Dr. Katrina Bossert for all their helpful discussions, encouragement, and the time they dedicated to advising my work.

I thank the National Science Foundation for funding my research, and I thank the staff at Poker Flat Research Range for maintaining the range and supporting the work done at the lidar lab. I also thank Dr. Bifford Williams for his work during the observation campaigns at the lab.

I thank the UAF Department of Atmospheric Sciences faculty, staff, and students for being great people and creating an enjoyable place to work and study.

I thank MACS Transit for getting me to and from the University each day, mostly on time.

I thank my lab mate and friend, Dr. Jintai Li, for being a great mentor since my very first day in Alaska, for generously sharing his knowledge and time with me, and for the memories made during all our lidar adventures.

I thank my Fairbanks friends, especially Shannon Christensen and Martin Roach, for showing me the Alaskan way and for always being there for me. I also thank my friends from home for cheering me on from far. I especially thank my best friend, Alaric Bryant, for going on this long-distance adventure with me and encouraging me every day.

I thank my family for always sharing in the excitement of things I try to do. I especially thank my parents. I thank my mom, Irma Alspach, for all her prayers and for being a role model for hard work. I thank my dad, David Alspach, for the unwavering support he has given me all my life.

Finally, and most importantly, I thank God for the blessing of this life and so many incredible experiences in Alaska, especially the time I've gotten to spend studying and appreciating His highest clouds.

Chapter 1. Introduction

1.1. The Summer Polar Mesosphere

The mesosphere is the region in Earth's atmosphere from ~50-90 km that exists between the stratosphere and the thermosphere (Figure 1.1). The mesosphere exists in the homosphere where atmospheric constituents are well mixed by eddy processes. The air pressure at the bottom of the mesosphere is less than 1% of the sea level pressure. Temperature decreases with height in the mesosphere due to reduced solar heating which occurs from diminished ultraviolet absorption by ozone. Despite being referred to as the "ignorosphere" until recent years, the mesosphere is a region of many interesting dynamic processes, including the propagation of gravity waves, tides, and planetary waves [Morris and Murphy, 2008]. Topography and weather systems in the lower atmosphere induce gravity waves, or buoyancy waves, which propagate upward and grow in amplitude as they travel through the less dense middle atmosphere. The gravity waves eventually become unstable and break, depositing their momentum. Tidal waves arise with periods of 24, 12, 8, and 6 hours driven by solar heating of the atmosphere. Planetary waves are inertial waves that occur due to the rotation of the Earth and have periods of several days. Another feature of the mesosphere is the layer of metallic species that exist from the ablation of meteors. Very little water vapor exists in the mesosphere (a few ppmv) but, coupled with the thermodynamics that take place in the summer, a remarkable phenomenon arises.

In the summer, dynamic processes occur that result in a cooling in the mesosphere that exceeds the heating due to solar radiation [Morris and Murphy, 2008]. The mean

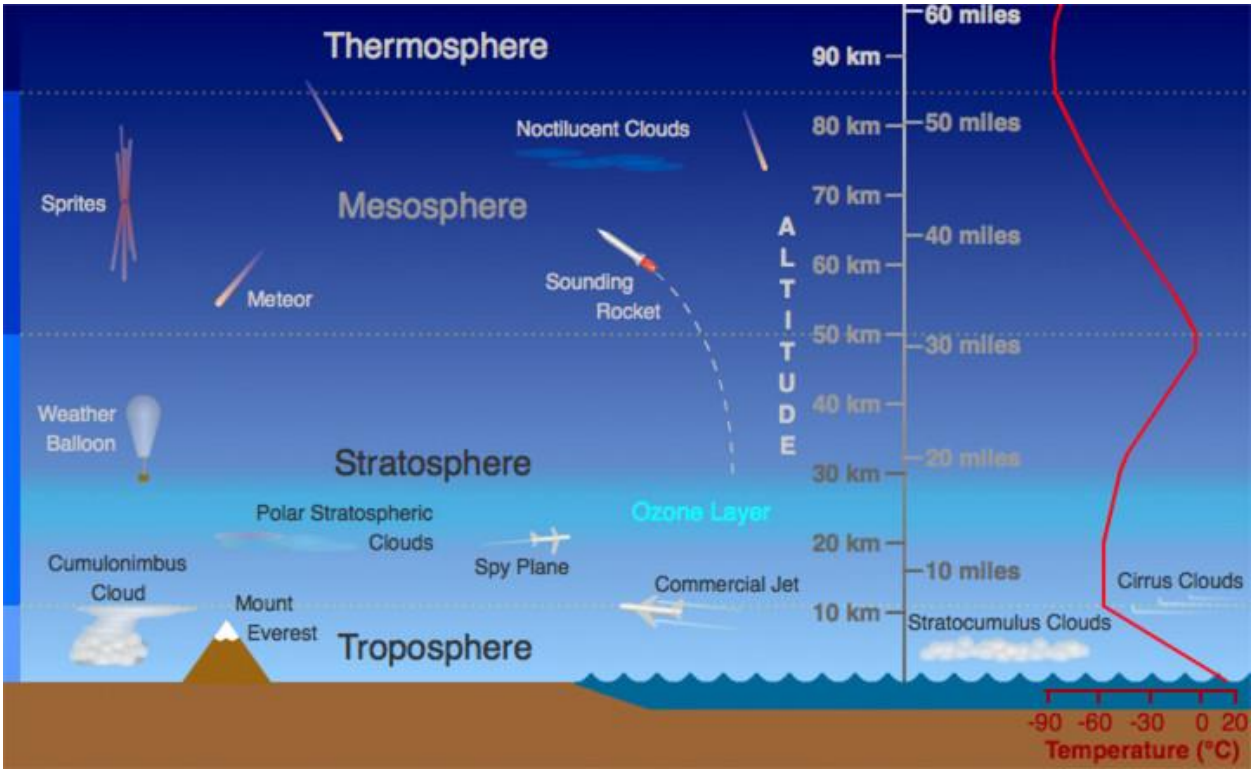

Figure 1.1. Layers of Earth's atmosphere. Taken from Russell, UCAR.

zonal wind direction reverses in the summer to a westward direction. The zonal westward wind predominantly filters out westward propagating gravity waves. The eastward propagating gravity waves that reach the mesosphere induce an eastward drag force upon their breaking. The eastward drag force results in a reduction and eventual reversal of the westward wind. Without the presence of gravity waves, the Coriolis force associated with the westward wind and the pressure gradient force would be in balance. However, due to the weakening of the westward wind by the eastward gravity wave drag force, the Coriolis force associated with the westward wind also weakens. The Coriolis force and the pressure gradient force become unbalanced, and this results in a net meridional circulation from the summer pole to the winter pole [Holton and Alexander, 2000]. The equatorward flow of air in the summer mesosphere drives a vertical upwelling

of air. The associated adiabatic cooling as the air rises in the mesosphere exceeds the heating due to solar radiation, resulting in an extremely cold summertime mesosphere. The mesospheric temperatures are coldest near the pole, where the equatorward flow of air and resulting uplift is greatest. In fact, the top edge of the polar mesosphere, termed the polar mesopause, is the coldest place in the entire Earth system with temperatures reaching below 130 K in the summer [Lübken, 1999]. The upwelling also transports water vapor from lower altitudes up into the mesosphere [Björn, 1984]. The extremely cold temperatures in the summer polar mesosphere enable the formation of ice crystals from the ambient water vapor, and the highest clouds in Earth's atmosphere are formed.

1.2. Noctilucent Clouds

1.2.1. Description

Noctilucent clouds (NLCs) are the highest clouds in Earth's atmosphere, occurring in the summer polar mesosphere at an altitude of about 83 km. These "night shining" clouds are named as such because they become visible to ground observers when the sun has descended below the horizon and the clouds become illuminated in the dark of twilight due to their high altitude and the sunlight scattering off the ice crystals. The lower atmosphere is in darkness while the NLCs become illuminated at their high altitude against a dark foreground. NLCs appear as tenuous, wispy features with a white or electric blue color and often exhibit wave-like structures. NLCs are typically visible when the sun is between 6-16° below the horizon [Fogle, 1966]. It is more difficult to distinguish NLC from cirrus clouds when the sun is less than 6° below the horizon. NLCs are also referred to as polar mesospheric clouds (PMCs), especially by the satellite community

since satellite instruments are not confined to the nighttime illumination and clear skies (free of tropospheric clouds) required for ground observations. NLCs are typically seen by ground observers between 50-70° latitude. The bright background sky that exists above the higher latitudes in the summertime makes it difficult for NLCs to be visible at these high latitudes, yet it is over the summer polar cap that the concentrated NLC mass exists throughout most of the summer [Donahue et al., 1972]. Patches of NLC can extend down to mid-latitudes and have been observed as far south as 42° N [Taylor et al., 2002].

Infrared measurements by the Halogen Occultation Experience (HALOE) confirmed that NLCs are composed of small crystals consisting of water ice [Hervig et al., 2001]. The ice crystals are typically less than 100 nm in radius. Lidar measurements have estimated the mean particle size of strong NLCs to be ~45-55 nm [Baumgarten et al. 2007]. Lidar cross-polarization experiments have discovered the presence of non-spherical particles in NLCs [Baumgarten et al., 2002]. The largest particles are seen near the bottom of the cloud layer (~80 km) and have radii up to 120 nm, but do not significantly contribute to the brightness of the cloud since they exist in small number densities. The brightest regions of the cloud are dominated by particle sizes between 50-70 nm which exist in large numbers [Hultgren and Gumbel, 2014].

1.2.2. Noctilucent Cloud Formation

Extremely cold temperatures are required for NLC formation due to the small concentrations of water vapor in the mesosphere. A temperature of 150 K has long been assumed as the threshold temperature for NLC formation [Theon et al., 1967]. It is below 150 K that mesospheric temperatures begin to reach below the frost point temperature

[Jensen and Thomas, 1994]. A thorough overview of the current knowledge of mesospheric ice particle formation has been established by Rapp and Thomas [2006]. Ice particle nucleation occurs near the altitude with the largest saturation ratio. This altitude is close to the temperature minimum at the mesopause which typically exists between 86-90 km. The saturation ratios at the temperature minimum are on the order of 100. Homogenous nucleation is considered highly unlikely in the summer mesosphere. The temperature requirement for homogenous nucleation is thought to be below 100 K, with greater than 10 ppmv of water vapor being required. Also, for homogenous nucleation to occur, the environment would have to be completely free of pre-existing aerosol particles. When nuclei are present, ice crystal formation through deposition on nuclei is highly preferred over homogenous nucleation [Rapp and Thomas, 2006]. Through a growth-sedimentation mechanism, the ice crystals grow in size through deposition of water onto the crystal as they descend due to gravity. Eventually, the ice crystals reach a warmer altitude when the crystals begin to sublimate. During the sedimentation, the ice particles are subject to mean winds, waves, and turbulence. Using the Community Aerosol and Radiation Model for Atmospheres (CARMA), modeling studies have suggested that the heaviest ice particles are subject to the growth-sedimentation mechanism and eventual sublimation, but that smaller particles may be transported upwards by the mean vertical wind [Rapp and Thomas, 2006]. The upward vertical wind can prolong the time that the ice crystal spends in the supersaturated region. Smaller particles exist in large numbers at the top of the cloud layer and a small number of large particles have been found to “rain out” of the cloud near the end of their life cycle. The fall speeds of these large particles enable them to fall well below the unsaturated

altitude region before sublimation [Hultgren and Gumbel, 2014]. It is important to remember that under the extremely cold temperatures and low pressure of the mesosphere, water is not expected to exist in the liquid phase. Phase transitions occur directly from gas to ice through deposition and from ice to gas through sublimation. Meteoric smoke particles are typically the nuclei of choice in almost all model studies of mesospheric ice particles [Rapp and Thomas, 2006].

1.2.3. Waves and Other Impacts

Planetary waves can produce strong disturbances to the background state of the mesosphere and therefore be an important driver for changes seen in NLC occurrence and brightness. NLC frequency of occurrence is strongly anti-correlated with fluctuations in temperature. Temperature fluctuations up to 8 K have been correlated to the probability of NLC occurrence [Kirkwood and Stebel, 2003]. The most important planetary waves for NLCs seem to be the 5-day and 2-day waves. The westward propagating 5-day wavenumber 1 (5DW1) planetary wave has been found to be the dominant wave present in the summer polar mesosphere in NLC and temperature signatures [Merkel et al., 2009]. The temperature amplitude of the 5DW1 wave is only up to about 3 K but corresponds to a significant change in NLC albedo of up to 3.6×10^{-6} sr^{-1} and an increase in cloud frequency of 22%. The 5DW1 occurs due to the reversal of the summertime jet. The westward propagating 2-day wavenumber 2 (2DW2) is also evident in temperature and NLC albedo and frequency signatures [Merkel et al., 2009].

NLC altitude, occurrence, and brightness as a function of solar time have found to be dominated by diurnal and semidiurnal tidal components. For NLC occurrence and

brightness, the diurnal tide is most important. For NLC altitude, both diurnal and semidiurnal components contribute about equally to the variability. Lidar observations over full diurnal cycles have shown that NLC occurrence is highest between midnight-6:00 local solar time (LST) and that the maximum NLC brightness is reached between 3:00-8:00 LST [Fiedler and Baumgarten, 2018].

NLC layers have been shown to occur in the cold phase of gravity waves [e.g. Collins et al., 2003]. Gravity wave activity has an impact on NLC depending on the phase of the wave. Short-period gravity waves with periods less than 6.5 hours tend to diminish NLC, while longer-period gravity waves have been shown to amplify NLC [Rapp et al., 2002]. This wave period effect is explained by the reduction in growth time that results when the crystals are rapidly transported downward out of the supersaturated altitude region and have not yet grown to a maximum size. Ice crystals that spend less time in the supersaturated region contribute to a reduction in NLC brightness. A growth timescale of 400 minutes has been found to provide the optimum amount of time in the supersaturated altitude region and allow the ice crystals to grow to a maximum size [Rapp et al., 2002]. Gravity waves with periods longer than 400 minutes allow the crystals to exist in the supersaturated region for this optimum timescale.

Several studies have shown that NASA Space Shuttle launches can create artificial NLCs due to the large deposits (300 tonnes) of water vapor near 100 km [Stevens et al., 2003; Stevens et al., 2005; Kelley et al., 2010]. The discovery that shuttle exhaust can form NLCs adds a complicating factor to determining long-term trends in NLCs. The most recent investigation of space shuttle exhaust used Solar Backscatter Ultraviolet (SBUV) data from 1985-2011 to examine possible impact from 60 NASA Space Shuttle

launches and found no significant increase in NLC ice signal [DeLand and Thomas, 2019]. A few of the launches show brief peaks in total ice after a launch, but the maximum contribution from these events is usually less than 5% of the total ice mass from a single NLC season. However, the impact from the larger number of smaller rocket launches has yet to be investigated.

1.2.4. Climate Change Implications

NLCs have become an entity of interest to study global climate change since they are sensitive to small changes in their environment [Hervig et al., 2016; Lübken et al., 2018]. Increases in greenhouse gases may result in more frequent and brighter NLCs. Methane (CH4) undergoes a series of complex reactions with OH and excited atomic oxygen to produce water (H2O) and molecular hydrogen (H_2). The oxidation of methane occurs mostly above 30 km and the water vapor is transported upwards to the mesosphere. Also, while carbon dioxide (CO2) works to warm the lower atmosphere, it has a cooling effect in the upper atmosphere through enhanced infrared emission to space. Increases in CO2 and CH4 have been modeled to predict the temperature and humidity change in the mesosphere and how NLCs may be expected to occur more frequently at lower latitudes [Thomas, 1996]. Thomas examined five scenarios of CO2 and CH4 levels and the resulting latitude boundary in which the ambient temperature is 5 K below the frost point temperature. The study included historical values from pre-industrialization, present values, and predicted increases. The results show an expected migration of the latitudinal boundary further south as CO2 and CH4 increase. In the case of pre-industrialization concentrations of CO2 and CH4, the latitude boundary exists at

63° N. This result supports the recent studies showing that NLCs have increased in occurrence, brightness, and that NLCs are occurring at lower latitudes [DeLand et al., 2007]. The pre-industrialization result may reflect why there are no recorded NLC observations before 1885 [Leslie, 1885].

Recent studies have continued to investigate the greenhouse gas impact on NLCs. Model simulations show that the likelihood of seeing NLCs through ground observations has increased dramatically over the decades [Lübken et al., 2018]. The increase of H2O has led to a significant enhancement in NLC brightness which has increased the likelihood of observing an NLC. The water vapor mixing ratio has increased by 1 ppmv since the beginning of industrialization. The study suggests that cooler temperatures due to increased carbon dioxide actually diminish NLC brightness as seen from the ground, because the cooler temperatures promote an increased number of particles of smaller particle size [Lübken et al., 2018]. The smaller particles cause less scattering of light which results in the brightness falling below the threshold of visibility.

1.3. History of Noctilucent Cloud Research

The first published sighting of an NLC was documented by Robert Leslie in 1885 [Leslie, 1885]. Leslie described the sky phenomenon consisting of ‘luminous silvery white cloud’ he witnessed in Southampton, England at about 10 p.m. on July 6, 1885. This first NLC sighting was observed two years after the eruption of Krakatoa, which sent great plumes of ash and water vapor into the middle atmosphere as high as 50 km. The eruption sparked a global interest in watching the evening sky, as unusual sunsets were visible across the world due to the presence of volcanic debris in the atmosphere. Before this

time, studies of the high atmosphere were not regularly conducted, but were more of an extension of interest prompted by new ideas about geomagnetism [Schroder, 1999]. The First International Polar Year occurred between 1882-1883 and documented observations of the auroras in both hemispheres. The state of atmospheric research at this time played into the controversy decades later about whether the eruption of Krakatoa resulted in the first formation of NLCs or whether the first NLC sighting was simply a result of the newfound interest in the high atmosphere and observation of anomalous sky phenomena.

Two other figures must be acknowledged for their early observations of NLCs in the same year as Leslie's observation. Backhouse published his NLC observation after Leslie's but the observation itself occurred earlier in the summer on the night of June 8, 1885 in Germany [Backhouse, 1885]. Jesse studied NLCs that same year in Czechoslovakia and is credited with the German name "*leuchtenden nachtwolken"* [Jesse, 1889]. There are other recorded accounts of unusual sky phenomenon before 1885, but none are clear enough to be considered a definite NLC observation. However, one note by Robinson in Northern Ireland from 1850 reported "strange luminous clouds in NW, not auroral." This account is rare because most other reports of unusual sky observations do not specifically use the key word "luminous" [Butler, 2006].

Between 1885-1886, Jesse established a network of NLC observers in Germany. Jesse also made the first accurate height estimates using ground-based photographic triangulation that estimated the NLCs at an altitude of 82 km [1896].

In 1933, Vestine reported the first observation of an NLC in North America with photographs taken in Alberta, Canada. Vestine later published a comprehensive review

of NLC studies thus far, including a list of observations that had been published in well-known German, English, and French scientific journals since the first recorded observation in 1885 [Vestine, 1934]. The effort had begun to characterize the NLC observations in terms of frequency and noticeable features in the displays.

Stereo-photographs taken by Witt on the night of August 10, 1957 in Sweden measured NLC heights between 81.5-85.5 km [Witt,1962]. Witt also estimated velocities of the movements in the clouds to be between 50-100 m/s from the northeast to the southwest and wave crests that were oriented perpendicular to the main direction of motion.

In the early 1960s, Fogle, a PhD student at the University of Alaska Fairbanks, coordinated a network of NLC observation stations in the United States, Canada, Greenland, and Iceland. Before this time, most of the NLC observations came out of Europe and the USSR, and it was unknown whether NLC displays were as frequent over North America as over Europe. Through the North American observation network coordinated by Fogle, NLC occurrence was found to be comparable to the occurrence over Europe and the USSR, and typical NLC characteristics were confirmed [Fogle, 1966]. Fogle also proved that NLC exist in the southern hemisphere through his own photographic observations in Chile [Fogle, 1964]. Although much understanding was gained on typical NLC characteristics, it was still uncertain at this time how NLCs form.

Some connections between NLC appearance and the onset of summer were proposed by Schroeder [1968]. Schroeder suggested that the transition of mesospheric winds in the spring and the associated uplift of air through the atmosphere drives the first formation of NLCs and the onset of the NLC season.

The first lidar observation of an NLC occurred in Norway on the night of August 5, 1989 with a ground-based sodium lidar [Hansen et al., 1989]. The NLC was detected between 82.2-83.4 km. This first lidar observation excited the possibility of investigating small-scale features of NLCs.

Since 1969, NLCs have been observed by satellite measurements and the presence of NLCs in the daytime was confirmed [Donahue et al., 1972]. The few decades of satellite measurements allowed both long-term and hemispheric NLC variations to be studied. Satellite measurements revealed that NLCs are more frequent and brighter in the Northern hemisphere than the Southern hemisphere. There is an anti-correlation between solar UV activity and NLC frequency and brightness due to the increased photodissociation of water vapor when solar activity is at a peak in the cycle [DeLand et al., 2006].

The work of Thomas highlighted the idea that NLCs may be an indicator of global climate change [Thomas, 1996]. His studies focused on the increases in greenhouse gas concentrations and the expected increase in NLC frequency, brightness, and latitudinal extent [Thomas, 1996; Thomas, 1989].

The Aeronomy of Ice in the Mesosphere (AIM) satellite was launched in 2007 to monitor NLCs and understand their formation and variability [Russell et al., 2009]. It was the first satellite mission dedicated solely to studying NLCs. The satellite includes three payloads including the Cloud Imaging and Particle Size (CIPS) instrument, the Solar Occultation for Ice Experiment (SOFIE) instrument, and the Cosmic Dust Explorer (CDE) instrument. The AIM instruments provided an unprecedented high-resolution of the clouds of 5x5 km in horizontal space. AIM confirmed the existence of very small ice particles

above the main NLC layer, which are evident in radar measurements of polar mesospheric summer echoes (PMSE) [Russell et al., 2009].

Currently there is much interest in investigating NLCs to extract both large-scale and small-scale dynamics such as interhemispheric coupling, gravity waves, turbulence, and instabilities, and using artificial NLC formation to study mesospheric thermodynamics. The recent Super Soaker rocket investigation in January 2018 explosively released 220 kg of water into the mesosphere to study the local cooling effects of water vapor.

Noctilucent cloud researchers convene at the Layered Phenomena in the Mesopause Region (LPMR) workshop. LPMR has been held as a biannual meeting since the 2007 workshop in Fairbanks, Alaska. Special issues on noctilucent clouds have been published usually two years following an LPMR meeting in the Journal of Atmospheric and Solar-Terrestrial Physics (JASTP), the Journal of Geophysical Research (JGR), Atmospheric Chemistry and Physics (ACP), and Atmospheric Measurement Techniques (AMT). A list of LPMR meetings since 2001 and their associated special issues is provided below:

14th LPMR- 2019, Williamsburg, Virginia, USA

13th LPMR- 2017, Kühlungsborn, Germany; ACP 18-20, 2018-2020;

AMT 11-12, 2018-2019 (ACP/AMT joint special issue)

12th LPMR- 2015, Boulder, Colorado, USA; JASTP 162, 2017

11th LPMR- 2013, Leeds, UK; JASTP 127, 2015

10th LPMR- 2011, Blacksburg, Virginia, USA; JASTP 104, 2013

9th LPMR- 2009, Stockholm, Sweden; JASTP 73, 14-15, 2011

8th LPMR- 2007, Fairbanks, Alaska, USA; JASTP 71, 3-4, 2009

7th LPMR- 2004, Cambridge, UK; JASTP 68, 1, 2006

6th LPMR- 2001, Pacific Grove, California, USA; JGR 108, D8, 2003

1.4. Scope of this study

In this thesis, I present a comprehensive study of NLCs observed by lidar at Poker Flat Research Range (PFRR) in Chatanika, Alaska (65° N, 147° W) from 1998-2019. This study includes new NLC lidar observations I participated in from the summers of 2018 and 2019. I use a particularly bright NLC lidar observation from the 2019 campaign to demonstrate the analysis method used for all NLC lidar observations at Chatanika from 1998-2019. I present a mesospheric environment analysis using satellite data to examine NLC occurrence and brightness over Alaska across entire NLC seasons. I also use satellite data to investigate the stability of the NLCs we have observed at Chatanika and determine the source regions that the NLCs may have originated from. Lastly, I present a technical overview of the Rayleigh lidar three-channel receiver system operating at PFRR. A brief overview of each chapter is provided below.

In Chapter 2, I review the principles and technique of Rayleigh lidar. I present a consistent analysis of all the Rayleigh lidar observations conducted during NLC season at Chatanika from 1998-2019. I provide a summary and discussion of the NLC characteristics.

In Chapter 3, I present a satellite analysis of the mesospheric environment over Alaska during NLC season. Cloud detection and albedo data from the Cloud Imaging and Particle Size (CIPS) instrument on the Aeronomy of Ice in the Mesosphere (AIM) satellite

is used to show the behavior of NLC frequency of occurrence and NLC brightness over Alaska across entire NLC seasons. Temperature and water vapor data from the Microwave Limb Sounder (MLS) instrument on the Aura satellite is used to characterize the meteorological conditions during the lidar observations in NLC season. The MLS data is used to examine the stability of the NLCs observed at Chatanika and how stability conditions change to the north of Chatanika.

In Chapter 4, I describe the Rayleigh lidar three-channel receiver system used at PFRR. I provide a signal analysis of the three-channel receiver system using lidar observations from the winter and the summer. I present a new density and temperature retrieval method for combining data from the three channels. I also use temperature data from the Sodium Resonance Wind Temperature Lidar (SRWTL) to extend the Rayleigh lidar density profile.

In Chapter 5, I summarize the key findings from my study and discuss my conclusions. I make recommendations for using CIPS and MLS data in the future in support of the lidar observations conducted at PFRR.

Chapter 2. Lidar Measurements of Noctilucent Clouds

2.1. Rayleigh lidar technique

Rayleigh lidar is a powerful method for studying the middle atmosphere. This region of the atmosphere (~30-90 km) faces spatial, temporal, and cost challenges in terms of measurement. Radars lack measurements between 30-60 km due to the absence of scattering media. Rocket investigations provide high resolution, but short-lived measurements that are expensive and unfeasible to conduct regularly. Rayleigh lidar is a remote sensing technique that enables high-resolution measurements of the middle atmosphere that can be conducted on a routine basis.

The Rayleigh lidar technique utilizes Rayleigh scattering to study the atmosphere. Rayleigh scattering is the scattering of electromagnetic radiation by particles that are much smaller than the wavelength of the incident radiation [Strutt, 1899]. In a Rayleigh lidar system, a laser transmits pulses of light into the sky. The transmitted photons are scattered by particles in the atmosphere and the backscattered photons are collected by a telescope. The time it takes for a return signal to reach the receiving system is used to determine the altitude of the backscattered signal, given the speed of light. In an aerosol-free atmosphere, the received signal is proportional to the density of the atmosphere. Therefore, Rayleigh lidar provides profiles of relative density of the atmosphere with altitude and time.

Within a time interval, Δt, the expected signal from an altitude range $(z - \Delta z/2, z + \Delta z/2)$ is given by the lidar equation:

$$N(z) = N_s(z) + N_B + N_D \tag{2.1}$$

where $N_s(z)$ is the signal proportional to atmospheric density, N_B is the background signal due to skylight, and N_D is the dark current signal within the detector. $N_s(z)$, N_B, and N_D are defined as the following:

$$N_s(z) = \eta T^2 \frac{E_L R_L \Delta t}{hc/\lambda_L} \rho(z) \Delta z \sigma_\pi^R \frac{A_T}{z^2} \tag{2.2}$$

$$N_B = \eta \left[H_N R_L \Delta z \pi (\Delta \Theta_R/2)^2 A_T \Delta\lambda \right] \left(\frac{2\Delta z/c}{hc/\lambda} \right) \tag{2.3}$$

$$N_D = (C_N R_L \Delta t)\left(2\Delta z/c\right) \tag{2.4}$$

where η is the receiver efficiency, T is the one-way atmospheric transmission, λ_L is the laser wavelength in meters, E_L is the laser energy per pulse in Joules, R_L is the repetition rate of the laser (pps) , $\rho(z)$ is the molecular number density (m^{-3}) at altitude z, σ_π^R is the effective backscatter cross section at λ_L (m), h is Planck's constant (6.63×10^{-34} J s), c is the speed of light (3.00×10^8 m/s), A_T is the area of the telescope (m^2), H_N is the background sky radiance ($W/(m^3 \mu m\ sr)$), $\Delta\Theta_R$ is the field of view of the receiver (0.5-1 mrad), $\Delta\lambda$ is the bandwidth of the detector (μm), and C_N is the dark signal rate of the detector (s^{-1}). The dark signal rate is the inherent count in the PMTs in the absence of light due to thermal emission in the detector. The dark signal will be discussed in more detail in Chapter 4.

The backscattered signal is processed by a high-speed counter and converted to an electronic signal. The electronic signal is sent to a computer which records the data. The returned signal is integrated over a short time interval (0.32 μs) which corresponds to the altitude range sampling resolution (48 m). The returned signal is integrated over a

number of laser pulses (typically 1000 pulses) which corresponds to the time sampling resolution (50 s).

The statistics of the photon counting process have a Poisson distribution [Papoulis, 1984]. The standard error in the lidar signal is therefore the square root of the total lidar signal,

$$\Delta N_S(z) = \sqrt{N_S(z) + N_B + N_D} \tag{2.5}$$

2.2. The Poker Flat Rayleigh lidar

The Rayleigh Density Temperature Lidar (RDTL) at Poker Flat Research Range (PFRR) in Chatanika, Alaska was installed in November 1997 [Mizutani et al., 2000] and is operated by the Geophysical Institute (GI) of the University of Alaska Fairbanks (UAF). The Rayleigh lidar system consists of a transmitter, a receiver system, and a data acquisition system. The transmitter is a Neodymium-doped:Yttrium Aluminum Garnet (Nd:YAG) laser. The laser operates at 532 nm with a pulse repetition rate of 20 Hz. The average laser power is currently 9-10 W. The Rayleigh lidar is operated only during the night, since daytime observations would require a narrow band pass filter around 532 nm to reject incoming sunlight. Currently the receiver is configured as a three-channel system, with each channel consisting of a photomultiplier tube, interference filter, and high-speed counter [Triplett, 2016]. The operation and data retrieval of the three-channel receiver system is detailed in Chapter 4 of this thesis. Typically, the returned signal is integrated over 50 seconds (1000 laser shots) and the integration is considered one profile of data. Table 2.1 provides the system specifications for the RDTL.

Table 2.1 RDTL System Specifications

Transmitter	
Laser	Nd:YAG
Model	Continuum Powerlite 8020
Wavelength (λ_L)	532 nm
Repetition rate (R_L)	20 Hz
Pulse energy (E_L)	450-500 mJ
Pulse width	5-7 ns
Divergence	0.45 mrad
Beam expander	x 10
Receiver	
Telescope diameter	1.04 m
Field of view	0.5 mrad
Detector	Photomultiplier tube
Digital recorder	Multichannel scalar
Maximum count rate	100 MHz

2.3. Analysis of Noctilucent Clouds

The analysis presented in this thesis builds upon previous studies of individual NLCs observed by lidar at Chatanika [Collins et al., 2003; Collins et al., 2009; Kelley et al. 2010]. For the current analysis of all NLCs observed at Chatanika from 1997-2019, the raw lidar profiles are integrated over 300 seconds (6000 shots) and then smoothed with a linear running average of 225 m between 60 to 90 km. MSIS-E-90 data is used to calculate and correct for extinction of the atmosphere. Noctilucent clouds in this study are characterized by their backscatter ratio, backscatter coefficient, and integrated backscatter coefficient.

After the background signal and the dark signal have been subtracted from the total lidar signal, the lidar signal is the sum of the molecular Rayleigh scatter signal, N_M, and the aerosol Mie scatter signal, N_A:

$$N_S(z) = N_M(z) + N_A(z) \tag{2.6}$$

The backscatter ratio is a measure of the relative brightness of the noctilucent cloud compared to the molecular atmosphere at a given altitude and time. The total backscatter ratio, R_{TOT} , is the sum of the molecular Rayleigh scatter signal and the aerosol Mie scatter, divided by the molecular Rayleigh scatter signal. The aerosol backscatter ratio is the total backscatter ratio minus one:

$$R_{TOT} = \frac{N_M(z) + N_A(z)}{N_M(z)} \tag{2.7}$$

$$R_A = R_{TOT} - 1 \tag{2.8}$$

When a noctilucent cloud is present, the lidar signal increases due to the addition of aerosol scatter to molecular scatter. Therefore, the molecular Rayleigh scatter signal must first be estimated before calculating the backscatter ratio. The molecular signal is

estimated in the following way. First, the lidar signal at each altitude bin between 60 to 90 km is summed across the night. The summed signal profile is then range-scaled to 60 km. A third-order polynomial fit is performed on the natural logarithm of the range-scaled summed signal from 60-90 km, excluding a 5 km range where the cloud signal is present (typically 80-85 km). After the fit has been performed, the summed signal profile is de-range-scaled. The estimated Rayleigh scatter signal is then normalized to the signal at each profile in time by a scaling factor. The scaling factor, $SF,$ is the sum of the signal between 68 to 72 km divided by the sum of the signal between 68 to 72 km of the estimated Rayleigh scatter signal. The backscatter ratio of each profile is calculated as the ratio between the true signal and the scaled estimated Rayleigh scatter signal. Figure 2.1 shows the estimated Rayleigh scatter signal (blue) plotted over the natural logarithm of the summed signal from the night of August 11-12, 2019. The observation on this night yielded a total of 48 five-minute profiles. Figure 2.1 also shows signal from profile 31 of the night (~01:00 LST) and the corresponding scaled estimated Rayleigh scatter signal (green). The scale factor is defined as the 2,981 signal counts summed from profile 31 divided by 150,861 signal counts summed from across the night. The backscatter ratio of the NLC observed on August 11-12, 2019 is shown in the top panel of Figure 2.2. The NLC on that night was up to 150 times brighter than the molecular atmosphere.

Before the Fall of 2019, the Rayleigh scatter signal had been estimated using a linear extrapolation from the summed signal between 68-72 km instead of the third-order polynomial fitting method described above. The linear extrapolation typically underestimated the backscatter ratio because the estimated Rayleigh scatter signal would cut too high above the base of the cloud signal. Further details on the linear

extrapolation fit and comparisons with the third-order polynomial fit are provided in Appendix B.

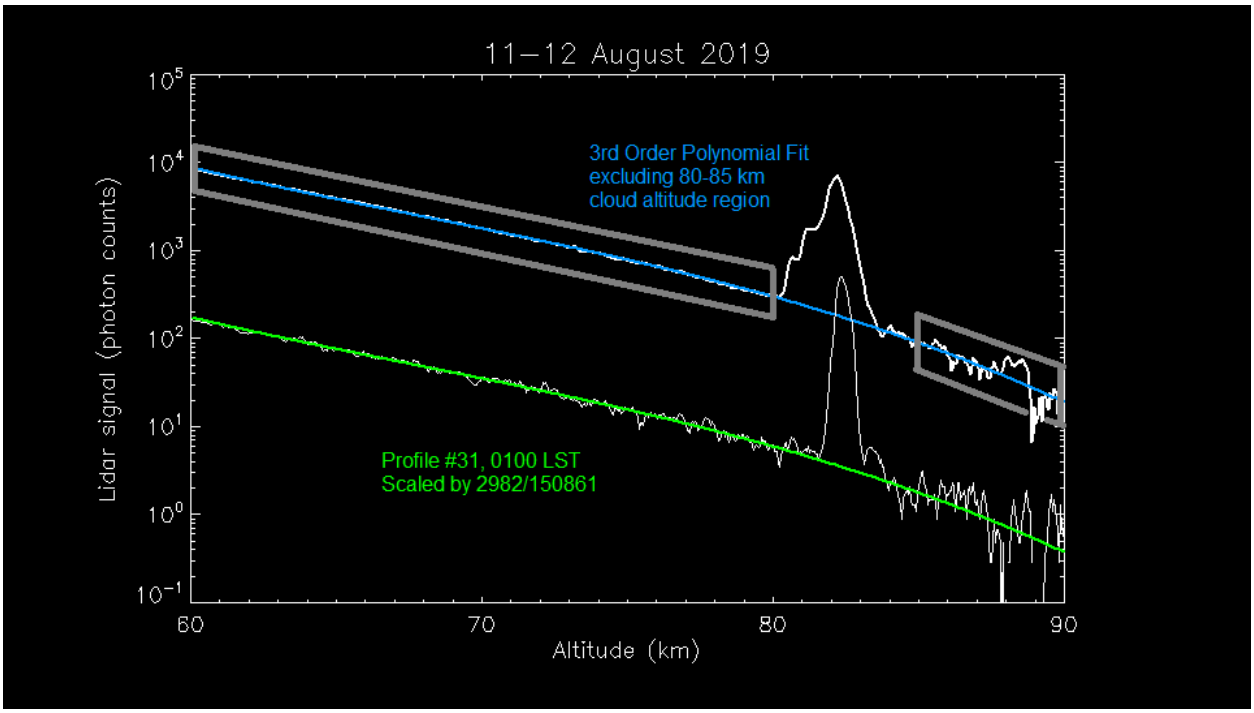

Figure 2.1. Rayleigh scatter signal estimate fitting on 11-12 August 2019. Lidar signal summed over the night of August 11-12, 2019 (top, white), the estimated Rayleigh scatter signal (blue), the signal from profile 31 of the night (bottom, white), and the scaled Rayleigh scatter estimate for profile 31 (green). The gray boxes show the altitude range where the Rayleigh scatter fit was performed.

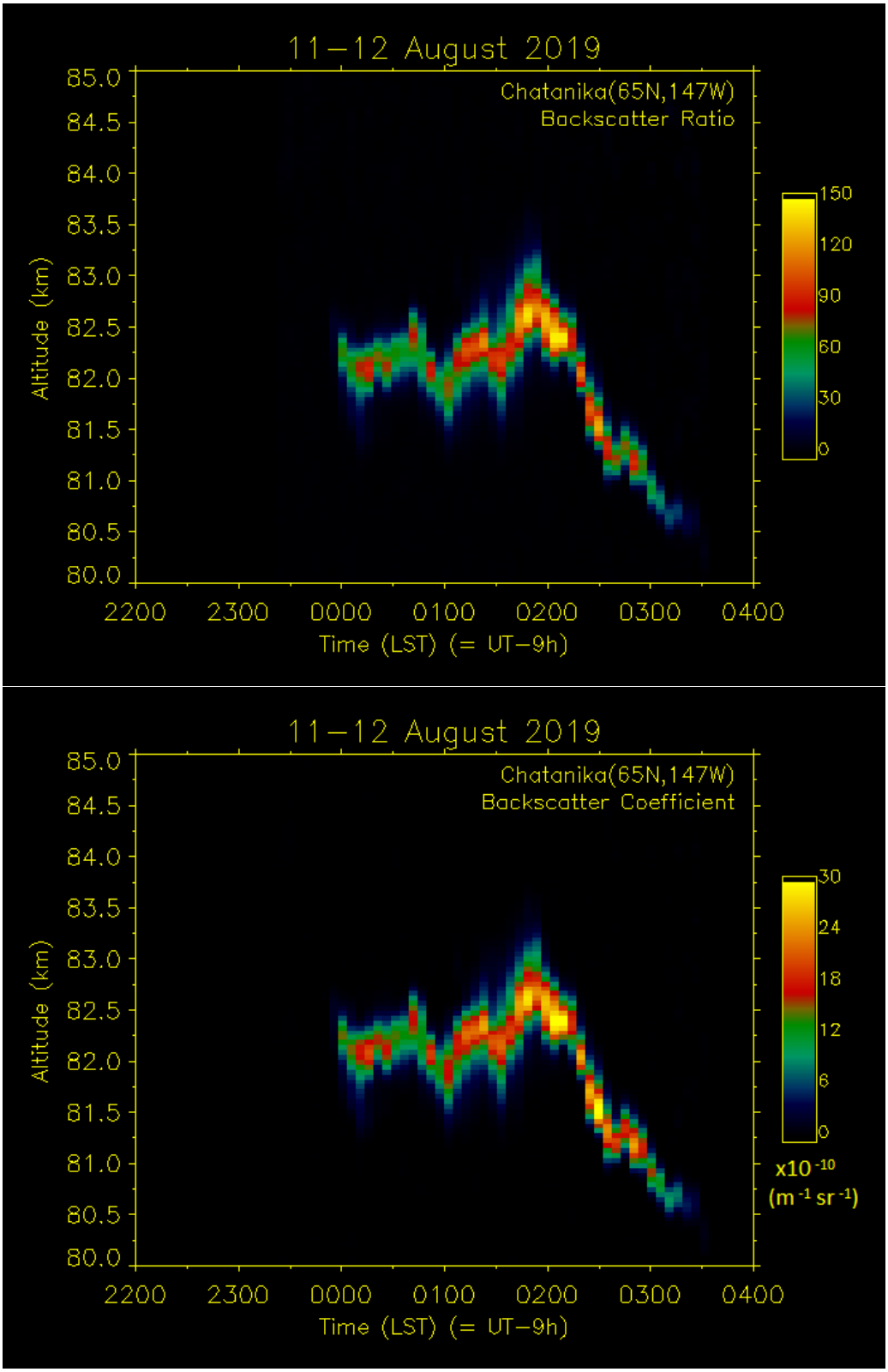

Figure 2.2. False color plots of backscatter ratio (top) and backscatter coefficient (bottom) with time and altitude for the NLC observed by the PFRR Rayleigh lidar on August 11-12 2019.

The error associated with the aerosol backscatter ratio is proportional to the standard error in the lidar signal:

$$\Delta R_a = \frac{\Delta N_S}{R_{est} * SF} \tag{2.9}$$

where R_{est} is the estimated Rayleigh scattering signal and SF is the scaling factor discussed previously.

The volume aerosol backscatter coefficient is a measure of the absolute brightness of the noctilucent cloud at a given altitude and time. The volume aerosol backscatter coefficient, BC_A, is the product of the aerosol backscatter ratio and the molecular backscatter coefficient, BC_M,

$$BC_A = R_A \cdot BC_M \tag{2.10}$$

The backscatter coefficient with height and time for the NLC observed on August 11-12, 2019 is shown in the bottom panel of Figure 2.2. The molecular backscatter coefficient is the product of the Rayleigh backscatter cross-section and the molecular atmospheric density. An atmospheric density profile from an Arctic observational seasonal climatology [Lübken, 1999] is used to determine the molecular atmospheric density. The error associated with the volume aerosol backscatter coefficient is due to the error in the backscatter ratio and calculated by propagation of error as:

$$\Delta BC_A = BC_A \cdot \frac{\Delta R_A}{R_A} \tag{2.11}$$

The integrated backscatter coefficient (IBC) is a measure of the brightness of the noctilucent cloud across its entire vertical extent. The IBC is calculated by integrating BC_A over a 4 km altitude range appropriate for the noctilucent cloud, typically 80.5 to 84.5 km,

$$IBC = \int_{alt0}^{alt0+L} BC_A(z) \tag{2.12}$$

Only significant IBCs are considered in the statistical characteristics of each NLC. An IBC is considered significant if it is greater than three times its error, which is defined as,

$$\Delta IBC = \sqrt{\int_{alt0}^{alt0+L} \left(BC_A err(z)\right)^2 dz} \tag{2.12}$$

After significant IBC values have been examined, the data is reprocessed to focus on the part of the night when the NLC is present. Figure 2.3 shows the IBC throughout the night for the NLC observed on August 11-12, 2019. Cloud duration is determined by the number of 300-second-integrated profiles where the IBC is significant. The NLC observed on August 11-12, 2019 had a cloud duration of 3 hours and 55 minutes.

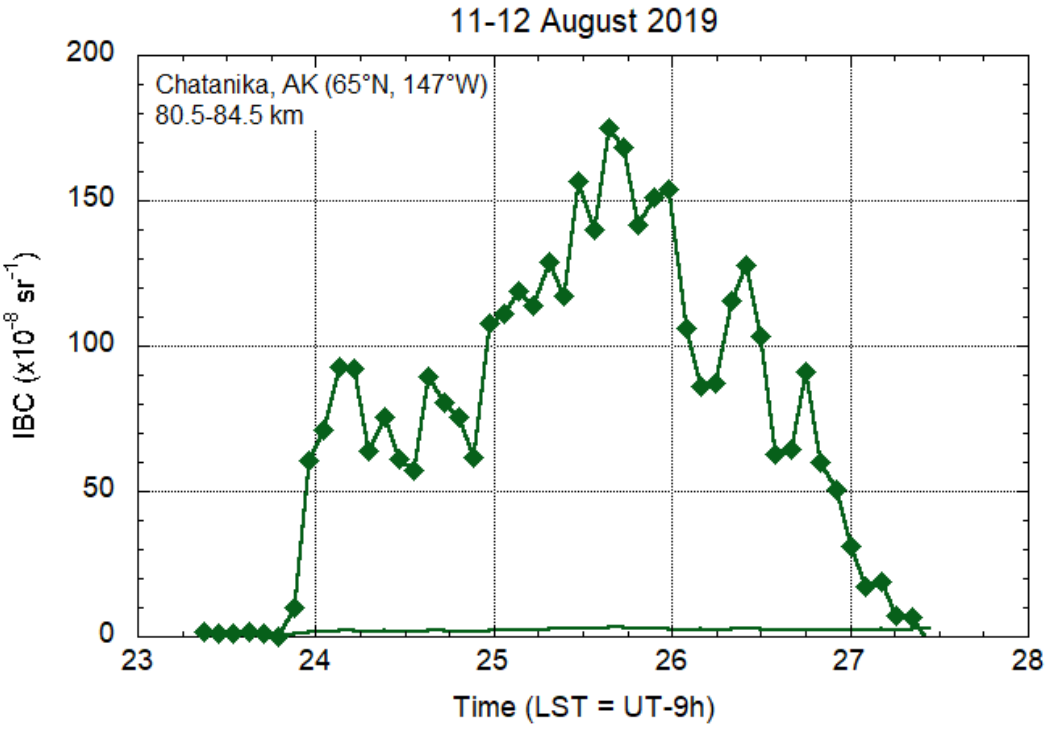

Figure 2.3. The integrated backscatter coefficient for the NLC observed on August 11-12, 2019. The thin green line at the bottom shows the threshold of $3\Delta IBC$.

2.4. NLC Lidar observations

Due to lighting conditions in Alaska, lidar observations during noctilucent cloud season are typically not conducted until late July. In this study, Poker Flat Rayleigh lidar data from July and August nights between 1998 and 2019 is considered. There are 71 nights of observations over this time range. Data for analysis is then confined to those observations that last 2.3 hours or longer and data with high quality signal statistics. The signal statistic of average signal per pulse is used as the signal quality threshold. The average signal per pulse is a measure of the returned signal counts from each pulse of the laser at the altitude range of 60-65 km. This restriction is important because a sudden drop in signal per pulse creates relatively noisy profiles. The signal per pulse can fluctuate significantly if low level clouds are passing overhead. The noisiness at the high altitudes makes it difficult to resolve a noctilucent cloud signature, given the increased error associated with the photon counting statistics. Also, noisier profiles make the extrapolated fit for the Rayleigh scatter signal estimate less accurate. The Rayleigh data is restricted to nights with an average signal per laser pulse of at least 0.3 counts, and nights where the signal per pulse was steady throughout the observations. The data quality restrictions yield 41 nights of data from 1998-2019 from the nights between July 31 and August 31 for analysis. The yearly distribution of the 41 Rayleigh lidar observations at Chatanika is plotted in Figure 2.4. There were no lidar observations made in 1998 that met the quality thresholds set for this study. Each night of high quality data is analyzed with the methods detailed in section 1.3. It must be noted that the 30 observations that did not pass the selection criteria were also analyzed using the methods detailed in section 1.3, and that no NLCs were apparent in these lower quality observations.

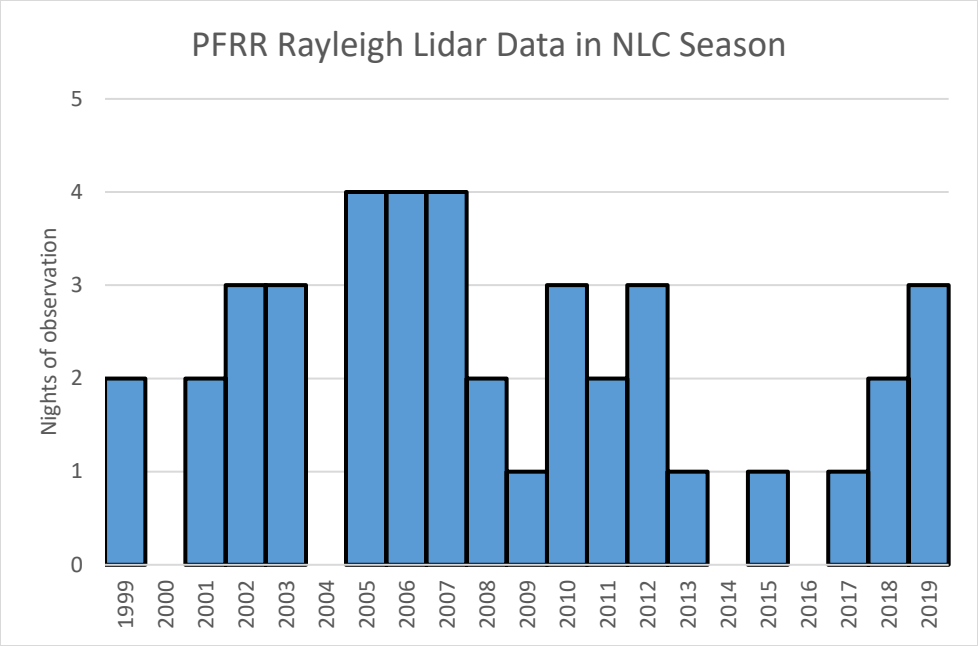

Figure 2.4. Histogram of the quality Rayleigh lidar observations during NLC season at Chatanika, Alaska from 1999 through 2019.

Of the 41 high quality observations, 21 nights include significant IBC (IBC>3ΔIBC) values indicating the presence of NLCs. A summary of NLC characteristics measured by Rayleigh lidar at Chatanika is shown in Table 2.2. Maximum IBCs range from 2.10 $x10^{-8}$ sr^{-1} to 3.29 $x10^{-6}$ sr^{-1}. Cloud duration ranges from 15 minutes to 235 minutes. Maximum BCs range from 2.81$x10^{-11}$ $m^{-1}sr^{-1}$ to 8.28$x10^{-9}$ $m^{-1}sr^{-1}$. Maximum BCs are seen at altitudes between 79.4 km to 84.0 km. The average cloud duration of NLCs measured by Rayleigh lidar at Chatanika is 99 minutes. The average maximum IBC is 8.10$x10^{-7}$ sr^{-1}. The average maximum BC is 1.42$x10^{-9}$ m^{-1} sr^{-1} and maximum BCs occur at an average altitude of 82.1 km.

Table 2.2 Summary of NLC Characteristics

Date	Cloud duration (min)	Max IBC (sr^{-1})	Avg IBC (sr^{-1})	Max peak BC ($m^{-1}sr^{-1}$)	Max peak BC altitude (km)	BR at max peak BC
Aug 4-5 1999	70.0	$2.75x10^{-7}$	$1.62 x10^{-7}$	$7.30x10^{-10}$	81.8	29.4
Aug 16-17 2001	55.0	$3.77x10^{-8}$	$2.60x10^{-8}$	$8.26x10^{-11}$	81.8	3.7
Aug 20-21 2001	15.0	$2.47x10^{-8}$	$1.84x10^{-8}$	$5.11x10^{-11}$	81.1	2.0
Aug 3-4 2002	90.0	$3.23 x10^{-6}$	$5.47 x 10^{-7}$	$8.28x10^{-9}$	79.4	217.0
Aug 6-7 2003	80.0	$1.17 x10^{-6}$	$4.26 x10^{-7}$	$2.02 x10^{-9}$	81.6	78.9
Aug 9-10 2005	160.0	$3.29 x10^{-6}$	$9.71 x10^{-7}$	$3.43 x10^{-9}$	82.1	156.3
Aug 18-19 2005	30.0	$3.79 x10^{-7}$	$1.85 x10^{-7}$	$7.15 x10^{-10}$	84.0	50.1
Aug 1-2 2006	103.3	$1.06 x10^{-6}$	$5.01 x10^{-7}$	$1.75 x10^{-9}$	81.7	69.3
Aug 2-3 2006	85.0	$1.43 x10^{-6}$	$6.19 x10^{-7}$	$3.18 x10^{-9}$	80.5	101.1
Aug 8-9 2006	25.0	$4.01x10^{-8}$	$3.14x10^{-8}$	$1.65 x10^{-10}$	82.6	8.3
Aug 10-11 2007	198.3	$1.71 x10^{-6}$	$7.50 x10^{-7}$	$2.21 x10^{-9}$	83.2	124.5
Aug 16-17 2007	125.0	$2.39 x10^{-7}$	$1.37 x10^{-7}$	$3.82 x10^{-10}$	83.2	23.0
July 31-Aug 1 2010	171.7	$1.04 x10^{-6}$	$4.27 x10^{-7}$	$1.42 x10^{-9}$	81.7	56.5
Aug 3-4 2010	30.0	$1.11x10^{-7}$	$7.00x10^{-8}$	$2.70 x10^{-10}$	84.3	18.3
Aug 8-9 2012	95.0	$2.68 x10^{-8}$	$1.14 x10^{-8}$	$5.98 x10^{-11}$	82.2	2.8
Aug 10-11 2012	65.0	$1.00 x10^{-7}$	$3.71 x10^{-8}$	$2.95 x10^{-10}$	80.7	10.3
Aug 13-14 2012	110.0	$2.10x10^{-8}$	$9.04x10^{-9}$	$2.81 x10^{-11}$	84.2	1.9
Aug 6-7 2013	85.0	$6.67 x10^{-7}$	$3.57 x10^{-7}$	$9.94 x10^{-10}$	81.2	35.8
Aug 10-11 2018	115.4	$2.12 x10^{-7}$	$8.03 x10^{-8}$	$4.38 x10^{-10}$	82.4	21.3
Aug 7-8 2019	140.0	$1.94 x10^{-7}$	$5.02 x10^{-8}$	$2.04 x10^{-10}$	82.9	10.3
Aug 11-12 2019	235.0	$1.75 x10^{-6}$	$7.92 x10^{-7}$	$3.15 x10^{-9}$	81.4	126.8

The NLC with the largest IBC was observed on August 9-10, 2005 with an IBC of 3.29 $x10^{-6}$. This NLC was observed by both lidar and cameras to the south of PFRR [Collins et al., 2009]. It is interesting that NLCs were visible to the north by ground observers at PFRR on the nights immediately preceding and following the August 9-10, 2005 NLC observation, but were not detected overhead by lidar on those nights. Medium-frequency radar data examined by Collins et al. showed no significant change in the southwestward wind on the three nights. Collins et al. used a microphysical model to determine that the water vapor mixing ratio on the August 9-10 2005 night was 7-9 ppmv. Satellite measurements will be used to examine the water vapor environment of NLCs detected at Chatanika in Chapter 3.

The most recent NLC observation on August 11-12, 2019 was the NLC measured for the greatest length of time. The NLC was observed continuously for 3.9 hours. This NLC also has the second highest average IBC of 7.92 $x10^{-7}$ sr^{-1}. The NLC display on this night was particularly brilliant, with NLC structures visible across most of the northern sky. Photos of the NLC structure observed on this night are shown in Figure 2.5.

Out of 41 nights of high quality data, NLCs were detected by the lidar on 21 nights, yielding a frequency of NLC occurrence at Chatanika of 51%. There are eight nights of observation within the 71 observations where NLCs were not detected by the lidar but were visible in the north to ground observers at PFRR. These ‘visible only’ NLC nights occurred on July 29-30, 2002; July 31-August 1, 2002; August 7-8, 2003; August 8-9, 2005; August 10-11, 2005; August 3-4, 2006; August 7-8, 2007; and August 11-12, 2009. Four of these nights that are included in the 41 high quality observations are: August 7-8, 2003; August 8-9, 2005; August 10-11, 2005; and August 11-12, 2009.

Figure 2.6 shows the maximum BC for each significant NLC and the altitude at which the maximum BC occurred. There appears to be a relation showing brighter NLCs occurring at lower altitudes. This relationship has been found in other NLC studies and may point to the growth-sedimentation mechanism where ice crystals enlarge through the deposition of water onto the crystal as they descend due to gravity [Rapp and Thomas, 2006]. The ice crystals at the lower altitudes are closer to attaining their maximum brightness than the ice crystals at higher altitudes.

Figure 2.7 shows the cloud duration and average and maximum IBC for each significant NLC. There is some indication evident in the average IBC that longer-lived clouds are brighter. This finding may reflect microphysical studies which have shown that longer lengths of time spent in the supersaturated region allow cloud particles to grow to their maximum size and achieve higher brightness [Rapp et al., 2002].

Figure 2.5. Noctilucent clouds observed at Poker Flat Research Range in Chatanika, Alaska on the night of August 11-12, 2019.

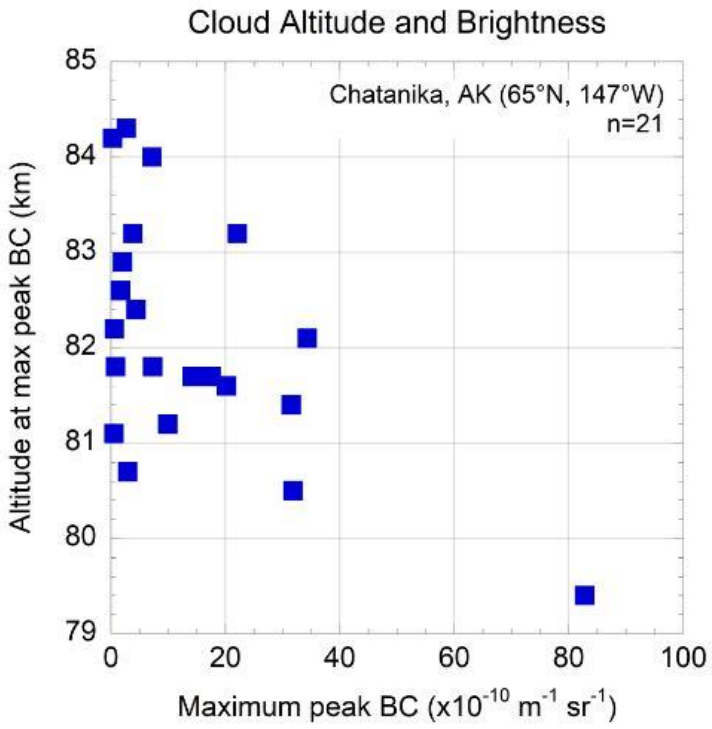

Figure 2.6. Maximum BC and altitude of maximum BC for the 21 significant (IBC≥3ΔIBC) NLCs observed by Rayleigh lidar at Poker Flat.

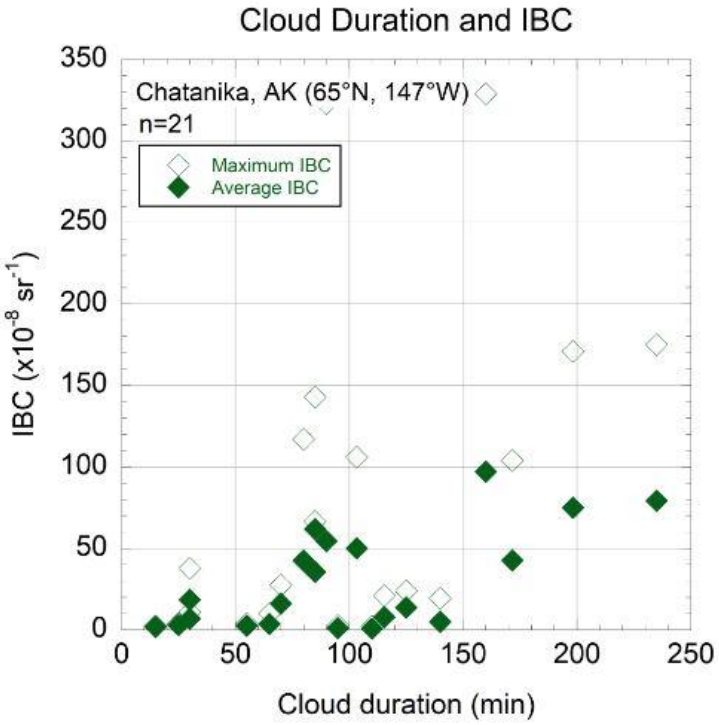

Figure 2.7. Maximum IBC and average IBC with cloud duration for the 21 significant (IBC≥3ΔIBC) NLCs observed by Rayleigh lidar at PFRR.

2.5 Summary and Conclusions

Methods for analyzing noctilucent cloud observations by Rayleigh lidar have been established. Rayleigh lidar observations in Chatanika, Alaska during NLC seasons between 1998-2019 have been analyzed. Out of 41 nights of high quality lidar observations, 21 nights were found to include significant IBC (IBC≥3ΔIBC) values indicating NLC presence. The frequency of NLC occurrence on a nightly basis at Poker Flat in Chatanika is 51%. There is evidence for brighter NLCs occurring at lower altitudes, which may reflect the growth-sedimentation mechanism of ice crystals. There is also some indication of the longer-lived clouds being the brightest clouds. The most recent NLC observation on August 11-12, 2019 was the longest detection (3.9 hours) of an NLC by lidar at Chatanika. This most recent NLC observation also included the second highest average IBC (7.92×10^{-7} $m^{-1}sr^{-1}$) of all NLC observations at Chatanika.

Chapter 3. Satellite Analysis of Noctilucent Clouds

3.1. The Cloud Imaging and Particle Size (CIPS) Instrument

The Aeronomy of Ice in the Mesosphere (AIM) satellite was launched in April 2007 to study noctilucent clouds (NLCs) in terms of their chemistry, physics, and variability [Russell et al., 2009]. The satellite operates in a near-circular polar orbit at ~555 km and makes 15 orbits per day. The Cloud Imaging and Particle Size (CIPS) detector is one of three instruments onboard the AIM satellite. CIPS is a panoramic imager consisting of four wide-angle cameras in a 2x2 arrangement. The cameras operate in a 10 nm passband centered at 265 nm. The field of view of the 2x2 camera arrangement is 120° along track by 80° cross track. CIPS measures ultraviolet radiation scatter by clouds and the atmosphere and retrieves the NLC parameters of albedo, particle radius, and ice water content. The design of CIPS was crafted around the favorability of UV imaging and near-nadir viewing. Ozone absorption in the spectral region near 260 nm blocks out Earth's surface signal and provides an efficient contrast between NLC scattering and the atmospheric background. Near-nadir viewing is chosen to remove line-of-sight effects present in limb viewing. By imaging the same cloud multiple times at different angles, CIPS is able to derive particle size information. The horizontal spatial resolution of CIPS is 5 km x 5 km [Russell et al., 2009].

The lidar measurements of NLCs at Chatanika have not previously been compared to CIPS measurements. The motivation of the current study is to retrieve the CIPS measurements that overlap with the lidar observations during NLC season and to examine CIPS measurements above Alaska over entire NLC seasons. The lidar measurements at Chatanika during NLC season are constrained by the summertime

lighting conditions, so that observations are conducted during late July and the first few weeks of August. The CIPS measurements can provide the broader context of NLC occurrence and brightness over Alaska since CIPS makes measurements throughout the NLC season (May-August). The broader coverage of CIPS measurements in time and space allows the lidar measurements of NLCs to be understood within the seasonal variations seen by CIPS.

3.2. CIPS Analysis

CIPS level 3C data between 2007-2019 is used to retrieve NLC frequency of occurrence and brightness over Alaska during 20 nights of lidar observations. CIPS data is not available in the Northern Hemisphere for the summers of 2017 and 2018. The Northern Hemisphere CIPS level 3C data is a summary file that gives all northern hemisphere data from one NLC season. The data is binned by each orbit and by 1-degree latitudinal bins. CIPS data is taken from a spatial region of 60-70° N and 130-170° W. This region covers almost all of Alaska and part of the Yukon Territory. Figure 3.1 shows the 60-70° N latitude data bins over all longitudes on the UT day of August 12, 2007. The spatial region considered in this study captures two ascending nodes and two descending nodes of the AIM satellite. The ascending node tracks are shorter due to the quality degrading below ~67° N. CIPS data is typically available at three different albedo thresholds. The lowest threshold of 1 G (10^{-6} sr^{-1}) is used in this analysis for all years except 2015 and 2019, in which the 5 G threshold is used. The CIPS data in 2015 and 2019 are provided at 35 different thresholds, and currently the recommended threshold

is the 5 G level. The threshold indicates the lowest albedo value used to determine NLC presence.

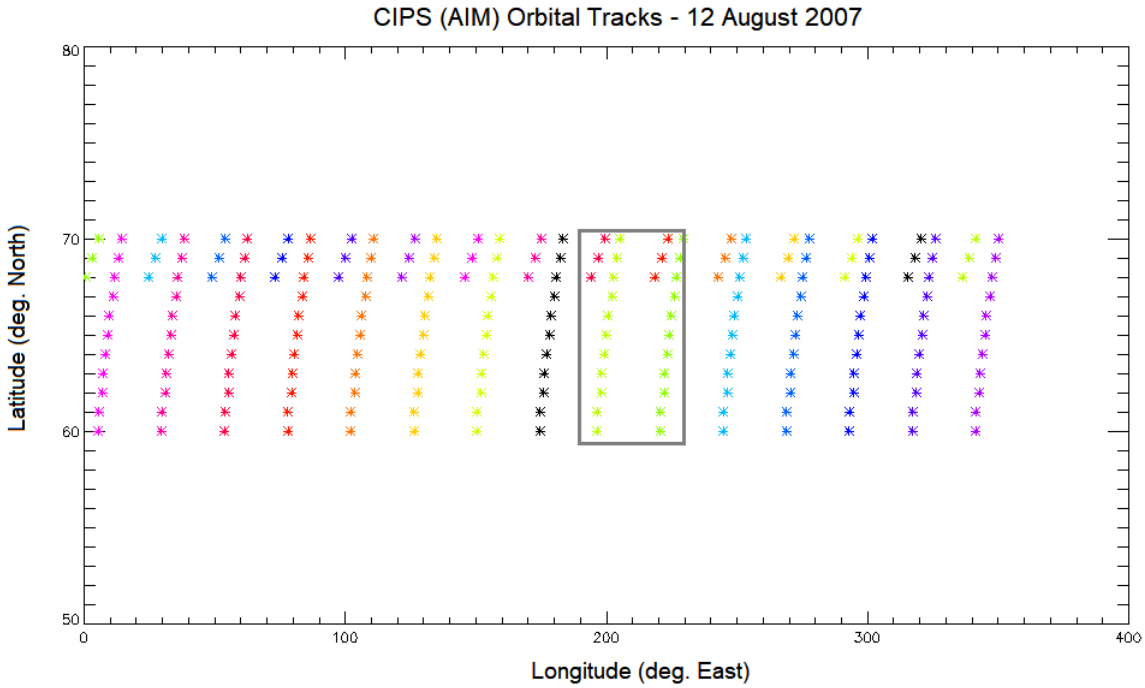

Figure 3.1. Locations of CIPS Level 3C 1-degree data bins from 60-70° N latitude on the UT day 12 August 2007. The gray outline shows the spatial region considered for the CIPS analysis over Alaska (60-70° N, 130-170° W).

It must be noted that the CIPS retrieval algorithms have changed over the years because the spacecraft orbit has changed. Currently the CIPS team is reprocessing all years of data under a new retrieval algorithm. As such, it is not currently advisable to use CIPS to compare NLC behavior between years. CIPS data will be used here to report NLC frequency and brightness for single days and over individual NLC seasons but is not used to compare characteristics between seasons. The CIPS level 3C ‘cld’ and ‘all’ files are used in this study. The ‘cld’ file includes all measurements that detected NLC presence above the chosen threshold value. The ‘all’ file includes both cloud and non-cloud points. For each night of lidar observations, the CIPS data is binned to include

measurements from the previous 24 hours and the following 24 hours, centered upon midnight LST (09:00 UT) of the corresponding lidar observation. Cloud frequency of occurrence is determined by the total number of positive NLC detections divided by the total number of CIPs observations in the spatial region and time bin. Cloud brightness is calculated as a weighted average albedo. The weighting factor is determined by the number of positive cloud detections in a 1-degree bin, divided by the total number of cloud detections in the entire spatial region over Alaska. The average albedo given in each 1-degree latitude bin is multiplied by its weighting factor, and then all individual weighted albedos are summed to yield the weighted average albedo as a single value for the night of interest. Table 3.1 shows the CIPS NLC frequency of occurrence and brightness values for each of the corresponding lidar measurements.

Table 3.1. CIPS Measurements Over Alaska [1]

Date of lidar observation	Lidar maximum IBC[2] ($x10^{-8}$ sr^{-1})	CIPS total NLC detections	CIPS total observations	CIPS NLC frequency	CIPS weighted average albedo ($x10^{-6}$ sr^{-1})
Aug 8-9 2007	NA	118	125,147	<1%	1.23
Aug 9-10 2007	NA	13,296	137,651	9.7%	7.48
Aug 10-11 2007	171	21,806	147,756	14.8%	6.12
Aug 16-17 2007	23.9	5,233	93,419	5.6%	3.04
Aug 11-12 2008	NA	7,702	108,382	7.1%	3.15
Aug 19-20 2008	NA	39	176,830	<1%	NA
Aug 11-12 2009	NA	5,668	94,159	6.0%	3.36
July 31-Aug 1 2010	104	13,508	195,539	7.0%	2.78
Aug 3-4 2010	11.1	13,880	155,715	8.9%	2.02
Aug 21-22 2010	NA	10	63,857	<1%	NA
Aug 11-12 2011	NA	13	138,668	<1%	NA
Aug 18-19 2011	NA	31	105,870	<1%	NA
Aug 8-9 2012	2.68	172	48,909	<1%	3.08
Aug 10-11 2012	10.0	231	77,251	<1%	2.51
Aug 13-14 2012	2.1	157	83,118	<1%	1.81
Aug 6-7 2013	66.7	3,288	29,679	11.1%	3.61
Aug 7-8 2019	19.4	1,801	26,246	6.9%	9.78
Aug 11-12 2019	175	1,440	38,887	3.7%	9.81
Aug 19-20 2019	NA	292	42,730	<1%	5.59

[1] CIPS measurements taken over 60°-70° N, 130°-170° W, +/- 24 h around local midnight (UT-9h) of lidar observation

[2] NA- no NLC detected

The CIPS NLC frequency and albedo are also examined across entire NLC seasons for each year when lidar observations were conducted. The CIPS data is binned over 24 hour periods centered at local midnight (09:00 UT). Figures 3.2a-i show the CIPS frequency and albedo variations for each season. The dotted lines show the 7-day running average in frequency and albedo. Nights of lidar observations at Chatanika are circled in black and noted whether NLCs were or were not detected during the lidar observation. In cases where the frequency of occurrence is 0%, there is no data point for albedo on the corresponding day. Both weak (IBC<3ΔIBC) and significant (IBC>3ΔIBC) NLC detections are noted as positive detections. CIPS detects NLCs in the Northern Hemisphere beginning in early May and continues through the end of August. Generally, the expected seasonality is seen in both cloud frequency and albedo with both values increasing as summer progresses up to solstice and decreasing in the second half of summer. Many of the lidar detections at Chatanika confirm the cloud frequency of occurrence and brightness conditions seen over Alaska by CIPS. For example, in 2007 there were two lidar observations on August 8-9 and August 9-10 which did not detect NLCs, and these nights show a CIPS frequency of occurrence of less than 1%. A lidar observation on the night after on August 10-11 did detect an NLC, and the CIPS cloud frequency of occurrence and albedo both indicate high values for this time of the season. The CIPS cloud frequency on August 10-11 was over 20% and the albedo was over 6 G. On the night of August 16-17, the lidar observations again detected an NLC, and CIPS saw high cloud frequency and brightness relative to the typical low values seen this late in the season. The CIPS cloud frequency on August 16-17 was over 10% and the albedo was about 3 G.

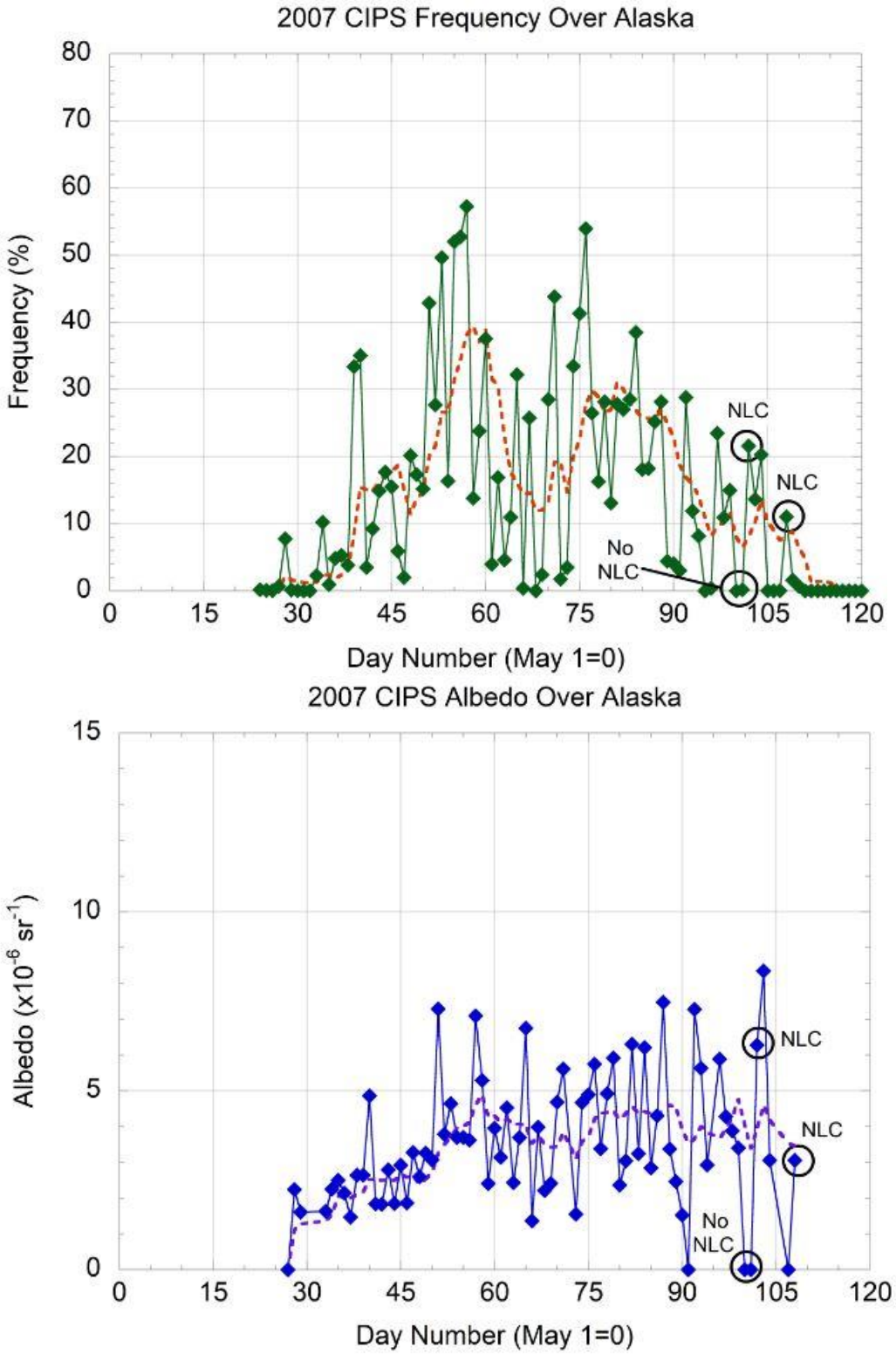

Figure 3.2a. CIPS frequency and albedo over Alaska (60-70°N, 130-170°W) during the 2007 NLC season. Nights of lidar observations are circled indicating positive or negative detections of NLCs.

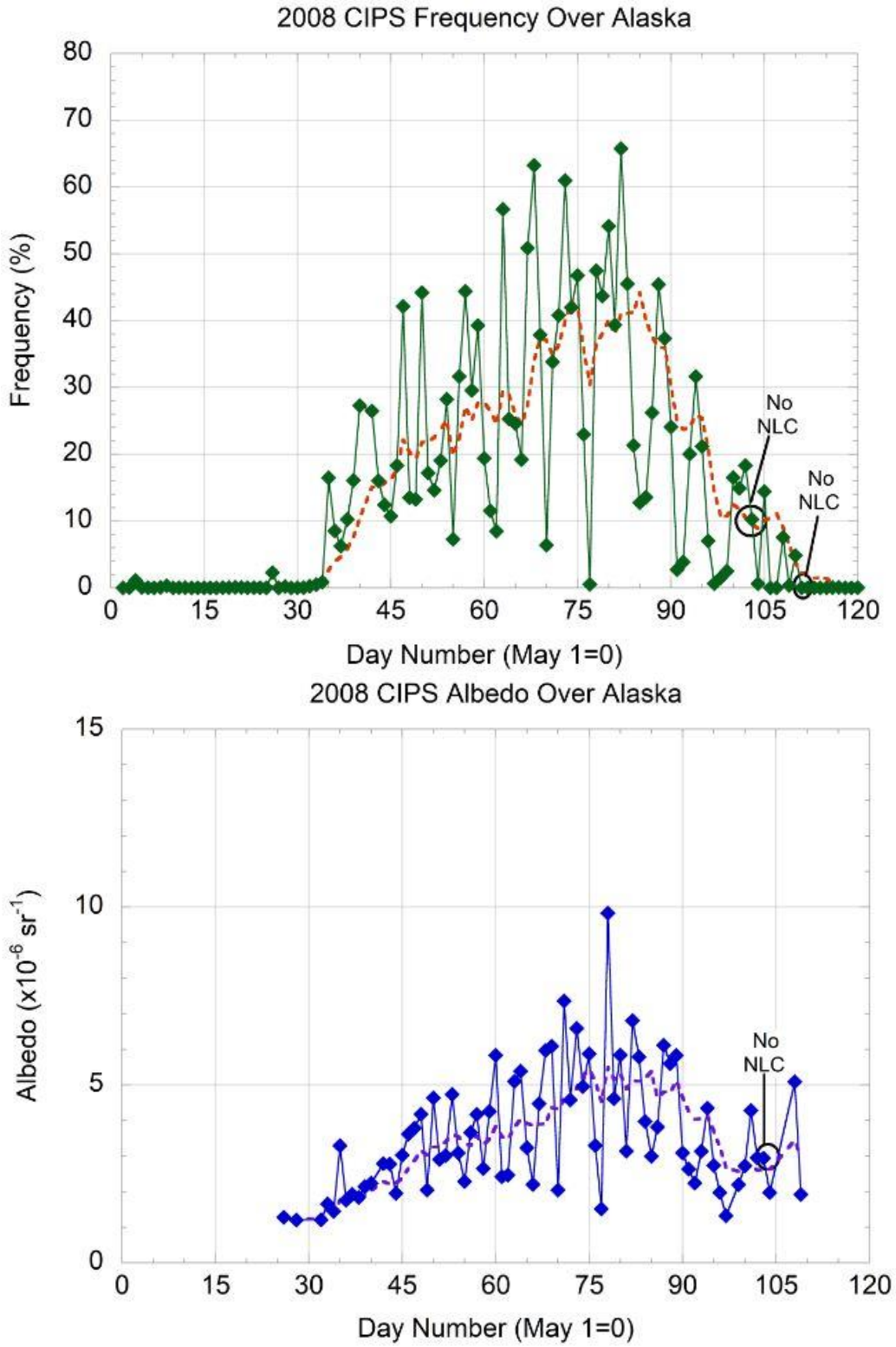

Figure 3.2b. CIPS frequency and albedo over Alaska (60-70°N, 130-170°W) during the 2008 NLC season. Nights of lidar observations are circled indicating positive or negative detections of NLCs.

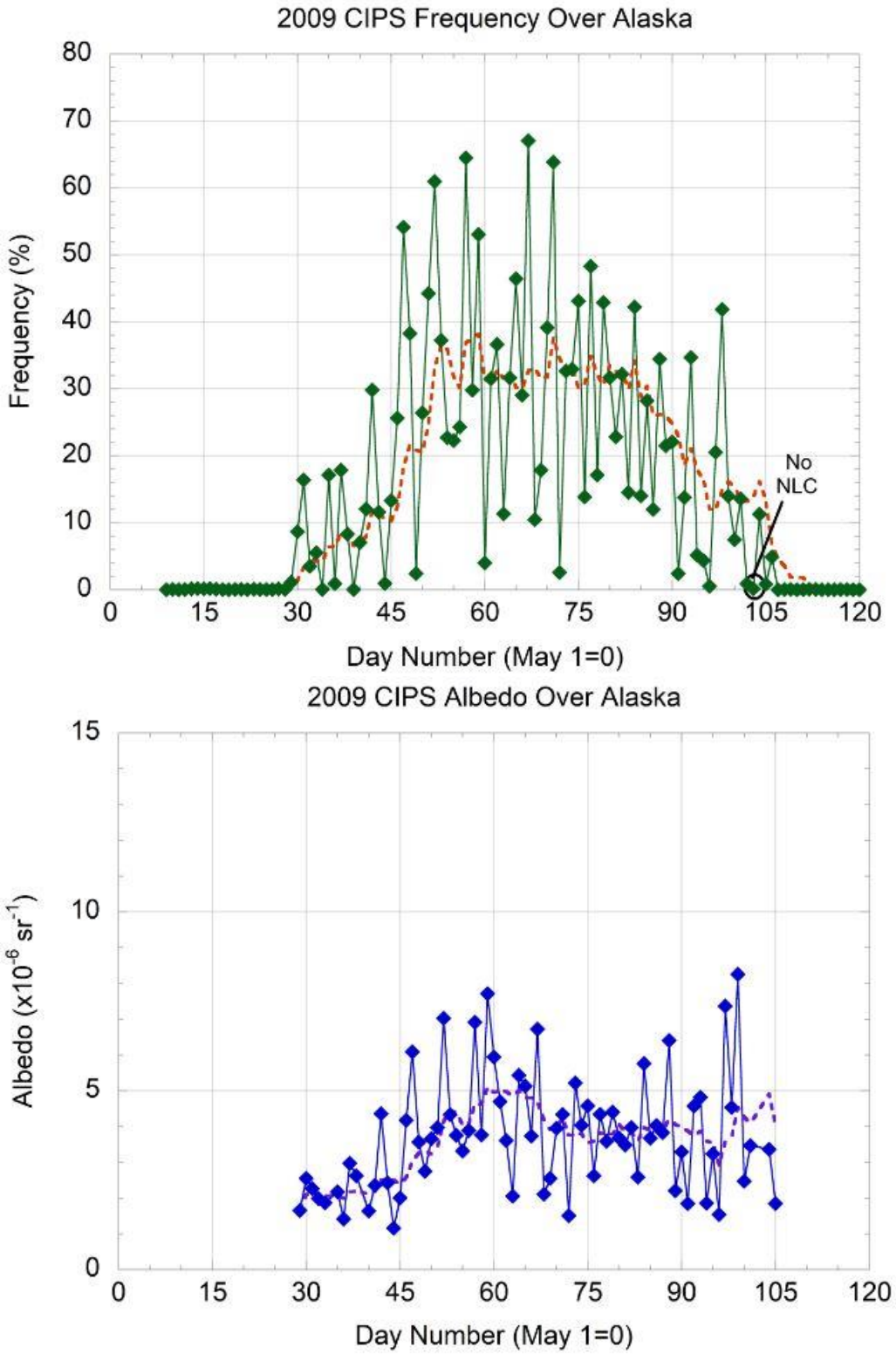

Figure 3.2c. CIPS frequency and albedo over Alaska (60-70°N, 130-170°W) during the 2009 NLC season. Nights of lidar observations are circled indicating positive or negative detections of NLCs.

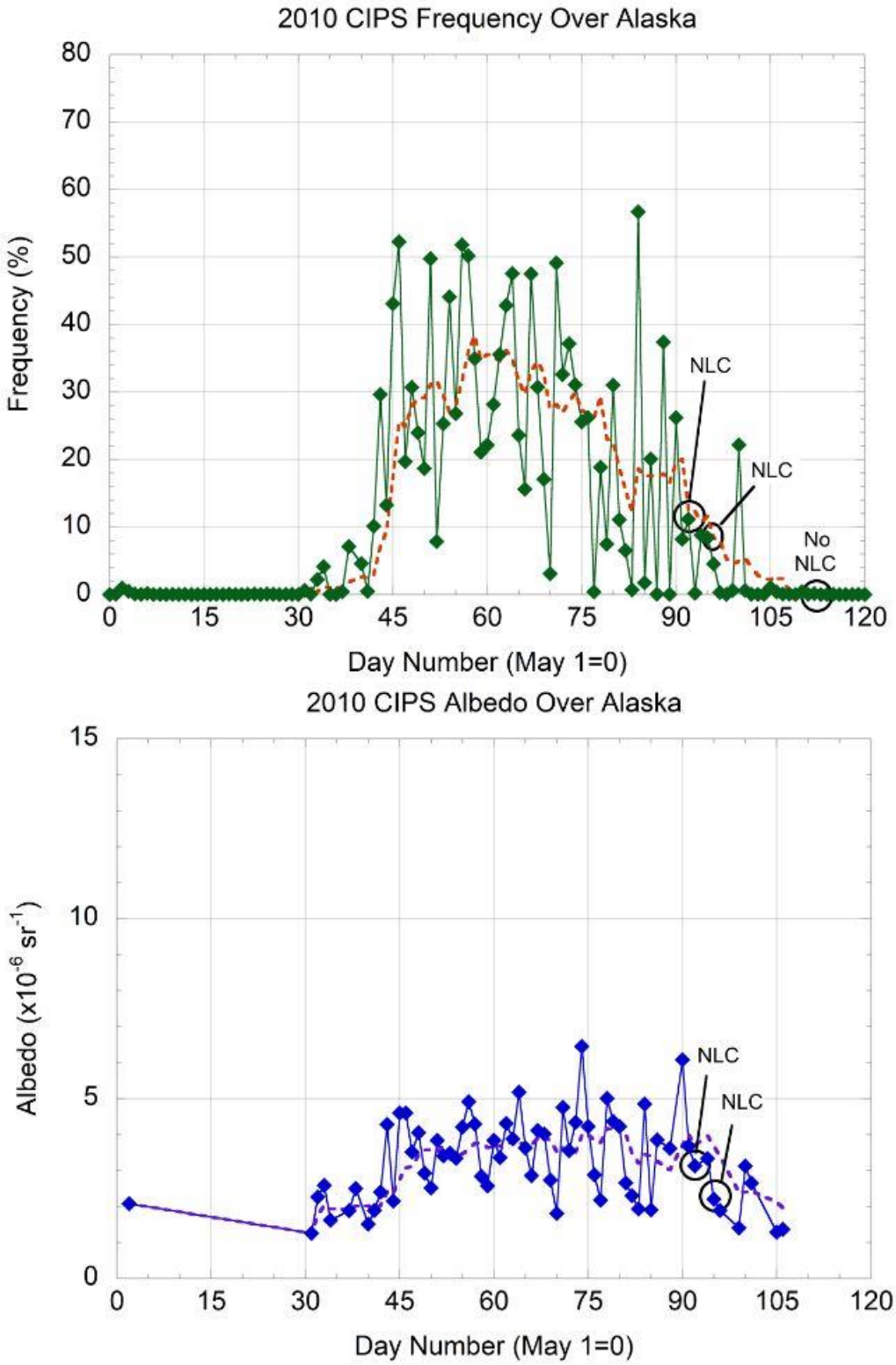

Figure 3.2d. CIPS frequency and albedo over Alaska (60-70°N, 130-170°W) during the 2010 NLC season. Nights of lidar observations are circled indicating positive or negative detections of NLCs.

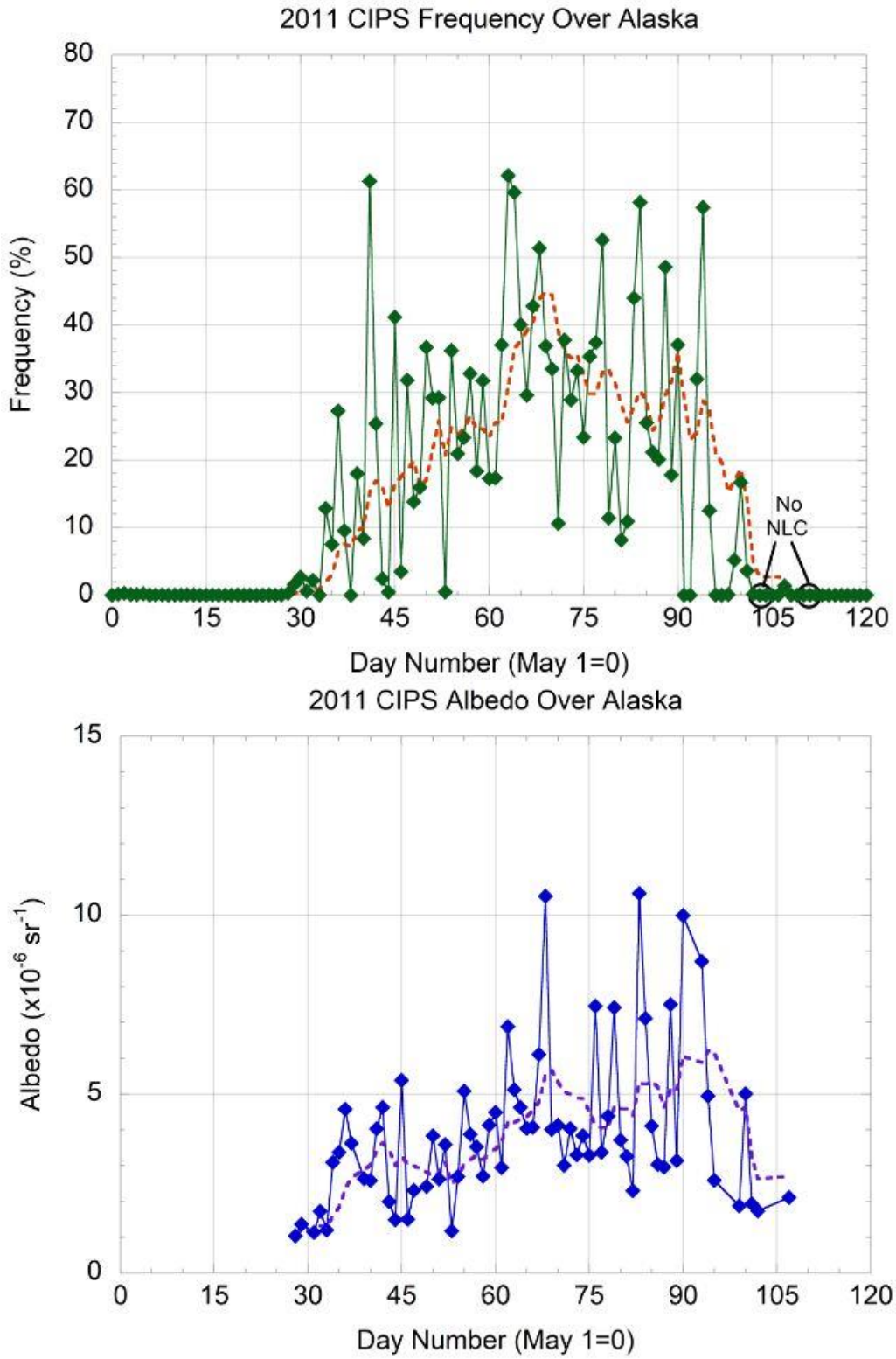

Figure 3.2e. CIPS frequency and albedo over Alaska (60-70°N, 130-170°W) during the 2011 NLC season. Nights of lidar observations are circled indicating positive or negative detections of NLCs.

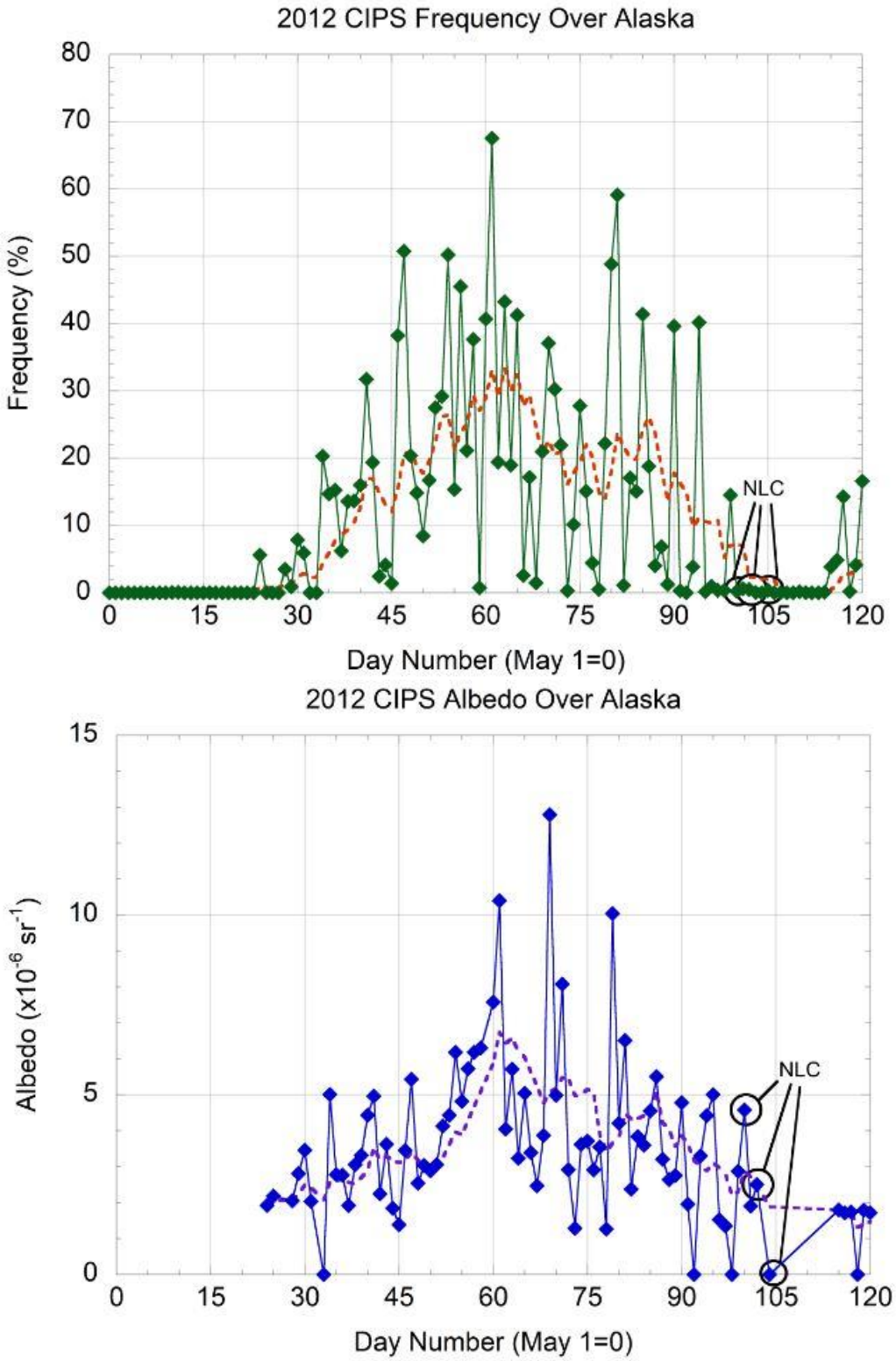

Figure 3.2f. CIPS frequency and albedo over Alaska (60-70°N, 130-170°W) during the 2012 NLC season. Nights of lidar observations are circled indicating positive or negative detections of NLCs.

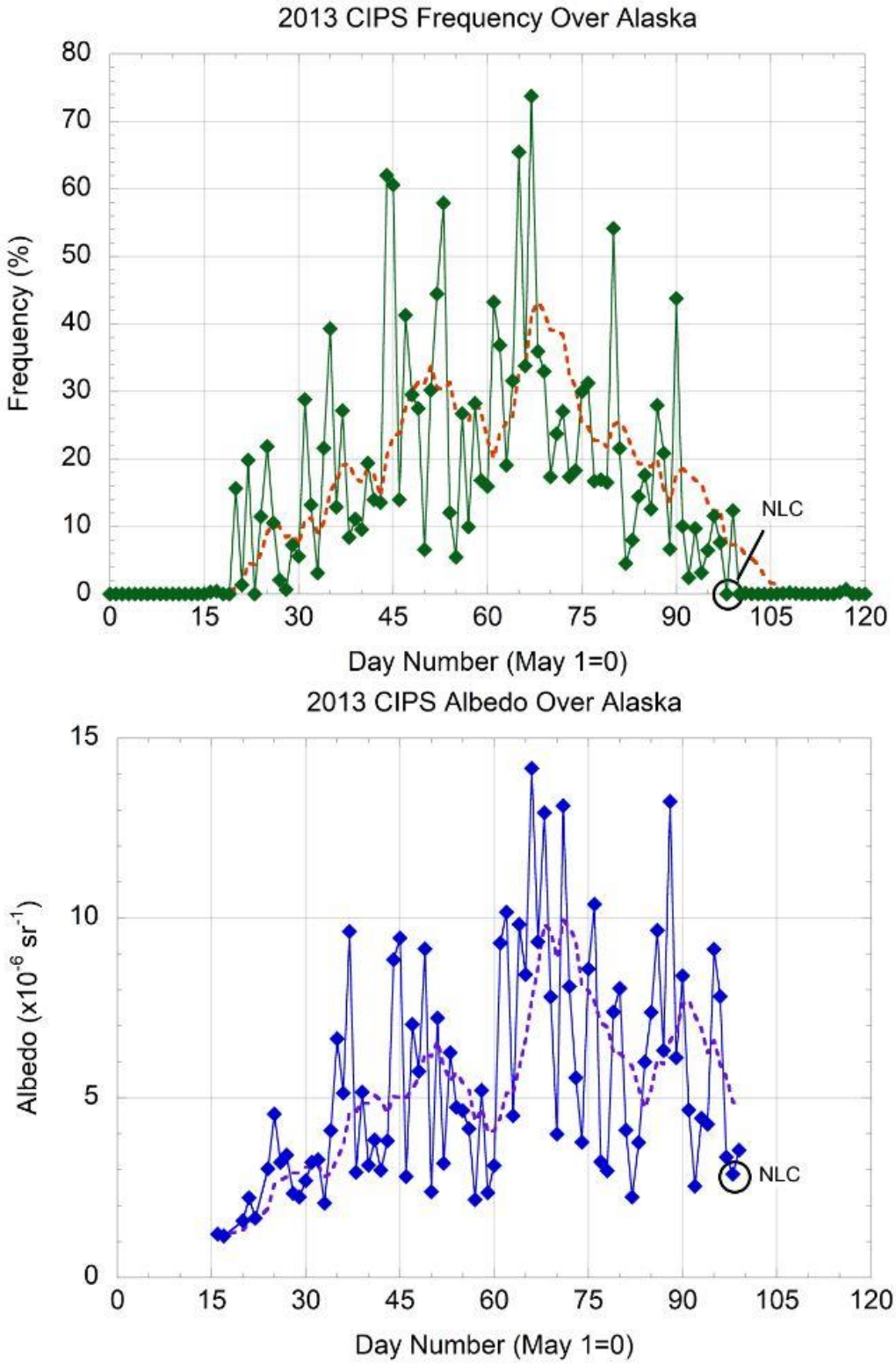

Figure 3.2g. CIPS frequency and albedo over Alaska (60-70°N, 130-170°W) during the 2013 NLC season. Nights of lidar observations are circled indicating positive or negative detections of NLCs.

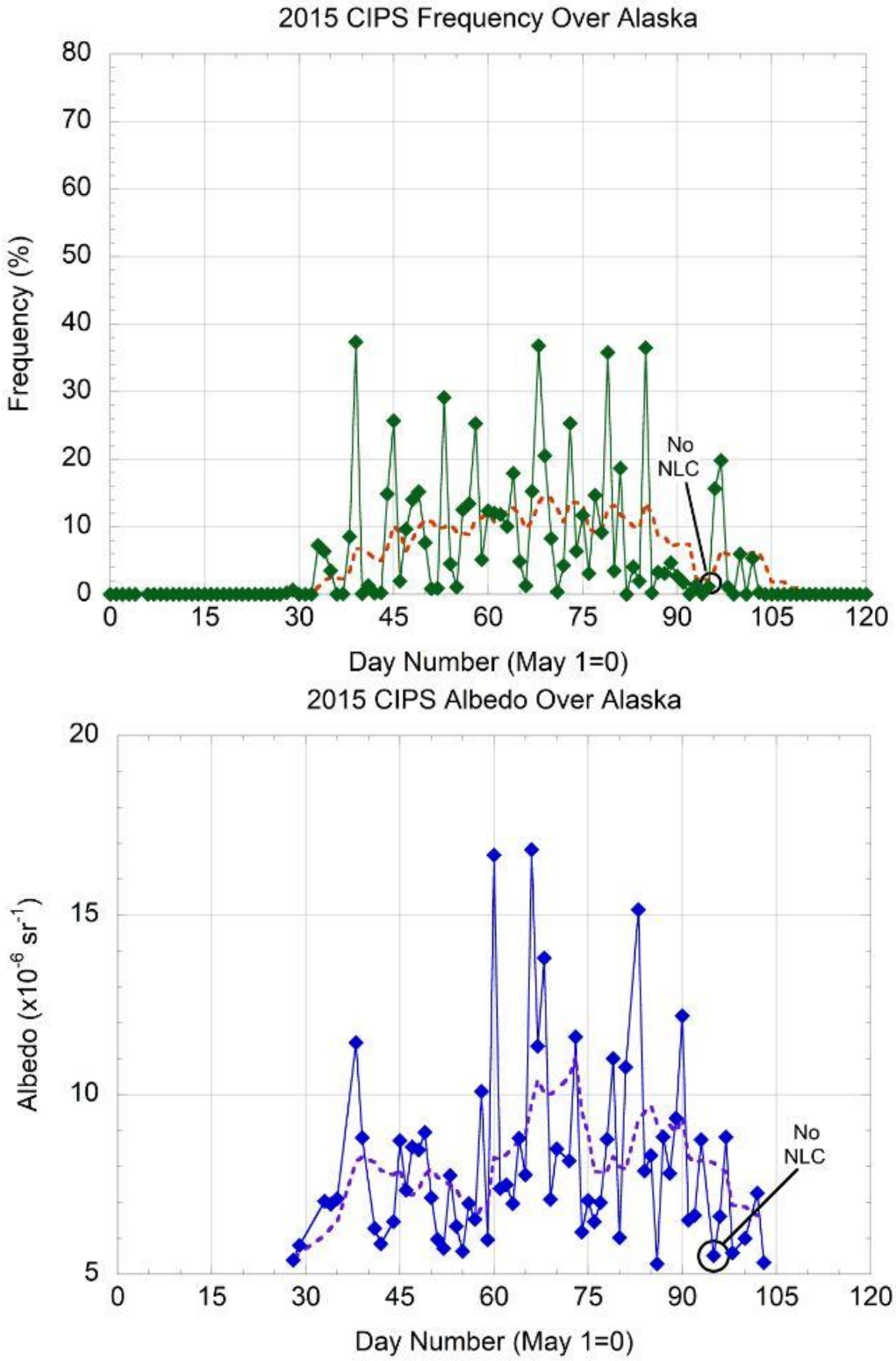

Figure 3.2h. CIPS frequency and albedo over Alaska (60-70°N, 130-170°W) during the 2015 NLC season. Nights of lidar observations are circled indicating positive or negative detections of NLCs.

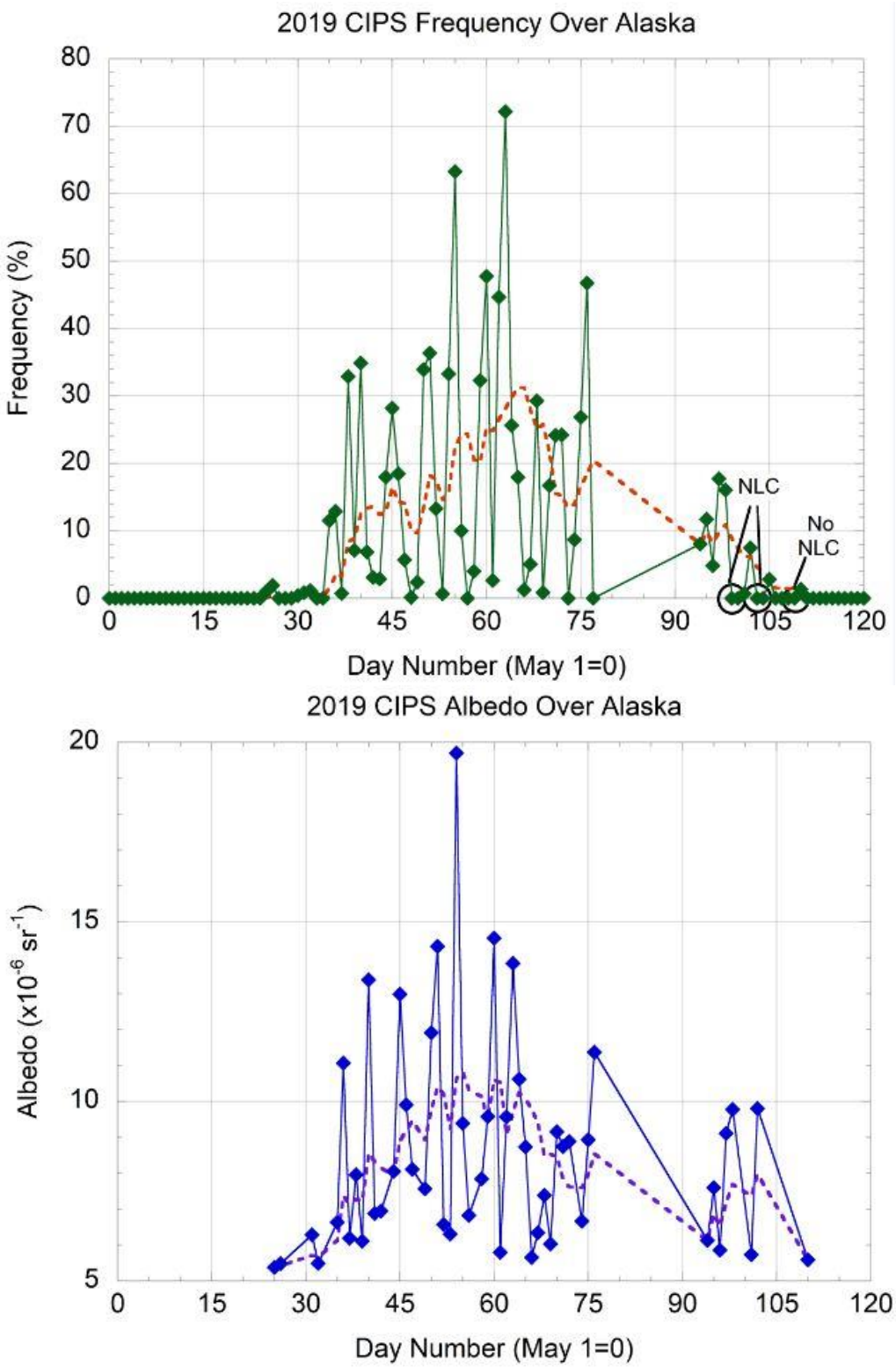

Figure 3.2i. CIPS frequency and albedo over Alaska (60-70°N, 130-170°W) during the 2019 NLC season. Nights of lidar observations are circled indicating positive or negative detections of NLCs.

There is only one event when the lidar did not detect an NLC when CIPS reports high NLC frequency and brightness. This one occurrence is on the night of August 11-12, 2008 when the lidar did not detect an NLC, but CIPS reports an NLC frequency of about 10% and a cloud albedo of about 3 G. This event reflects high NLC activity elsewhere over Alaska but not over Chatanika. There are six events when the lidar did detect an NLC when CIPS reports low NLC frequency. These occurrences are on the nights of August 8-9, 2012; August 10-11, 2012; August 13-12, 2012; August 6-7, 2013; August 7-8, 2019; and August 11-12, 2019. Three of these nights are interesting because the CIPS frequency is low (< 2%) but the CIPS albedo is between 3-5 G. The two nights in 2019 likely have near-zero values in CIPS frequency and albedo because of the high threshold (5 G) that is used in this year. The events when the lidar and CIPS do not correspond may reflect the difference in the single point measurement the lidar provides versus the broad coverage CIPS provides over Alaska.

3.3. The Microwave Limb Sounder (MLS) Instrument

The next analysis uses temperature and water vapor data from NASA's Earth Observing System (EOS) microwave limb sounder (MLS) instrument. MLS is a passive microwave remote sensor onboard the Aura satellite that measures temperature, geopotential height, and a set of atmospheric constituents. Aura was launched in July 2004 as part of the A-train in a sun-synchronous polar orbit at 705 km. Aura provides daily global coverage and makes about 14.5 orbits each day. The mission of Aura is to expand the understanding of the stratospheric ozone layer, climate change, and global air quality. MLS measures thermal emission from several broad spectral bands. In a passive remote sensor, the apparent brightness temperature at a particular frequency is due to

contributions from both the temperature of the atmosphere and from the concentration of the atmospheric constituent. Measurements of the brightness temperature vary with changes in both atmospheric temperature and the constituent concentration. An emission line corresponding to a uniformly-mixed atmospheric gas is used to determine the temperature [Woodhouse, 2006]. Then this temperature is used as a baseline to retrieve the concentrations of the constituents from other emission lines. In the Aura MLS, the 118 GHz oxygen line is used to retrieve temperature measurements, and the 190 Ghz line is used to retrieve H2O mixing ratios. The MLS temperature product is retrieved from 261-0.001 hPa (~9-90 km). The MLS H2O product is retrieved from 316-0.002 hPa (~8-87 km). Other MLS data products include BrO, CH3Cl, CH3CN, CH3OH, ClO, CO, geopotential height, HCl, HCN, HNO3, HO2, HOCl, ice water content, ice water path, N2O, O3, OH, relative humidity, and SO2. The data products are given by 55 pressure levels.

3.4. MLS Analysis

NLCs are highly sensitive to changes in temperature and humidity. In order for an ice cloud to form, the atmosphere must be supersatured. Supersaturation occurs when the water vapor pressure exceeds the equilibrium water vapor pressure. The equilibrium water vapor pressure increases as temperature increases. The summer polar mesosphere is a unique place in the atmosphere where the water vapor concentration is extremely low (< 10 ppmv), but where temperatures reach such cold extremes that ice cloud formation can occur. Fluctuations in the temperature and water vapor impact how readily the ice clouds can form.

Previously, temperatures during NLC lidar observations at Chatanika were assumed from seasonal climatological profiles in order to estimate the water vapor environment [Collins et al., 2009; Collins et al., 2003]. In this analysis, MLS temperature and water vapor data is used to investigate the meteorological conditions in the mesosphere during all NLC lidar observations at Chatanika since Aura's launch in 2004. The MLS temperature and water vapor data is screened according to the MLS data quality document [Livesey et al., 2018]. The 0.0046 hPa level data corresponds to about 83.5 km and is used for all the MLS analyses in this chapter. Figure 3.3 shows a single profile of MLS temperature data and a single profile of MLS water vapor data from August 12, 2019 at 64.7° N and 140.9° W to illustrate the vertical resolution of MLS. Pressure has been converted to approximate altitude by assuming hydrostatic equilibrium and integrating downward in pressure (upward in altitude) from the MLS pressure level closest to the ground.

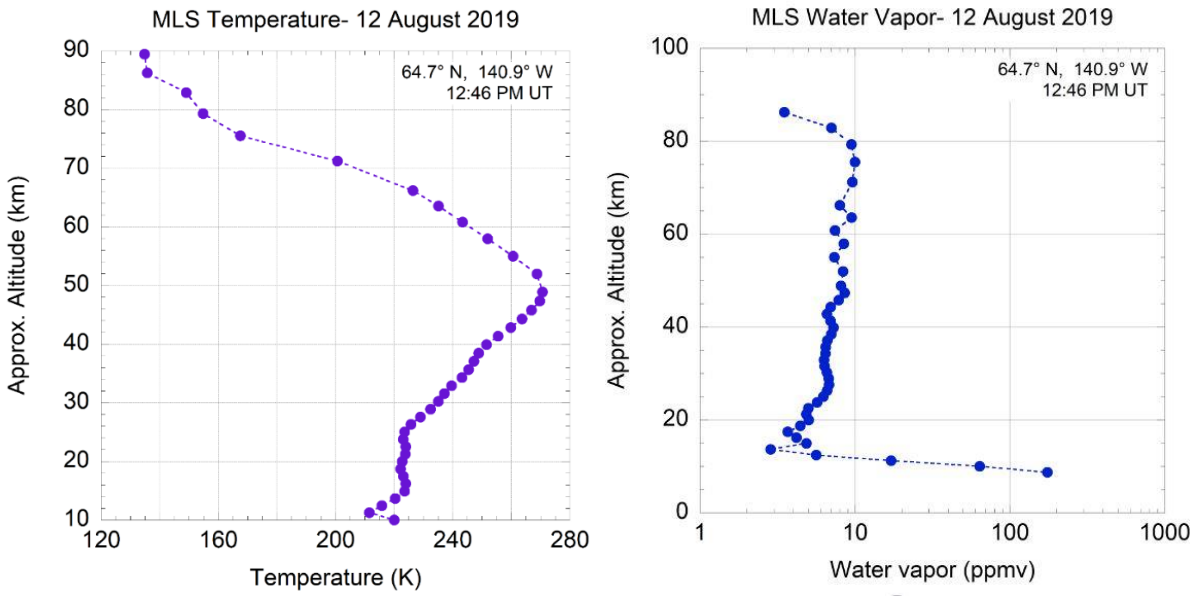

Figure 3.3. A single MLS temperature profile (left) and a single MLS water vapor profile (right) on 12 August 2019 at 64.7° N and 140.9° W. The MLS pressure levels have been converted to approximate altitudes.

A preliminary analysis was first done to examine the temperature and water vapor anomalies across the NLC season to determine where the NLC lidar observations occurred within the seasonal variations in temperature and water vapor. For the temperature and water vapor anomaly study, the MLS descending node (~03:00 LST, 12:00 UT) data was averaged over 62-68° N and 140-154° W for each night. Some of the very bright NLCs occurred during or just after local minima in temperature compared to the surrounding days. Temperature fluctuations up to 8 K were seen between days throughout the NLC season. Also, fluctuations in water vapor of over 3 ppmv were seen between days throughout the season. Figure 3.4 shows the temperature and water vapor anomalies for the 2007 NLC season with a 7-day running mean over-plotted as the dotted line. NLCs were observed by the lidar at Chatanika on the night of August 10-11, 2007 and August 16-17, 2007. The water vapor levels on both nights of the lidar observations are near the seasonal average water vapor. Both nights of lidar observations appear to be during a local cooling compared to the surrounding nights. However, it became clear that the insights from looking at anomalies alone are limited without contextualizing what such changes in temperature and water vapor mean for cloud formation. This led to frost point calculations being included in the next analyses.

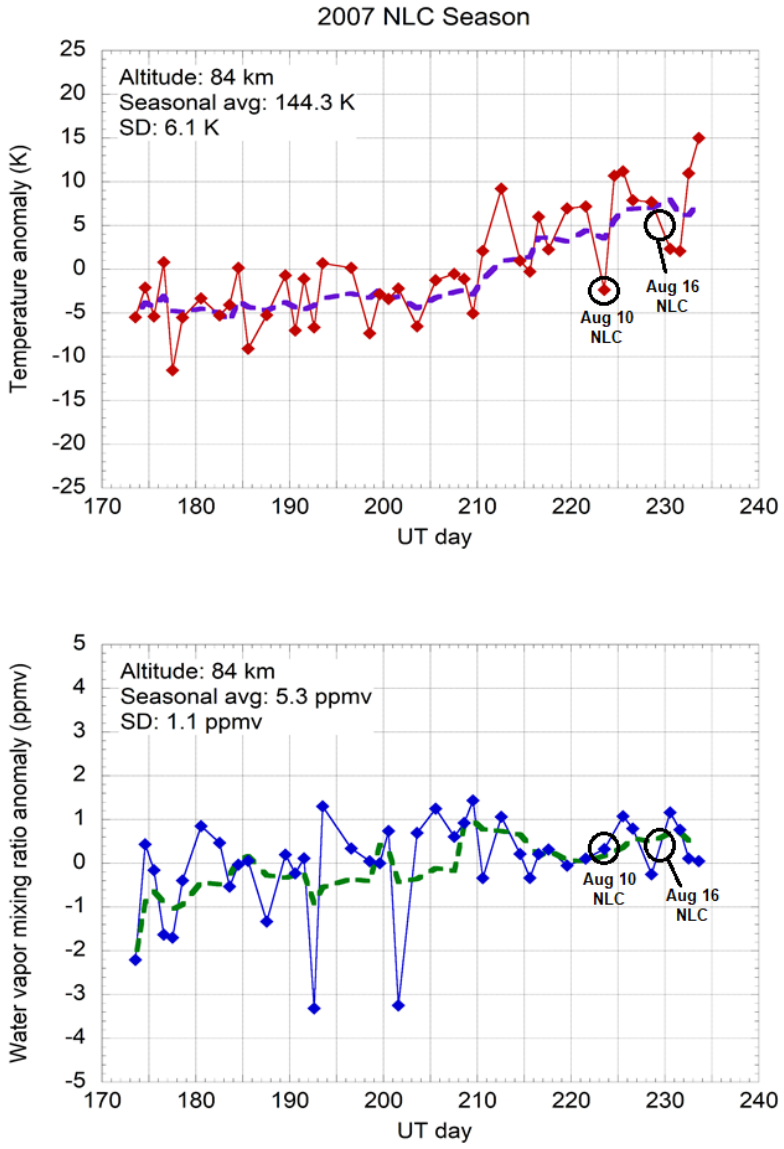

Figure 3.4. MLS temperature and water vapor anomalies over Alaska (averaged over 62-68° N, 140-154° W) during the 2007 NLC season. The two lidar observations that detected an NLC are circled.

The frost point temperature is the temperature at which the vapor pressure of water vapor over ice is equal to the ambient water partial pressure. The frost point equation from Murphy and Koop is adopted for this analysis,

$$T_{frost} \approx (1.814625\ln(p_w) + 6190.134)/(29.120 - \ln(p_w)) \text{ for T>115K} \quad (3.1)$$

where p_w is the ambient water partial pressure [Murphy and Koop, 2005].

For the next analysis, MLS data is not averaged over a region, but instead the closest data point to Chatanika is taken at the 64.7° N latitude that is also closest to the lidar observation time. The method of taking the closest MLS data point to a ground-based observation station has been used in previous NLC studies [Dalin et al., 2011]. Of the 41 high quality lidar observations identified in Chapter 2, 31 lidar observations overlap with MLS operating years since Aura's launch in 2004. Figure 3.5 shows the temperature and water vapor mixing ratios for each of the 31 overlapping lidar observations. Figures 3.6a-m show the temperature and frost point temperature from May 1-August 31 for each summer when lidar observations were conducted at Chatanika. Nights of lidar observations are labeled according to whether NLCs were or were not detected. At the beginning of May, the water vapor concentration is typically very low (< 1 ppmv) and hence, the frost point temperature is low, meaning that unusually cold temperatures are required for ice formation. This early in the season, the temperatures are as warm as 180 K. As the summer progresses into solstice, the water vapor concentration increases to a few ppmv and the temperatures decrease to as low as 130 K. From the beginning of June to the middle of August, temperatures frequently reach below the frost point. The lidar observations occur in the first few weeks of August, when temperatures are increasing after solstice and the frequency of sub-frost-point conditions is decreasing.

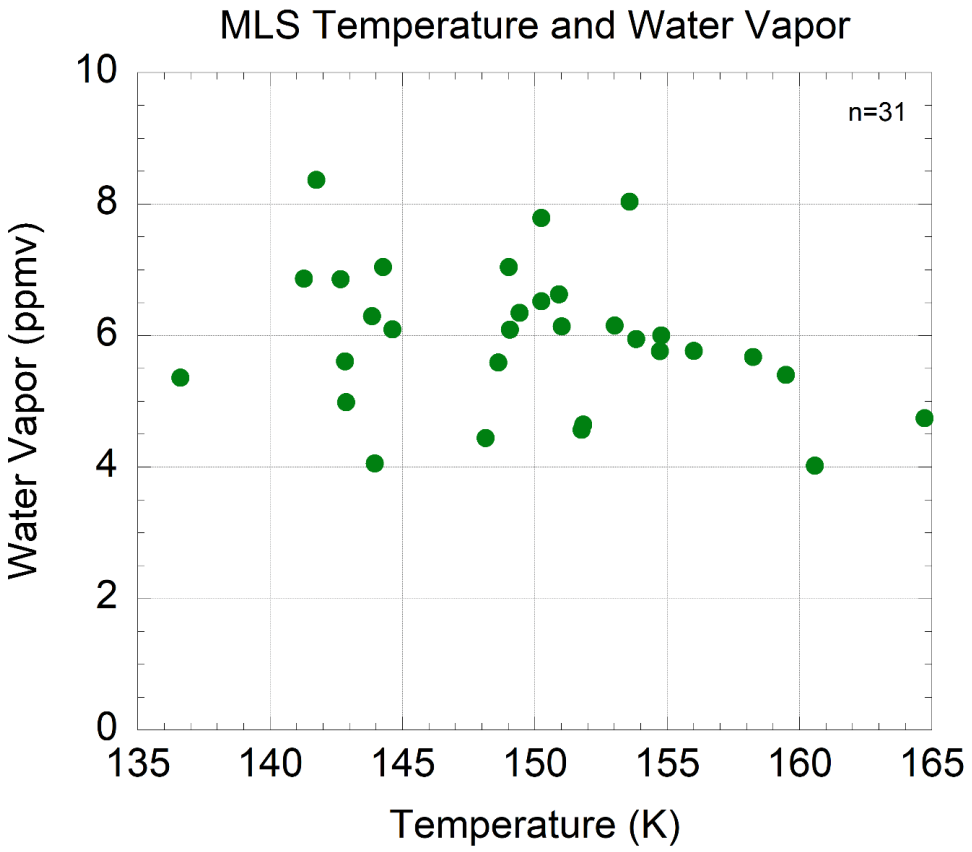

Figure 3.5. MLS temperature and water vapor mixing ratios during 31 lidar observations from NLC seasons in 2005-2019.

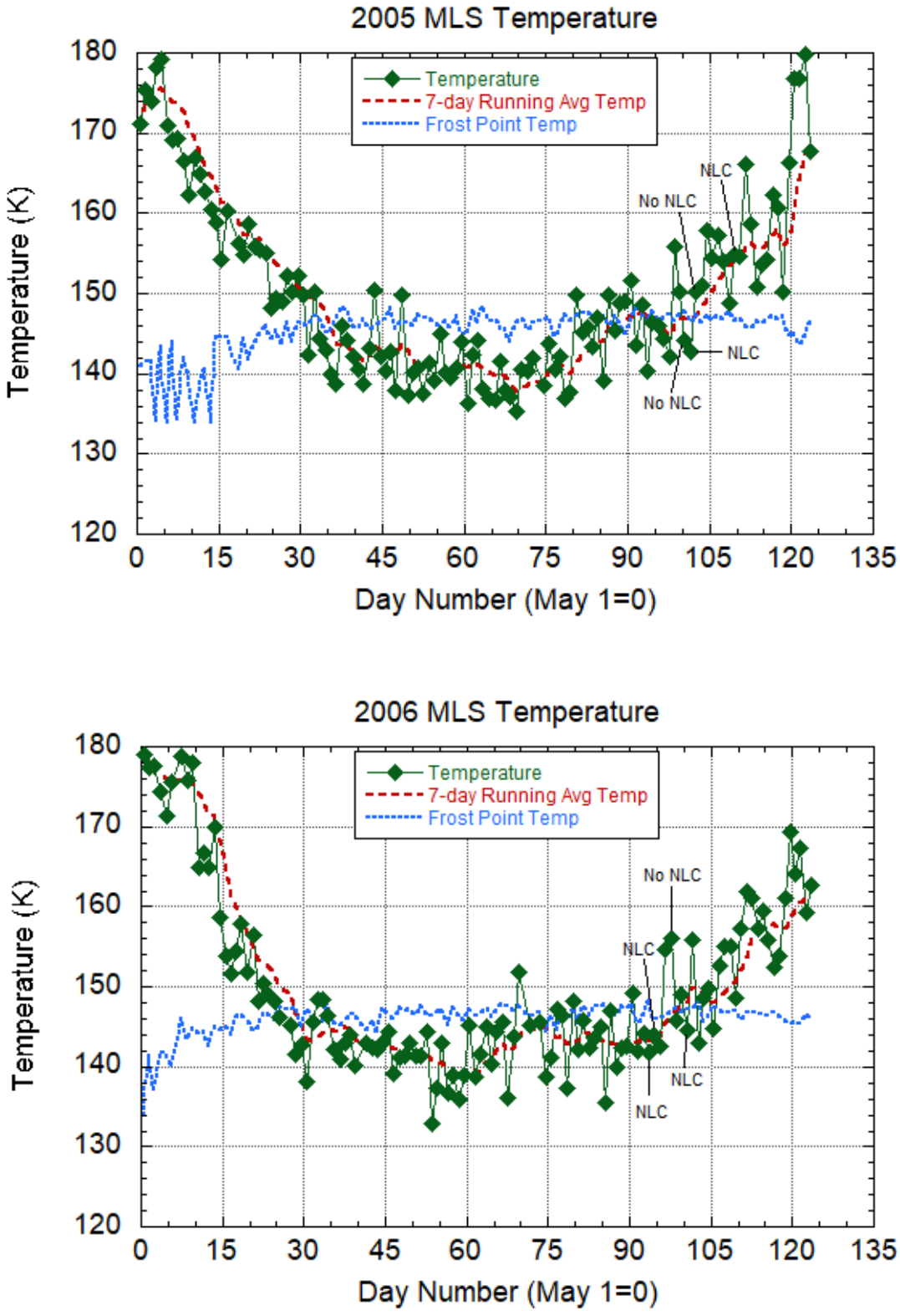

Figure 3.6a.,b. MLS temperature and frost point temperature near Chatanika at 64.7° N during summer 2005 (top) and summer 2006 (bottom).

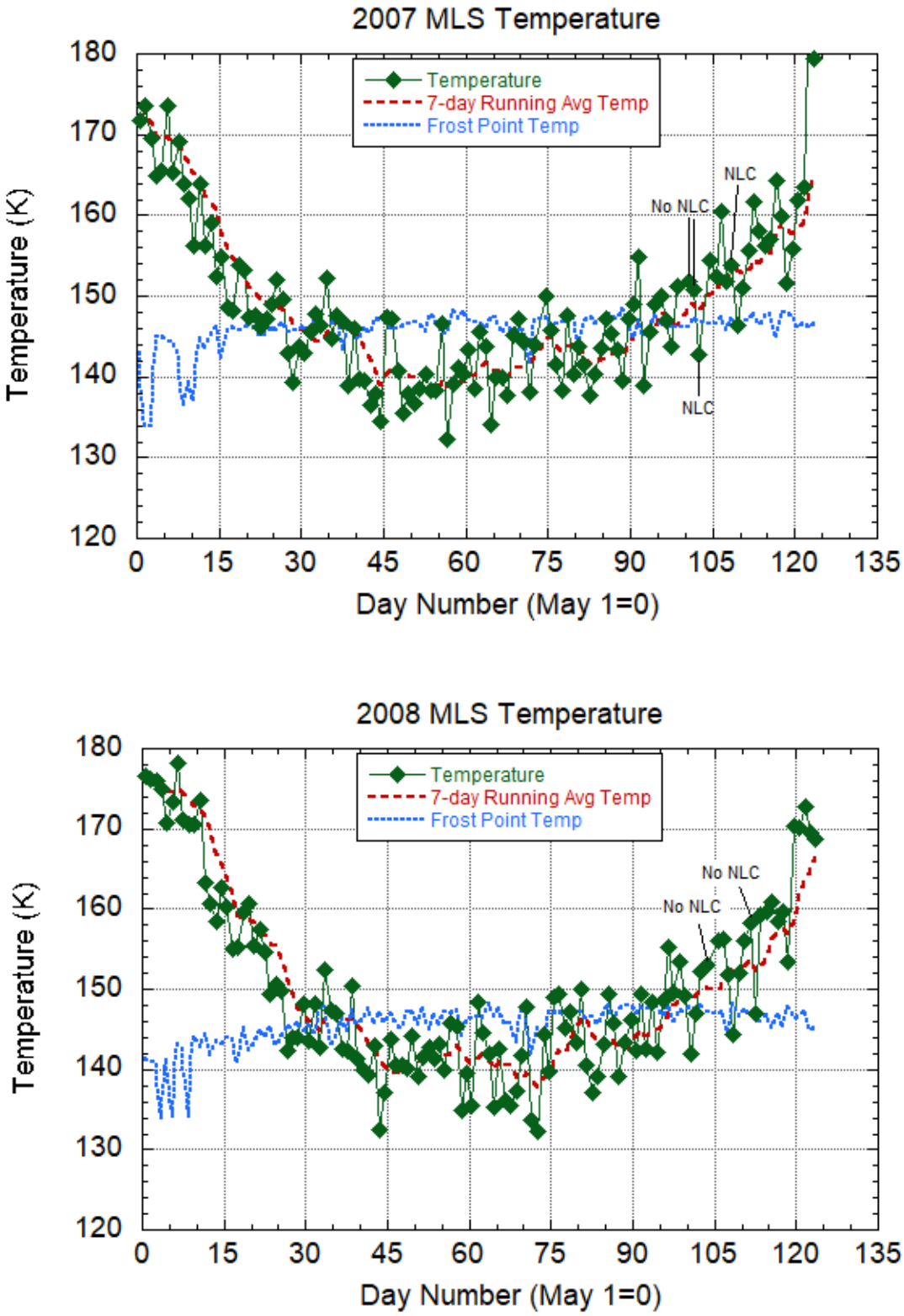

Figure 3.6c.,d. MLS temperature and frost point temperature near Chatanika at 64.7° N during summer 2007 (top) and summer 2008 (bottom).

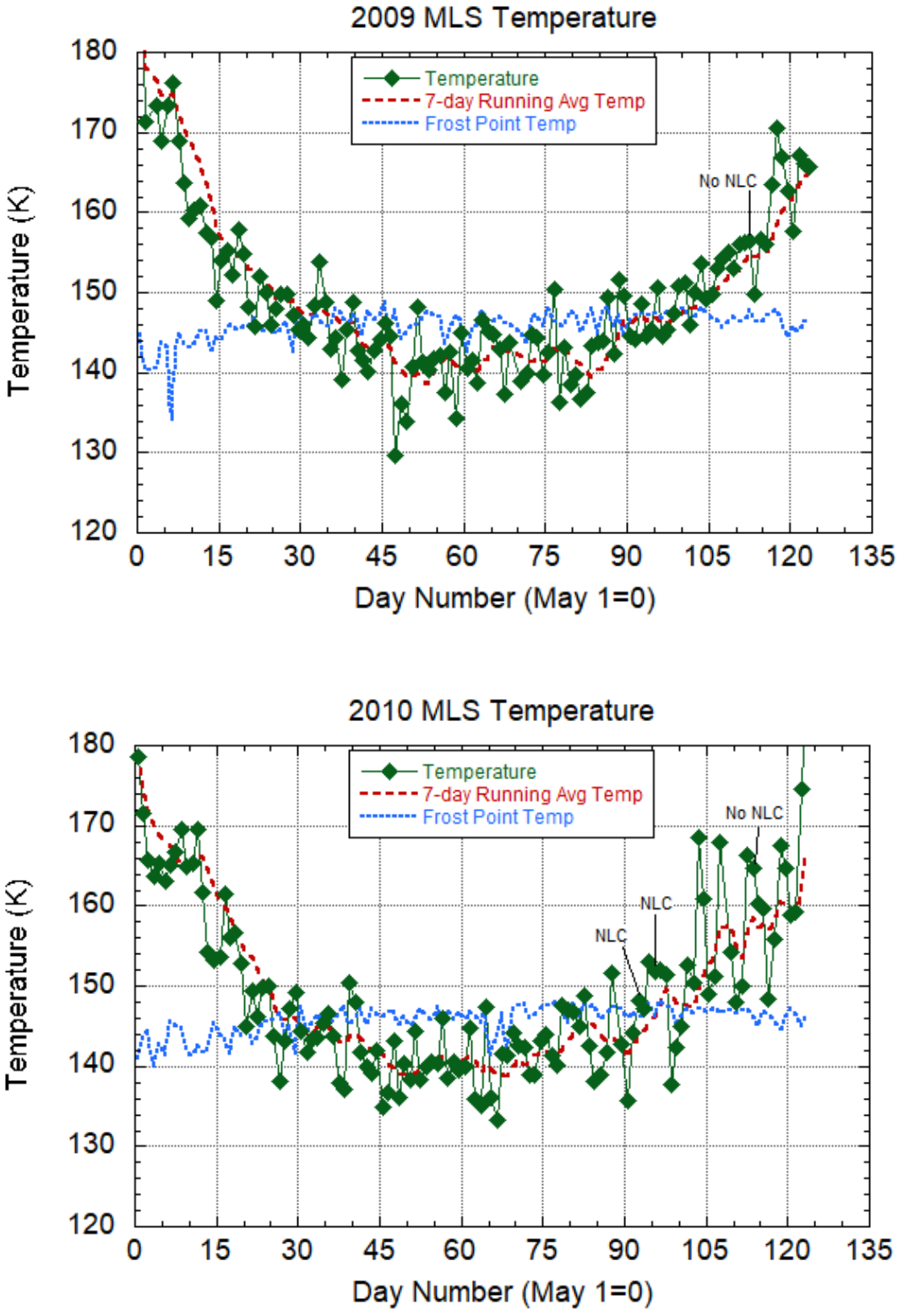

Figure 3.6e.,f. MLS temperature and frost point temperature near Chatanika at 64.7° N during summer 2009 (top) and summer 2010 (bottom).

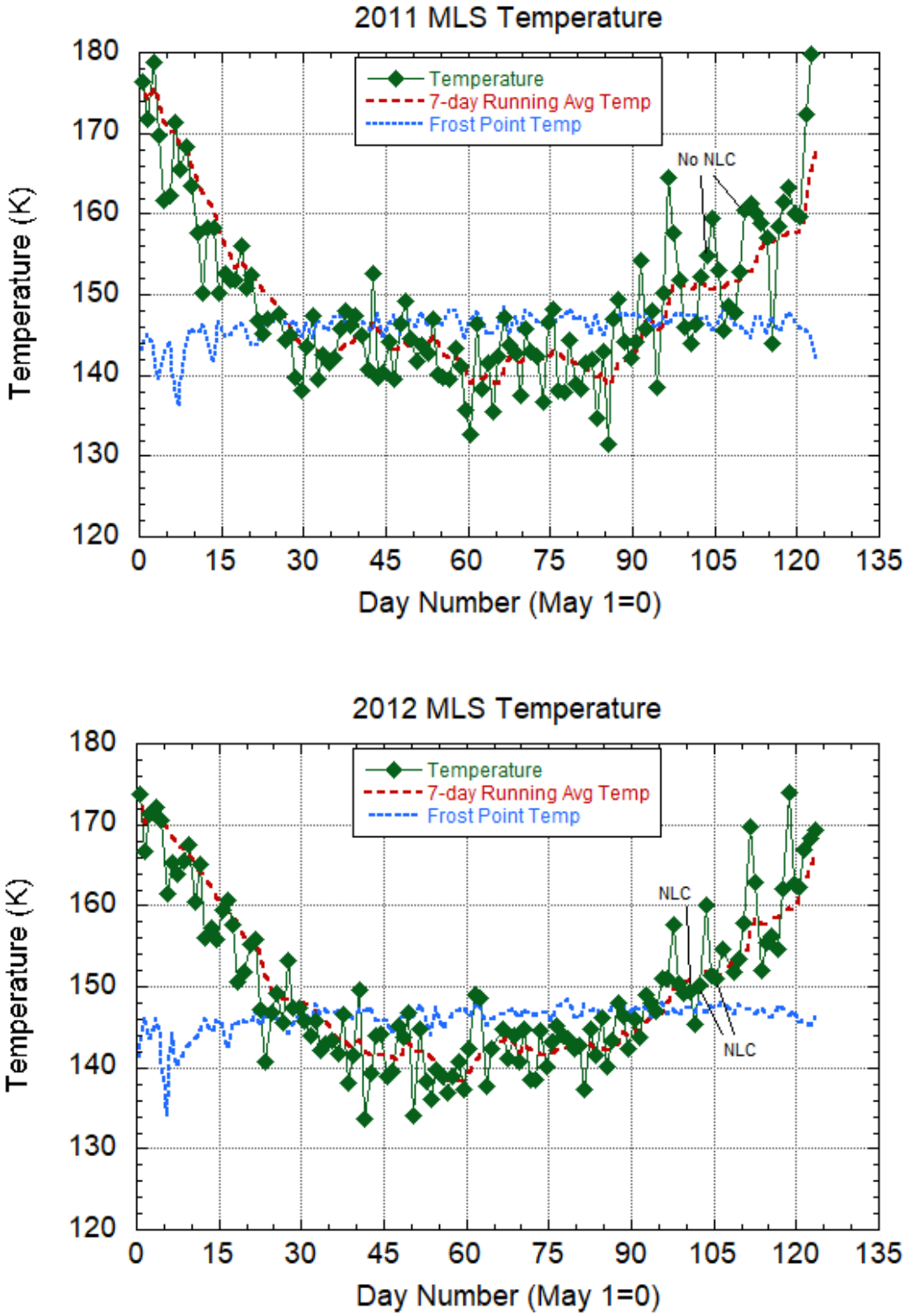

Figure 3.6g.,h. MLS temperature and frost point temperature near Chatanika at 64.7° N during summer 2011 (top) and summer 2012 (bottom).

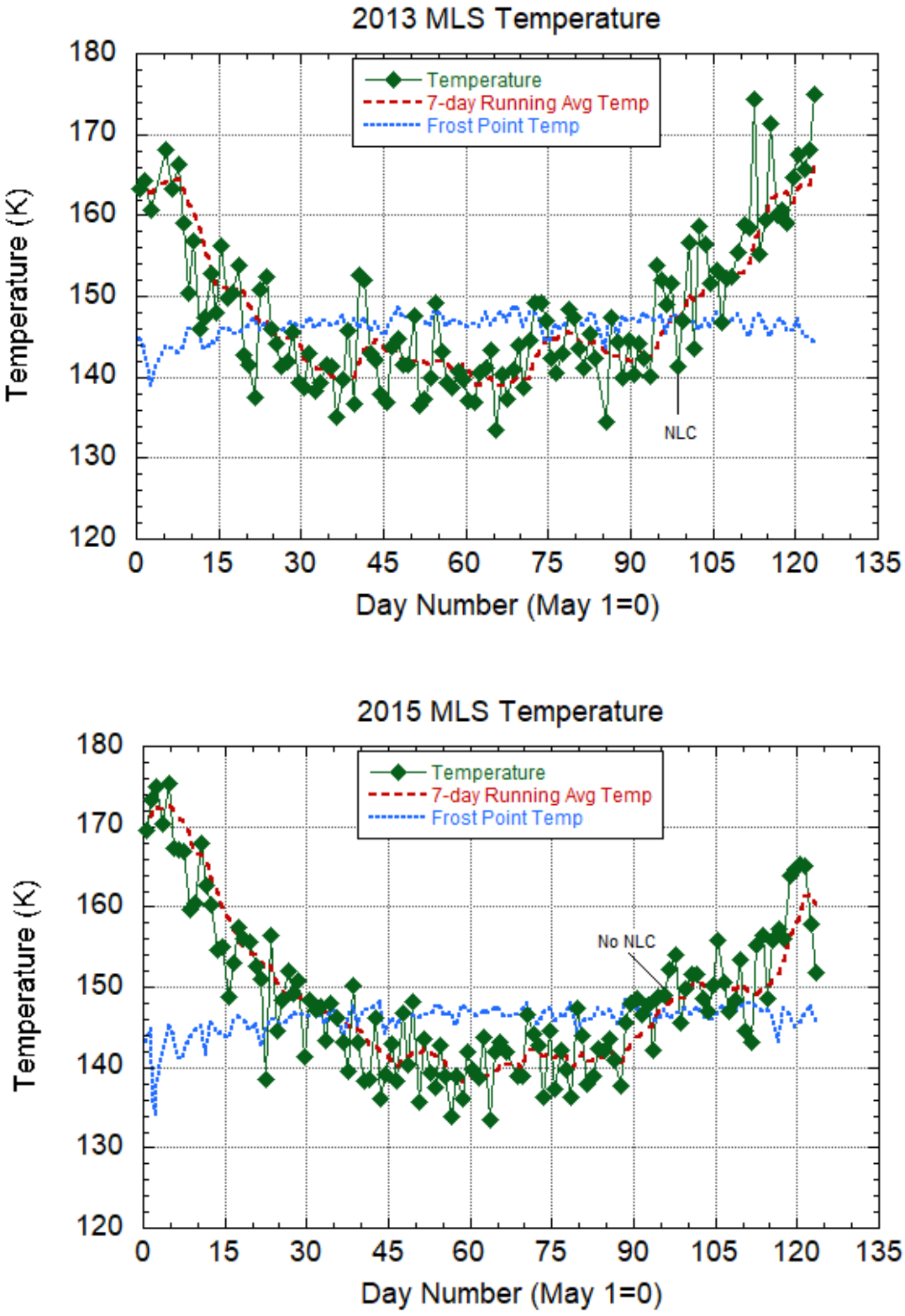

Figure 3.6i.,j. MLS temperature and frost point temperature near Chatanika at 64.7° N during summer 2013 (top) and summer 2015 (bottom).

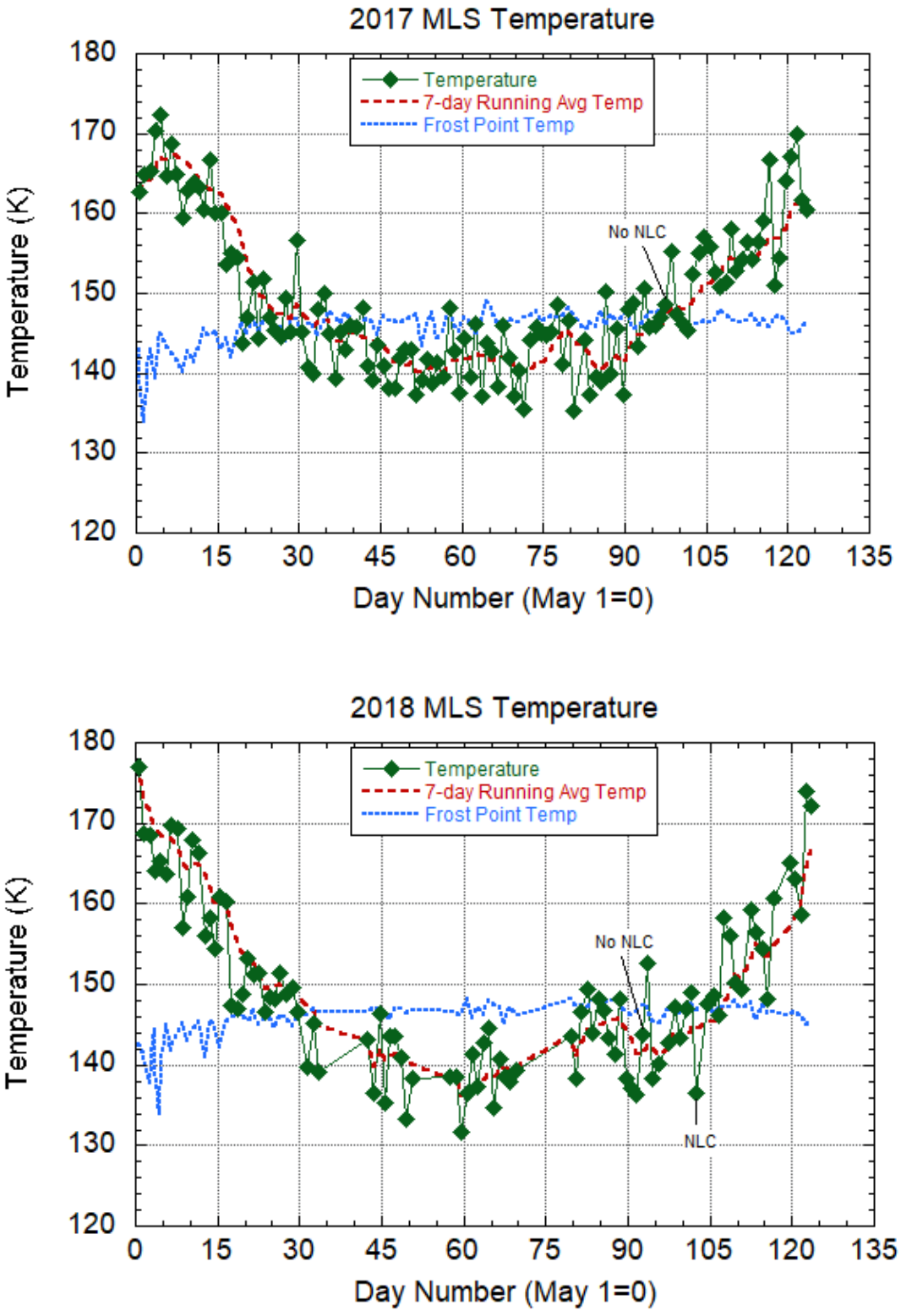

Figure 3.6j.,k. MLS temperature and frost point temperature near Chatanika at 64.7° N during summer 2017 (top) and summer 2018 (bottom).

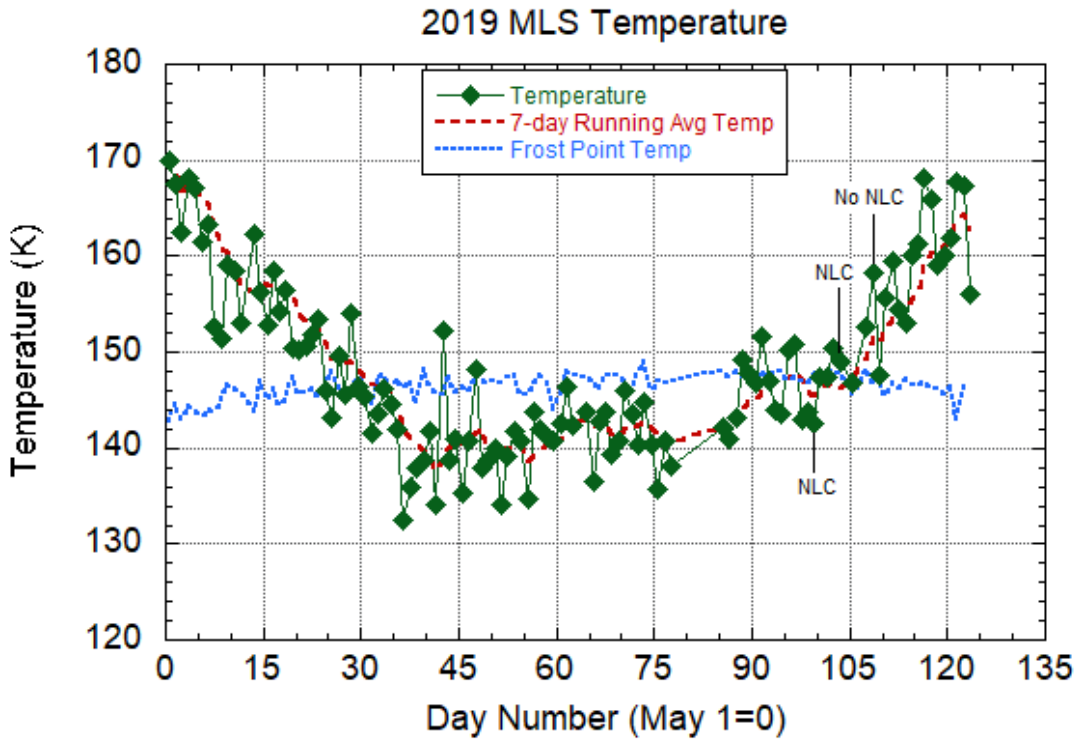

Figure 3.6m. MLS temperature and frost point temperature near Chatanika at 64.7° N during summer 2019.

Next, the distribution of lidar observations according to temperature, water vapor, and temperature relative to the frost point is investigated. The MLS water vapor mixing ratio varies between 4 ppmv and 9 ppmv for the 31 nights of lidar observations overlapping with MLS, yielding frost point temperatures between 146 K and 148 K. This range of frost point temperature agrees with other frost point analyses in the mesosphere [Dalin et al., 2011]. Figures 3.7a-c. show the distribution of lidar observations relative to temperature, water vapor, and temperature deviation from the frost point. The lidar observations are separated by three categories. *No NLC* indicates observations where NLCs were not detected by the lidar and were not visible in the sky. *NLC* indicates the

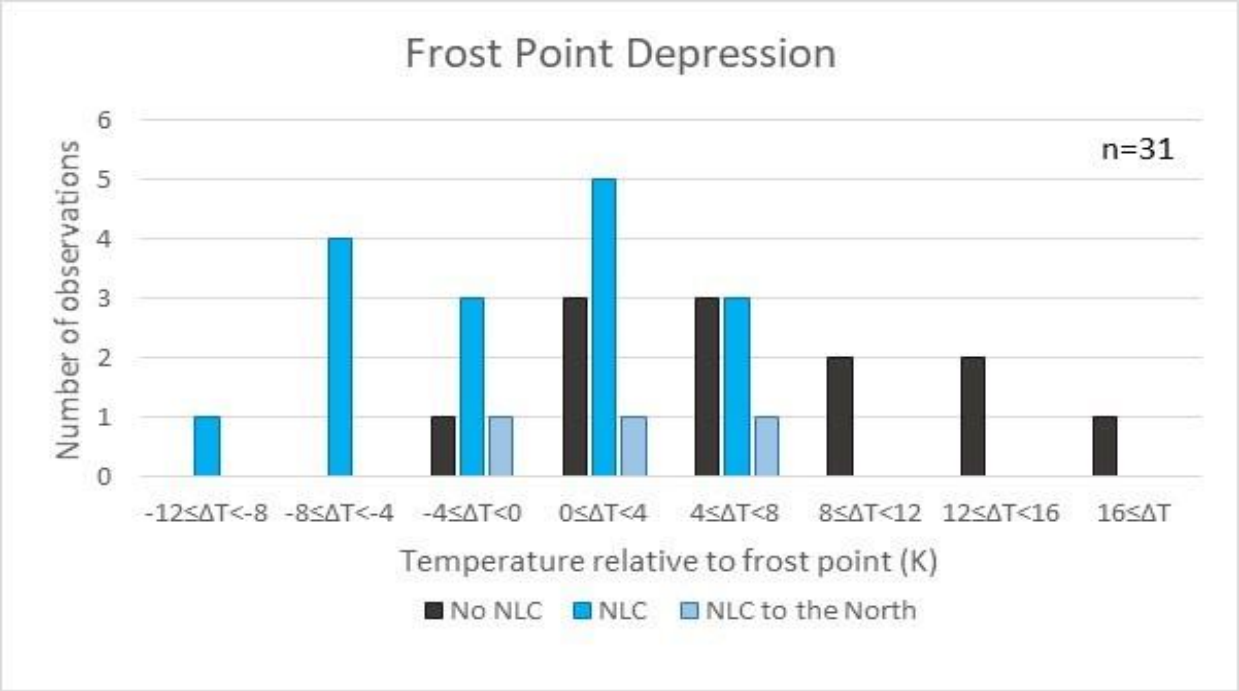

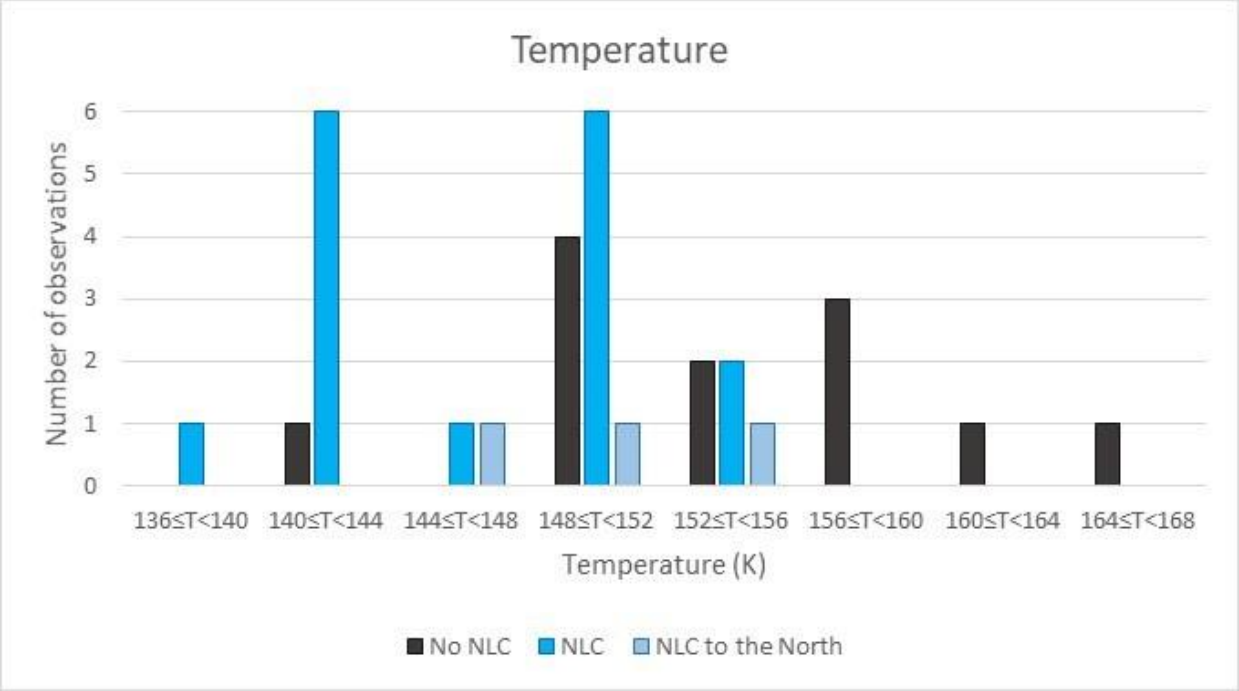

Figure 3.7a. (top) Distribution of Poker Flat lidar observations with frost point depression determined by MLS temperature and water vapor data at 64.7°N. Figure 3.7b. (bottom) Distribution of Poker Flat lidar observations with MLS temperature at 64.7°N.

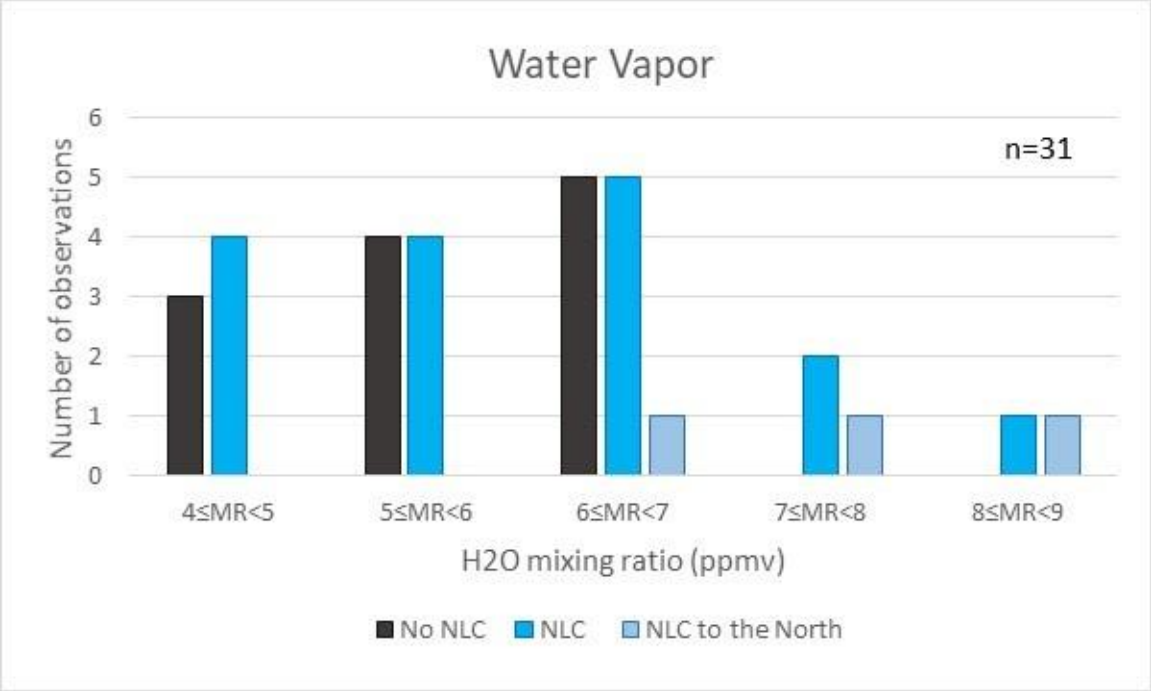

Figure 3.7c. Distribution of Poker Flat lidar observations with MLS water vapor at 64.7°N.

observations where NLCs were detected by the lidar. *NLC to the North* indicates that NLCs were not detected by the lidar but were visible in the sky to the north by ground observers at PFRR. The distribution between these categories is clearest in the histogram of frost point depression. Nights with high temperatures relative to the frost point (>8 K above) only correspond to lidar observations where NLCs are absent. Nights with low temperatures relative to the frost point (>4 K below) only correspond to lidar observations where NLCs are present. There is an intermediate range just above and below the frost point temperature where NLCs are both present and absent. In the distribution of lidar observations with temperature alone, the distinction between the categories of observations is not as obvious as in frost point depression. This points to the roles of both temperature and water vapor, which are included in the frost point depression calculation, having an impact on NLC occurrence. With the MLS water vapor mixing ratio varying only between 4 ppmv and 9 ppmv and the uncertainty being 2 ppmv, it is difficult to determine

the water vapor impact on the NLC occurrence in the lidar data. Still, it is worth noting that the five nights with very high water vapor levels (>7 ppmv) all correspond to observations where NLCs were present at or near PFRR.

Since it is evident that frost point depression impacts NLC occurrence, the next question is whether frost point depression impacts the brightness of NLCs detected by lidar at Chatanika. To investigate this impact, the maximum IBC and average IBC for the 16 significant IBC clouds since 2004 are plotted in Figure 3.8a and Figure 3.8b with the MLS temperature relative to the frost point on the night of the lidar observation. Errors in the frost point depression are shown as the horizontal bars. No strong relation is seen between cloud brightness and frost point depression. NLCs of varying brightness exist both above and below the frost point, and the weak NLCs exist at a large range of temperatures relative to the frost point. However, the small number of lidar observations may prevent a clear relation from being detected.

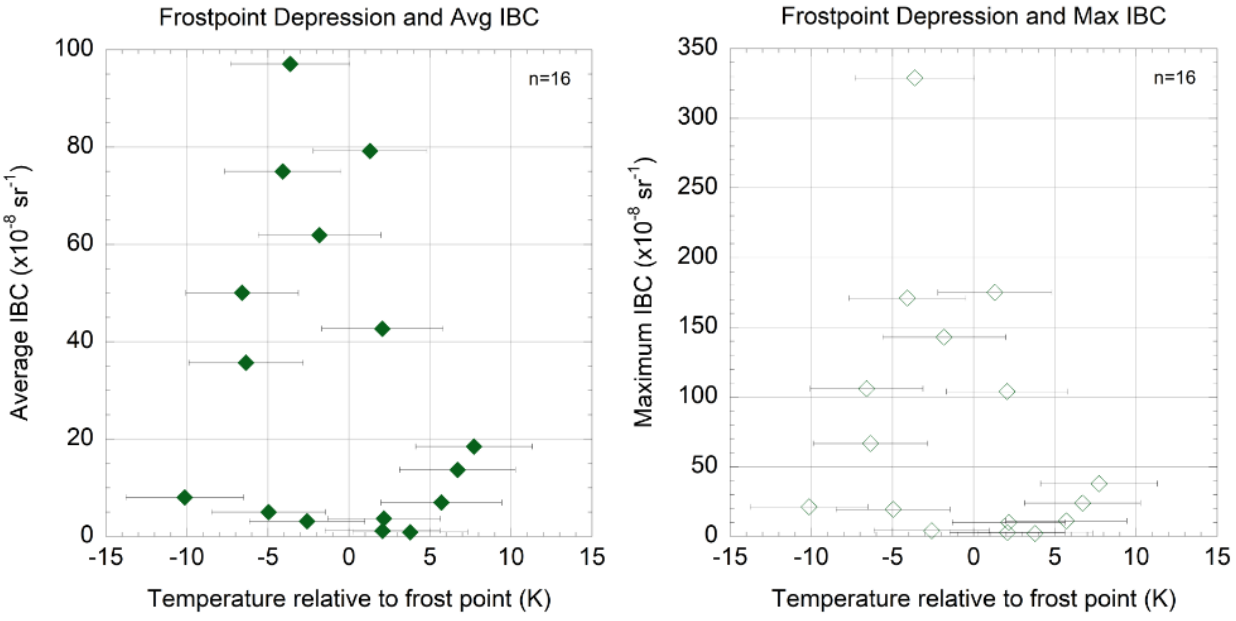

Figure 3.8a. (left) MLS frost point depression and average IBC for 16 NLCs detected by lidar at Chatanika. Figure 3.8b. (right) MLS frost point depression and maximum IBC for 16 NLCs detected by lidar at Chatanika.

Wind data during past NLC lidar observations motivates the next part of the analysis, which is built upon the transport of the clouds from their source location. A meteor wind radar was established at PFRR in 2018 and operated during the 2019 NLC season. During the night of the very bright and extensive NLC display on August 11-12, 2019, the meteor wind radar measured strong southwestward winds which peaked in the hour before the NLC was first detected by the lidar. Figure 3.9 shows the hourly zonal and meridional wind speeds measured by the meteor wind radar at 82 km. The wind data provides insight into what was seen by ground observers at PFRR on the night of the NLC detection on August 11-12, 2019. The NLC was first visible in the northeastern sky nearly 1 hour before the first detection by lidar, and NLC structure was subsequently seen moving southward toward the lidar lab. During the lidar observations on August 9-10, 2005, a medium frequency radar also measured southwestward winds, and ground observations and camera observations showed the NLC structure moving southwestward towards the lidar lab [Collins et al., 2009]. The radar wind, camera observations, and ground observations from 2005 and 2019 illustrate the role of the southwestward wind in transporting northern NLCs towards PFRR.

The dynamic of southwestward transport of NLCs from the north extends the spatial range of meteorological conditions that is relevant to the NLCs detected by lidar at Chatanika. The southwestward wind varied from 35 m/s to 60 m/s (130 km/h to 220 km/h) during the NLC observation on the night of August 11-12, 2019. Considering these wind speeds and that the NLC was observed continuously for 3.5 hours, the horizontal extent of the cloud was likely several hundred kilometers (~450-770 km). This means that the source region of the cloud could have been several hundred kilometers to the north.

Therefore, in the next analysis, a series of MLS data points to the north of Chatanika are examined for each night of NLC observation to investigate the meteorological conditions at those locations.

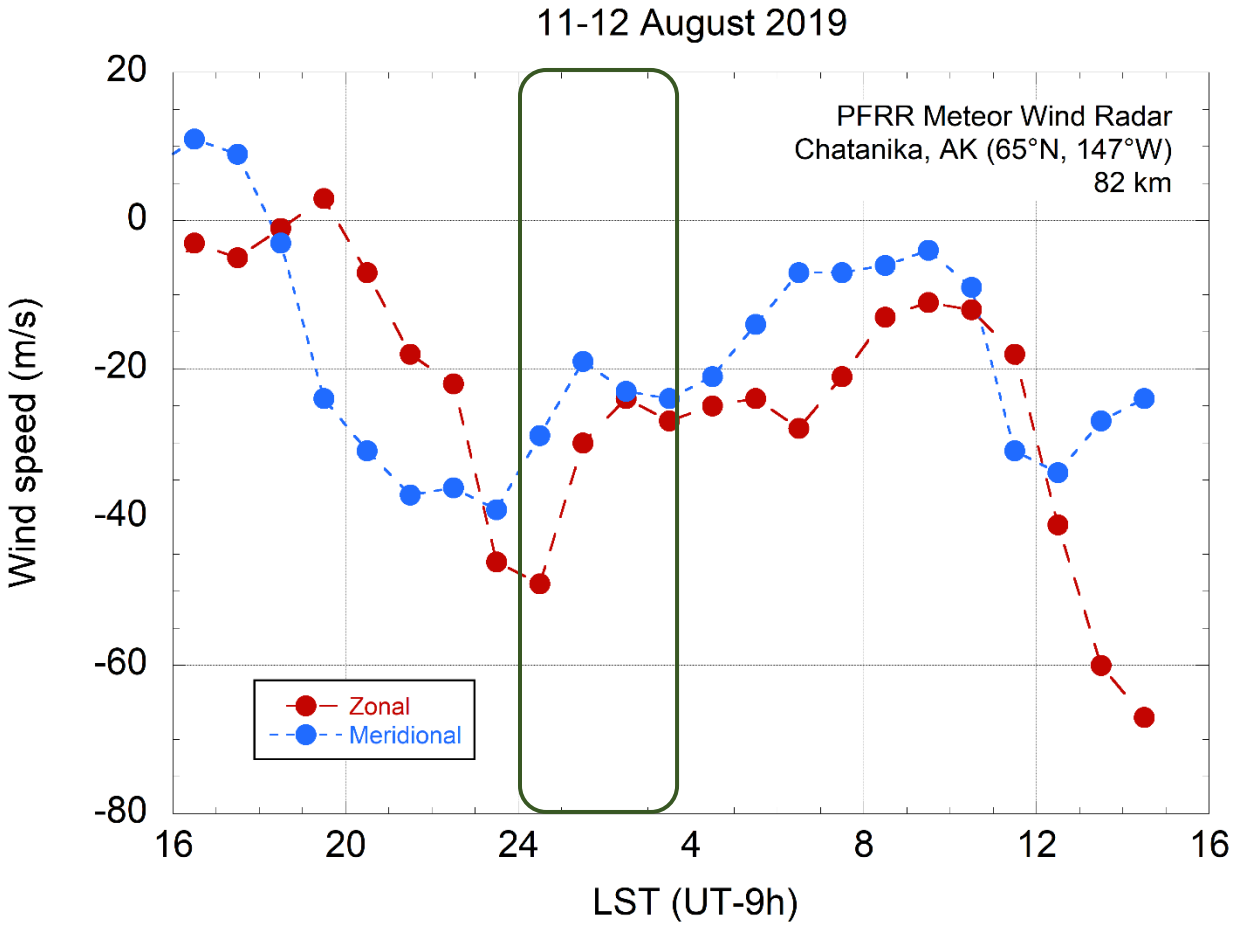

Figure 3.9. Zonal and meridional wind speeds measured at 82 km by the Poker Flat meteor wind radar on the night of 11-12 August 2019. The green outline shows the time of the NLC detection by lidar.

The previous analysis examined temperature relative to the frost point temperature, which is calculated using the MLS H2O product. In the next step, the analysis is posed in terms of the ambient water vapor present relative to the equilibrium water vapor condition at each location north of Chatanika. Environmental stability is assessed at each point, in terms of whether an ice cloud at that location would be in a supersatured, equilibrium, or subsaturated (unstable) condition. The MLS temperature is used to calculate the water vapor pressure over ice according to the equation presented by Murphy and Koop,

$$p_{ice} = \exp\left(9.550426 - \frac{5723.265}{T} + 3.53068\, ln(T) - 0.00728332T\right) \qquad \text{for T>110K}$$

where T is temperature in Kelvin and p_{ice} is the vapor pressure of ice in Pa [Murphy and Koop, 2005].

The Aura satellite's descending node travels southwestward in latitude over Alaska each day in the early morning (~03:00-05:00 LST). The stability analysis presented here uses the MLS data points that are part of the same track as the closest data point to Chatanika that was used in the previous frost point depression analysis. The track point locations are separated by about 1.4° in latitude. A total of 5 track points from 64.7-70.3° N are analyzed. For each latitude track point, the maximum IBC of the NLC detected by the Rayleigh lidar is plotted against the equilibrium water vapor mixing ratio and the MLS water vapor mixing ratio. Three stability conditions are defined as the following: *Supersaturated* indicates that the nominal MLS H2O and its lower bound is greater than the equilibrium H2O. *Equilibrium* indicates that the equilibrium H2O value is within the uncertainty bounds of the MLS H2O value. *Subsaturated* indicates that the nominal MLS H2O and its upper bound is less than the equilibrium H2O value.

Figure 3.10a shows the water vapor equilibrium plot for the first latitude track at 64.7° N. Of the 16 clouds, seven are considered supersaturated, one is in equilibrium, and eight are subsaturated. Most of the weak clouds (max IBC<50x10^{-8} sr^{-1}) are considered subsaturated, and there are six clouds where the conditions require very high water vapor for equilibrium. Such high water vapor concentrations are not present naturally in the mesosphere. It is possible that these weak clouds may not have been stable at the time they were detected by lidar over Chatanika. At the second track at 66.1° N (Figure 3.10b), there are six clouds in supersaturation, four more clouds (five total) in equilibrium conditions than before, and five clouds in subsaturation. Also, there are now only four unusually high equilibrium water vapor levels (>10 ppmv). Moving to the third track at 67.5° N (Figure 3.10c), there are seven clouds in supersaturation, seven clouds in equilibrium, and only two clouds in subsaturation. At the fourth track at 68.9° N (Figure 3.10d), there are eight clouds in supersaturation, six clouds in equilibrium, and two clouds in subsaturation. At the fifth track at 70.3° N (Figure 3.10e), there are 13 clouds in supersaturation, one cloud in equilibrium, and two clouds remain in subsaturation. The two subsaturated clouds at 70.3° N are later-season NLCs which were detected on August 18, 2005 and August 13, 2012. The temperatures of these two later-season subsaturated clouds are both between 150.7 K and 150.8 K at 70.3° N. A cooling of 4-5 K is necessary to bring the equilibrium water vapor level down to the MLS water vapor. Figure 3.11 displays a histogram of the number of clouds in each stability category at each track point. Cloud formation conditions improve as the track points progress further north; the cloud conditions move out of subsaturation conditions into equilibrium and supersaturated conditions.

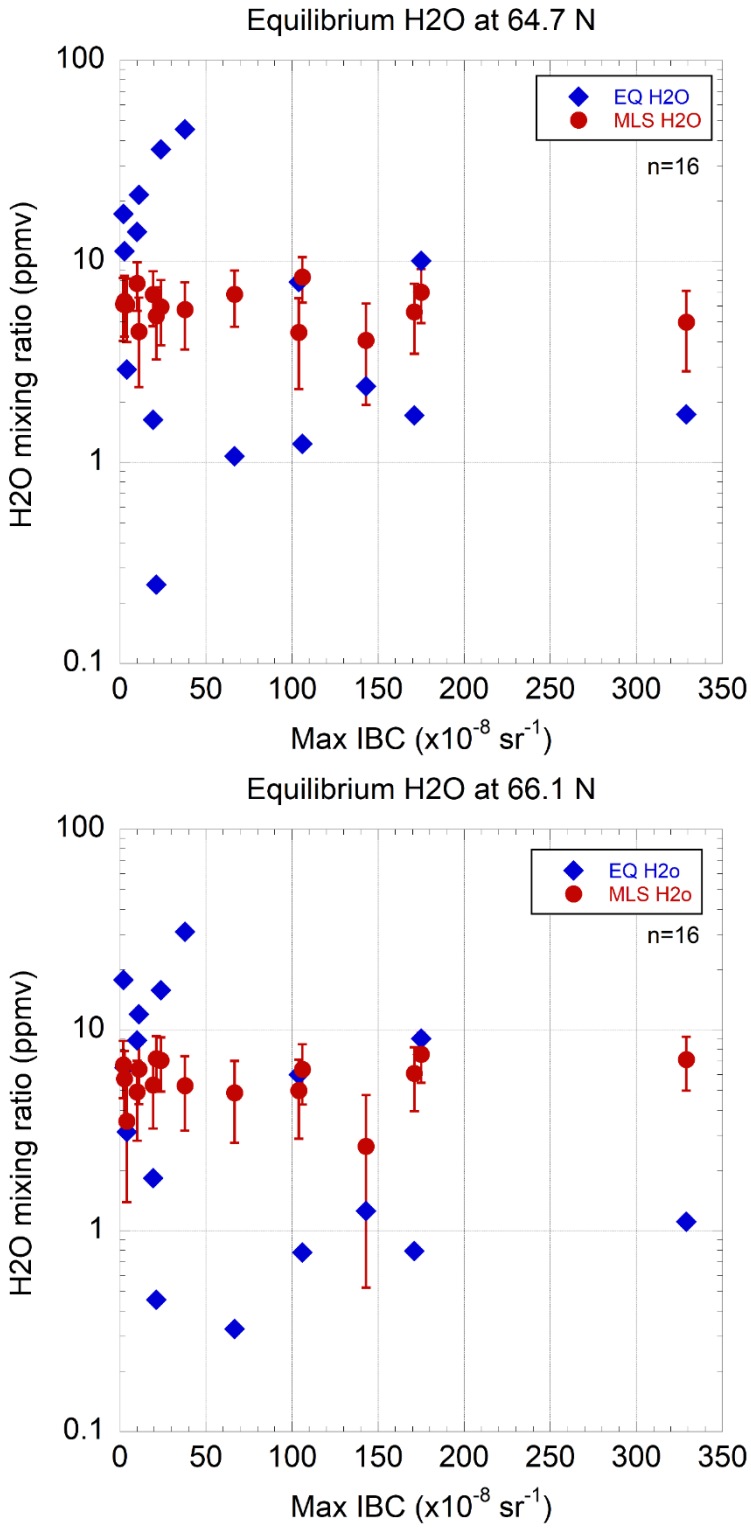

Figure 3.10a.(top) Maximum IBCs for 16 NLCs detected by lidar at Poker Flat and the equilibrium H2O and ambient H2O on each night measured by MLS data at 64.7° N. Figure 3.10b. (bottom) Maximum IBCs for 16 NLCs detected by lidar at Poker Flat and the equilibrium H2O and ambient H2O on each night measured by MLS data at 66.1° N.

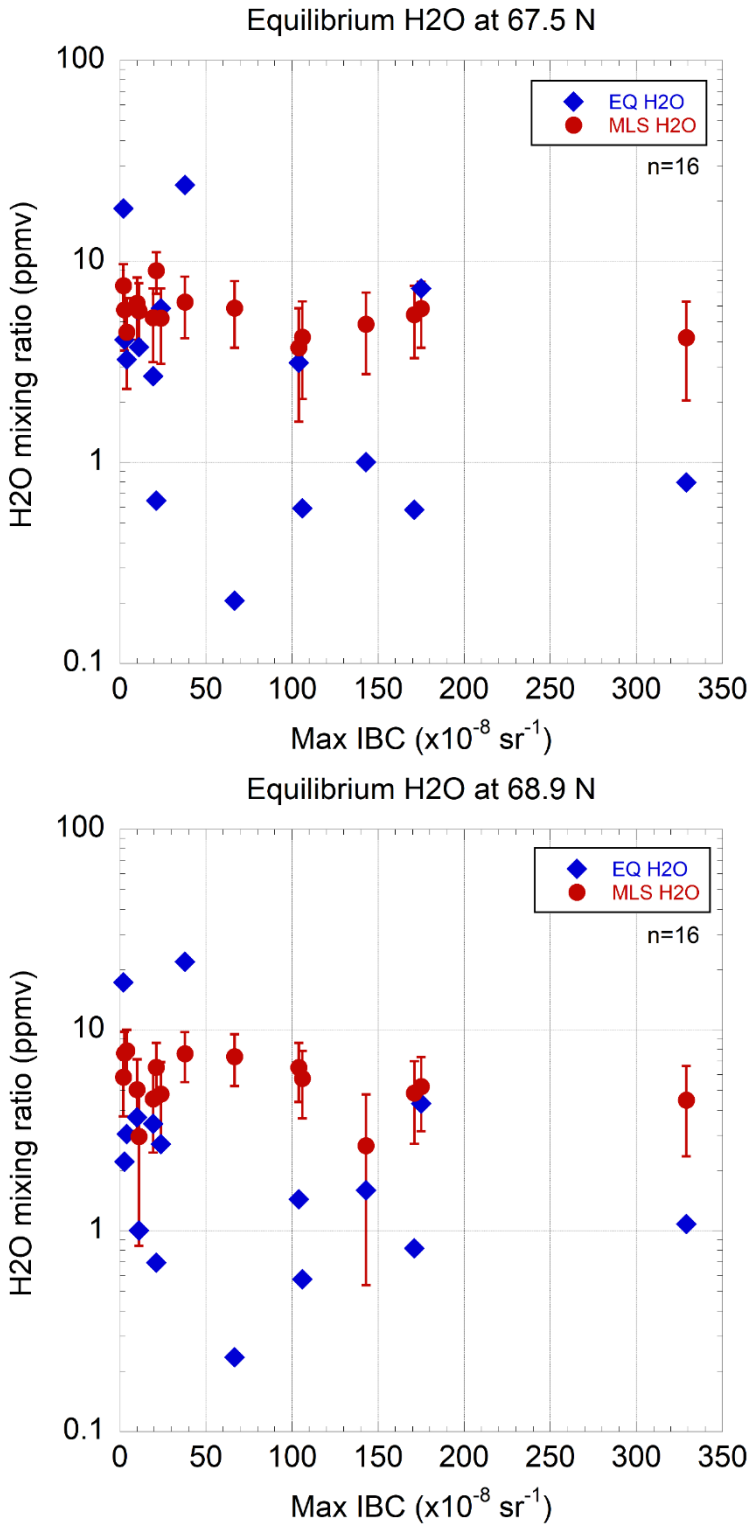

Figure 3.10c.(top) Maximum IBCs for 16 NLCs detected by lidar at Poker Flat and the equilibrium H2O and ambient H2O on each night measured by MLS data at 67.5° N. Figure 3.10d. (bottom) Maximum IBCs for 16 NLCs detected by lidar at Poker Flat and the equilibrium H2O and ambient H2O on each night measured by MLS data at 68.9° N.

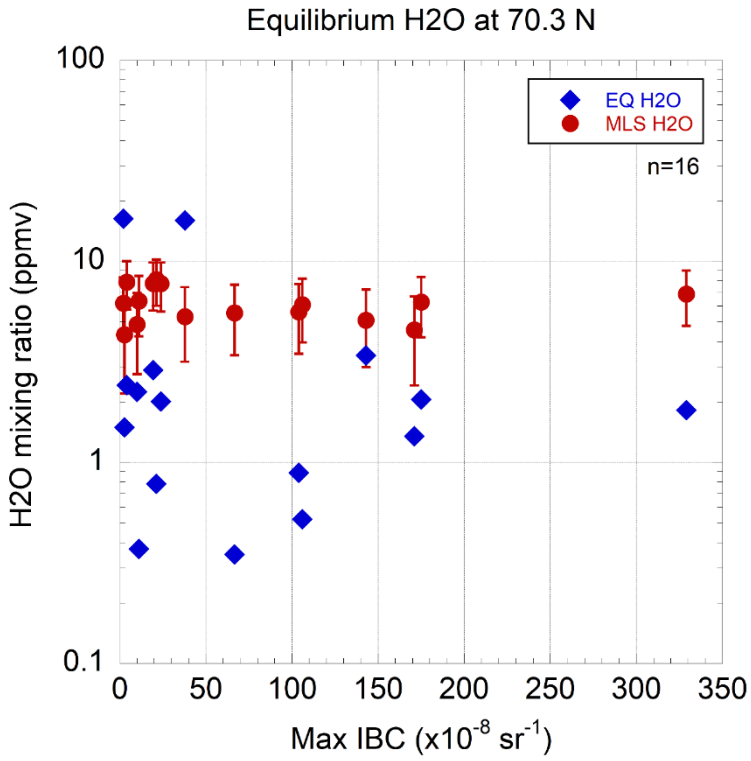

Figure 3.10e. Maximum IBCs for 16 NLCs detected by lidar at Poker Flat and the equilibrium H2O and ambient H2O on each night measured by MLS data at 70.3° N.

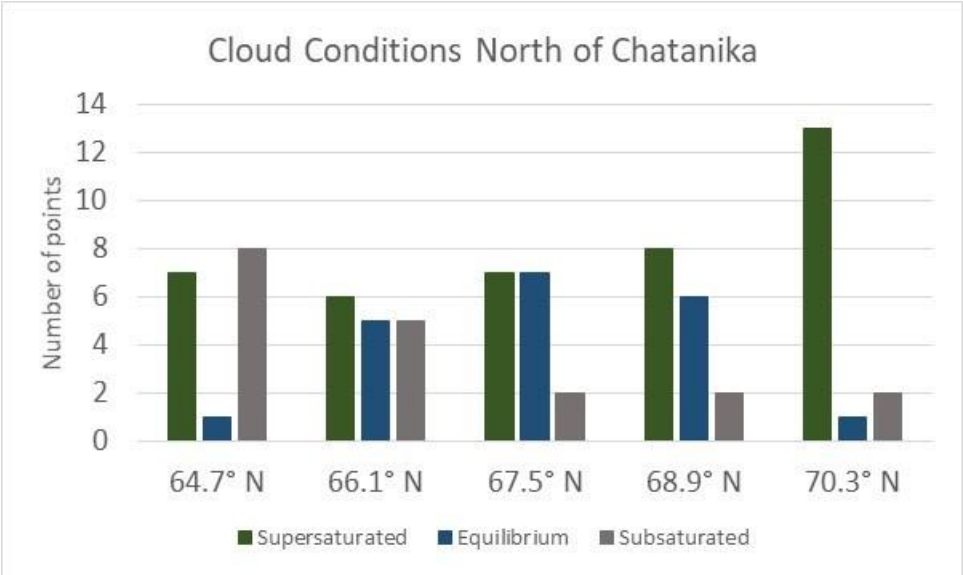

Figure 3.11. Histogram of cloud conditions along five latitudes over Alaska as determined by MLS temperature and water vapor data.

The water vapor equilibrium analysis provides a framework for understanding the NLCs observed by lidar at Chatanika. At 65° N, Chatanika lies south of the more concentrated cloud mass centered over the North Pole. In previous studies, it was assumed that the presence of NLCs overhead means that the temperature and water vapor concentrations are sufficient to keep a mesospheric ice cloud in equilibrium. However, it is now understood that NLCs to the north can be transported to the south through the southwestward wind, and that these clouds travel from a colder environment to a warmer environment. Particularly for the weaker NLCs observed at Chatanika, the lidar detections may represent unstable patches of cloud passing over Chatanika that are over several hundred kilometers away from their source locations, meaning that the clouds may have formed at least several hundred kilometers to the north. The results from this study reflect the findings from more complex investigations of NLC source locations. Three-dimensional modeling of NLC particle trajectories has been used to estimate nucleation sites for NLCs detected by lidar at the ALOMAR Observatory at Andoya (69° N) [Berger and von Zahn, 2007]. The nucleation sites for the NLC particles over Andoya were found to be up to 1000 km to the north, with the southern winds transporting the clouds towards the lidar observation site.

Chapter 4. Rayleigh Three-Channel Receiver

4.1. The Three-Channel Receiver

The Rayleigh Density Temperature Lidar (RDTL) system at the Lidar Research Laboratory (LRL) at Poker Flat Research Range (PFRR) in Chatanika, Alaska was upgraded in 2013 from a single-channel system to a two-channel system. From 1997 to 2013, the RDTL operated as a single-channel system that retrieved relative density and temperature profiles over the 40 km to 80 km altitude region [e.g., Thurairajah et al., 2009; Triplett et al., 2018]. With this single-channel system, two issues prevented quality measurements outside of the defined altitude range; the high signal below 40 km would result in an overload in the detector, and the low signal above 80 km had a low signal-to-noise ratio. The motivation of the upgrade in 2013 was to extend the altitude range of measurements by receiving signal lower in the stratosphere and higher in the mesosphere. It is possible to achieve measurements lower in the atmosphere by decreasing the power of each laser pulse or by decreasing the area of the telescope, but these methods would place a lower cap on the high altitude of quality measurements. Similarly, it is possible to achieve measurements at higher altitudes in the atmosphere by increasing the power of each laser pulse or by increasing the area of the telescope, but these methods would place a higher cap on the low altitude of quality measurements.

The strategy of a multi-channel system is to split the light received by the telescope between several channels, with each channel operating as an individual detector. A smaller portion of returned light is allowed into the detector of the low-altitude channel, and the remaining portion of returned light is directed to the detector(s) of the high-altitude channel(s). By this method, lidar measurements are possible at lower altitudes in the

atmosphere since less signal in the low-altitude channel eliminates the overloading of its detector. Lidar measurements are possible at higher altitudes in the atmosphere since greater signal is directed into the detector(s) of the high-altitude channel(s). Furthermore, the signals from the three channels can be combined and hence create a more statistically significant signal profile.

In 2013, the RDTL receiver system was upgraded to a two-channel system through the strategy described above, while the 60 cm telescope was replaced with a 1.04 m telescope. The upgrades resulted in a signal increase by a factor of 3.3, a measurement extension of 8 km in altitude, and a reduction in temperature retrieval errors by half [Triplett, 2016]. In 2017, the RDTL receiver system was further upgraded from a two-channel system to a three-channel system. A diagram of the RDTL three-channel receiver system is shown in Figure 4.1. The three-channel receiver system consists of a 1.04 m telescope, a pinhole (1 mrad or 0.5 mrad), a collimating lens, and three channels each consisting of a beam splitter (or mirror), an interference filter, a focusing lens, a photomultiplier tube (PMT), a high speed recorder, and a data acquisition computer. The high speed recorders are synchronized to the Nd:YAG laser by a laser pulse detector. In the RDTL three-channel receiver system, 20% of the light enters the low-altitude channel (Channel 1) and the remaining 80% of the light is split evenly between two high-altitude channels (Channel 2 and Channel 3). The PMT of each channel is electronically switched from a low gain mode to a high gain mode at a certain time after the laser fires to avoid overloading the detector with high signal from the low altitudes. For Channel 1, the delay time is chosen as 150 μs, corresponding to a switching altitude of 22.5 km. For Channel

2 and Channel 3, the delay time is chosen as 200 μs, corresponding to a switching altitude of 30 km.

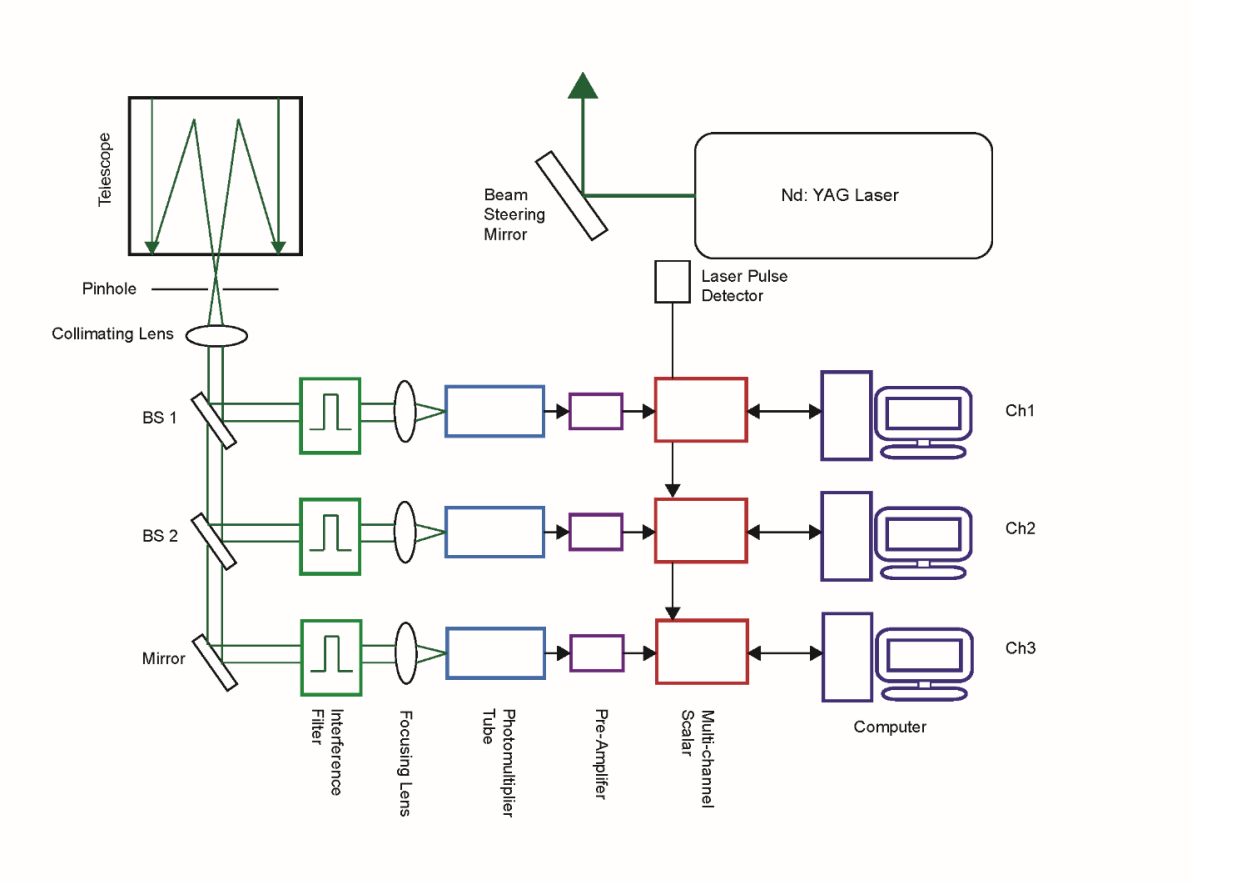

Figure 4.1. Schematic diagram of the three-channel receiver for the Rayleigh lidar system operating at 532 nm. The signal is distributed between the low-altitude channel (R1) and the two high-altitude channels (R2 and R3). BS 1 is a 20-80 beam splitter. BS 2 is a 50-50 beam splitter.

During observations with the RDTL system, data is acquired in profiles, with each profile consisting of signal from the integration of multiple (typically 1000) laser pulses. A number of profiles (typically 16) is acquired and stored in a single data file. The data acquisition program pauses in between sets of data to allow the operator to attend to the lidar system if required. The operator then initiates the next set of data. The raw resolution of the RDTL measurements is currently 50 seconds in time and 48 meters in altitude.

4.2. Signal Analysis

4.2.1. 22-23 December 2018 Observation

Figure 4.2 shows the total raw lidar signal in each of the 3 channels from the RDTL observations on the night of December 22-23, 2018. On this night, the RDTL operated from 17:39-06:59 LST (UT-9 h). The laser power was 7.8 W. The total number of sets acquired was 59, with Channel 1 acquiring 920 profiles (integration of 920,000 laser pulses), and Channel 2 and Channel 3 each acquiring 944 profiles (integration of 944,000 laser pulses). It is usual that Channel 1 acquires less profiles than the other channels due to periodic hang-ups in its data acquisition, requiring the operator to reconfigure the settings before continuing with the next profile. The total raw lidar signal profile in Figure 4.2 shows the exponential decrease of signal with height corresponding to atmospheric density diminishing with height. At the top altitudes (>90 km), the signal profile is dominated by noise. At these high, noisy altitudes, the signal due to atmospheric density is considered negligible and the total signal is due to the sum of the background skylight and the dark current inherent in the detector. The background skylight signal and the dark signal are expected to be constant with height.

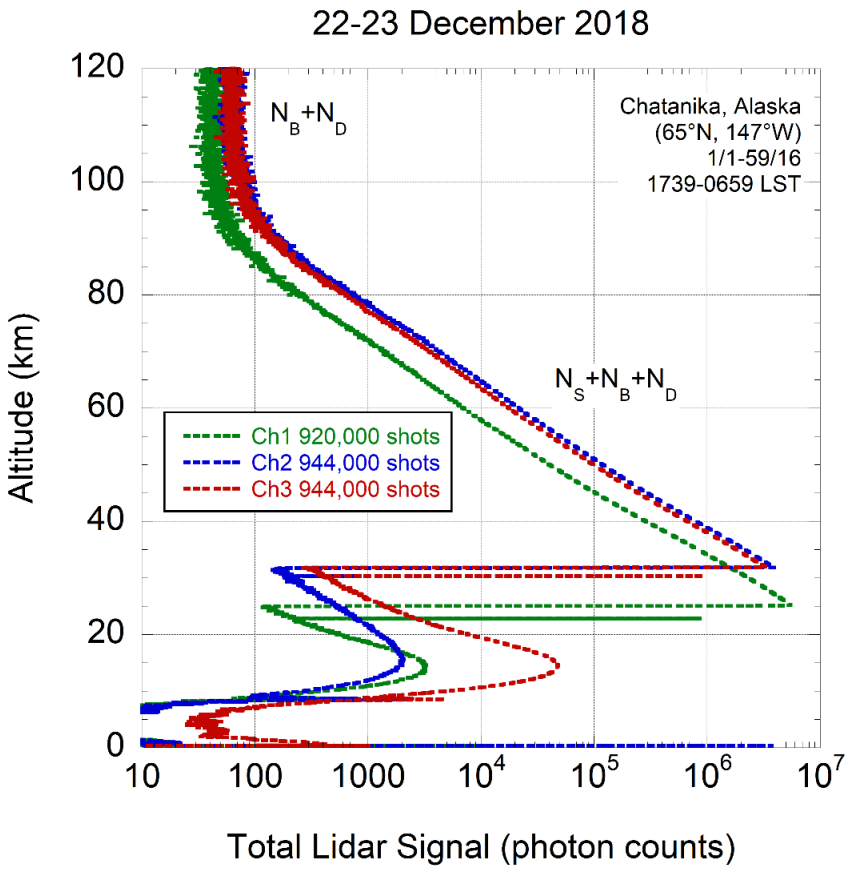

Figure 4.2. Integrated lidar signal from Channel 1 (green), Channel 2 (blue), and Channel 3 (red) of the Rayleigh lidar receiver during the lidar observation on 22-23 December 2018.

Table 4.1 provides a summary of the signal in each channel on the night of the lidar observation. For each channel, the total signal from 60-65 km (105 range bins) and the total signal from 120-125 km (105 range bins) is shown. The total signal from 60-65 km represents the sum of the lidar signal due to the atmosphere and the signal due to the background and dark current. The total signal from 120-125 km represents the sum of the background signal and dark signal. To isolate the atmospheric signal, the signal from 120-125 km (or another high-altitude region) is subtracted from the total lidar signal at 60-65 km. The remaining signal is normalized by the number of laser pulses to yield a 'signal per pulse' value for each channel. The signal per pulse value is used to determine the percent of signal contribution from each channel. The signal per pulse in Channel 1, Channel 2, and Channel 3 for the lidar observations on December 22-23, 2018 was 0.5 counts, 1.6 counts, and 1.4 counts respectively. The distribution of the signal percentage between Channel 1, Channel 2, and Channel 3 is 14%, 46%, and 40% respectively.

Table 4.1. Three-Channel RDTL Signal on 22-23 December 2018

Time: 1739-0659 LST Sets/profiles: 1/1-59/16	Channel 1	Channel 2	Channel 3
Laser pulses	920,000	944,000	944,000
Total signal (60-65 km)	506,054	1,559,151	1,285,612
Total signal (120-125 km)	4,426	6,832	6,744
Signal (60-65 km)	501,628	1,552,319	1,278,868
Signal per pulse (60-65 km)	0.5	1.6	1.4
Percent of signal (60-65 km)	14%	46%	40%
Estimated dark signal (120-125 km)[1]	1300	530	1600

[1]Dark signal measured on October 11, 2019.

4.2.2. Dark Signal

In the fall of 2019, tests were conducted to measure the dark signal in the photomultiplier tubes of each of the three channels. The dark signal was measured on September 27, 2019 and October 11, 2019 with the interference filters off and the lights off in the receiver room. On each day, measurements were taken both with and without the electronic blanking on. The mean total signal, the standard deviation, and the standard error for the dark signal in each channel between 40-180 km are shown in Table 4.2a and Table 4.2b for the dark signal tests from September 27, 2019 and October 11, 2019. The total dark signal from 40-180 km for each set of data taken during the tests is shown in Figure 4.3a and Figure 4.3b. The difference between the dark signals with the electronic blanking on and off were found to not be statistically significant. The dark signal rate varied between 8-55 counts per second (cps) between the three channels considering measurements taken on both days. The expected dark signal rate for the PMT is 50-150 cps. Given the discriminator level of -0.2 V set for each of the detectors, the measured dark signal rate of 8-55 cps is reasonable. The dark signal rate in each channel on the October day was about twice as high than the measurements on the September day. The increase in dark signal is likely attributed to the higher room temperature on the second day when the heating system was running in the building. An increase in dark signal rate of this magnitude is expected for a room temperature increase of 10° C [Hamamatsu, 2007]. The increase in temperature results in higher thermionic emissions in the PMT, yielding higher dark signal on the October day. The estimated dark signals from 120-125 km in Table 4.1 are derived from the measurements taken on October 11, 2019 with the electronic blanking on, where the dark signal rates were 43

cps, 17 cps, and 50 cps in Channel 1, Channel 2, and Channel 3 respectively. The background signal from 120-125 km is dominated by skylight over the dark signal, especially at the beginning and the end of the observational period when twilight occurs.

Table 4.2a. Dark Signal on 27 September 2019

Channel/blanking	Set Numbers	Mean Signal (counts)	Standard Deviation	Standard error
R1 Unblanked	3-10	226	13	5
R2 Unblanked	3-10	126	12	4
R3 Unblanked	3-10	381	50	18
R1 Blanked	11-13	225	19	11
R2 Blanked	11-13	152	23	13
R3 Blanked	11-13	333	22	12

Table 4.2b. Dark Signal on 11 October 2019

Channel/blanking	Set Numbers	Mean Signal (counts)	Standard Deviation	Standard error
R1 Unblanked	1-9	649	36	12
R2 Unblanked	1-9	235	28	9
R3 Unblanked	1-9	814	53	18
R1 Blanked	10-18	636	34	11
R2 Blanked	10-18	254	17	6
R3 Blanked	10-18	743	51	17

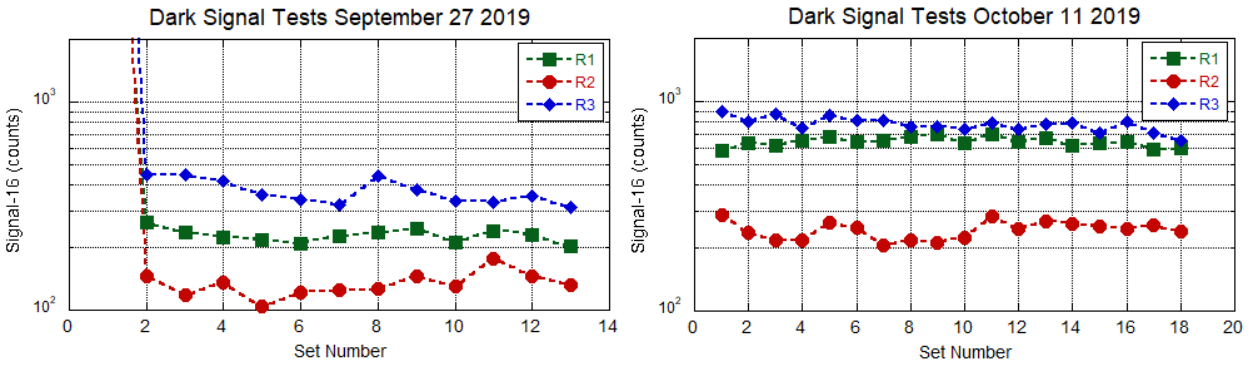

Figure 4.3a. (left) Total dark signal from 40-180 km for each test data set on 27 September 2019.
Figure 4.3b. (right) Total dark signal from 40-180 km for each test data set on 11 October 2019.

4.2.3. 11-12 August 2019 Observation

The RDTL three-channel receiver system was used to conduct measurements during a noctilucent cloud (NLC) campaign at PFRR in the summer of 2019. Figure 4.4 shows the total raw lidar signal in each of the 3 channels from the RDTL observations on the night of August 11-12, 2019. On this night, the RDTL operated from 22:35-03:30 LST. The laser power was 10 W. The total number of sets acquired was 22. For NLC observations, the data is typically processed to include only the darkest part of the night and/or to focus on the core part of the night when the NLCs were detected. The total raw lidar signal shown in Figure 4.4 represents the integrated signal from set 4, profile 1 through set 22, profile 8 in each channel. The signal in Channel 1 represents the integration of signal from 288 profiles (288,000 laser pulses). The signals in Channel 2 and Channel 3 each represent the integration of signal from 296 profiles (296,000 laser pulses). The raw signal profile in Figure 4.4 shows the exponential decrease of signal with height corresponding to atmospheric density diminishing with height until about 80 km. The NLC echo is visible in all three channels from about 80-84 km and represents the added signal contribution from the presence of NLC (ice crystals).

Table 4.3 provides a summary of the signal in each channel on the night of the NLC observation on August 11-12, 2019. The total signal values displayed are determined in the same manner as those shown in Table 4.1. The distribution of the signal percentage based on the signal per pulse at 60-65 km between Channel 1, Channel 2, and Channel 3 is 16%, 40%, and 44% respectively. Based on the splitting of light between the three channels, the expected signal distribution between Channel 1, Channel 2, and Channel 3 is 20%, 40%, and 40% respectively. The signal distributions on the December

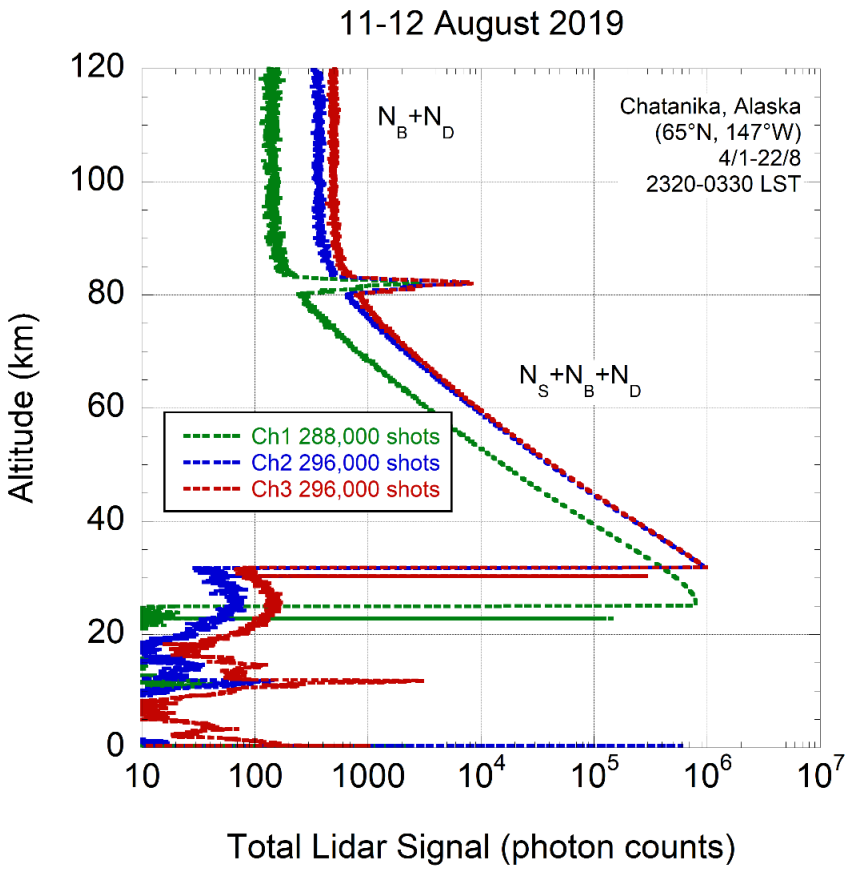

Figure 4.4. Integrated lidar signal from channel 1 (green), channel 2 (blue), and channel 3 (red) of the Rayleigh lidar receiver channels during a noctilucent cloud detection on 11-12 August 2019.

Table 4.3. Three-Channel RDTL Signal on 11-12 August 2019

Time: 2320-0330 LST Sets/profiles: 4/1-22/8	Channel 1	Channel 2	Channel 3
Laser pulses	288,000	296,000	296,000
Total signal (60-65 km)	252,219	649,980	710,164
Total signal (120-125 km)	15,105	38,218	52,738
Signal (60-65 km)	237,114	611,762	657,426
Signal per pulse (60-65 km)	0.8	2.1	2.2
Percent of signal (60-65 km)	16%	40%	44%
Total signal (80-85 km)	72,570	189,106	217,700
Signal (80-85 km)	57,465	150,888	164,962
Signal per pulse (80-85 km)	0.2	0.5	0.6
Percent of signal (80-85 km)	16%	40%	44%
R_{max}	160	146	162
Altitude (km) of R_{max}	82.37	82.32	82.32
Lidar signal at R_{max}	230	509	570

22-23, 2018 observation and the August 11-12, 2019 observation both deviate from the expected signal distribution. Also, the signal distributions between these two nights of observations are slightly different. From observations during the winter of 2018-2019, it was discovered that the ratio between signals in the three channels is sensitive to the position of the interference filters. The position of the interference filter affects the transmission of the filter and causes slight variations in the signal ratios from night to night. The signal per pulse and signal distribution for the 80-85 km range are also provided in Table 4.3. The signal per pulse in each channel from 80-85 km is about a factor of 4 times less than the signal per pulse from the 60-65 km range from the same night.

The presence of NLCs on the night of August 11-12, 2019 provides a detection target that can also be used to analyze the signals in the three-channel receiver system. Table 4.3 compares values of the maximum backscatter ratio (R_{max}) between the three channels. The R_{max} is determined based on the 6000 laser-pulse-integration method described previously in Chapter 2 with the Rayleigh scatter signal estimated from a third-order polynomial fit over the summed signal from 60-90 km, excluding the cloud altitude region (80-85 km). The 6000 laser-pulse-integration yields 48 profiles in Channel 1 and 49 profiles each in Channel 2 and Channel 3. The R_{max} occurs in profile 31 in each channel. The R_{max} is 160, 146, and 162 and occurs at 26:03 LST, 25:59 LST, and 25:59 LST in Channel 1, Channel 2, and Channel 3 respectively. The time in Channel 1 is slightly offset from the other two channels due to the slightly smaller number of raw profiles acquired in Channel 1's acquisition. The altitude of the maximum R is 82.37 km, 82.32 km, and 82.32 km in Channel 1, Channel 2, and Channel 3 respectively. The altitude of R_{max} in Channel 1 is one altitude range bin above the altitudes of maximum R in the other two channels. The lidar signal in each channel at the time and altitude of R_{max} is also displayed in Table 4.3. The R_{max} statistical error is less than 5% in each of the channels. This means that the R_{max} values in Channel 1 and Channel 3 are within the statistical errors of each other. The R_{max} value in Channel 2 is outside the statistical error with both Channel 1 and Channel 3.

The Rayleigh scatter estimate fitting for each of the three channels is shown in Figure 4.5. The summed signal over the night is shown as the top white profile in each panel. The blue line shows the Rayleigh scatter signal that has been estimated by a third-order polynomial fit over the summed signal from 60-90 km, excluding the cloud signal

region (80-85 km). The lower white profile in each panel shows the lidar signal in profile 31 in each channel and the corresponding scaled Rayleigh estimated signal in green. Figure 4.6 shows false color plots of R with time and altitude for the NLC detected on August 11-12, 2019 by each channel. All three channels show the same NLC structure.

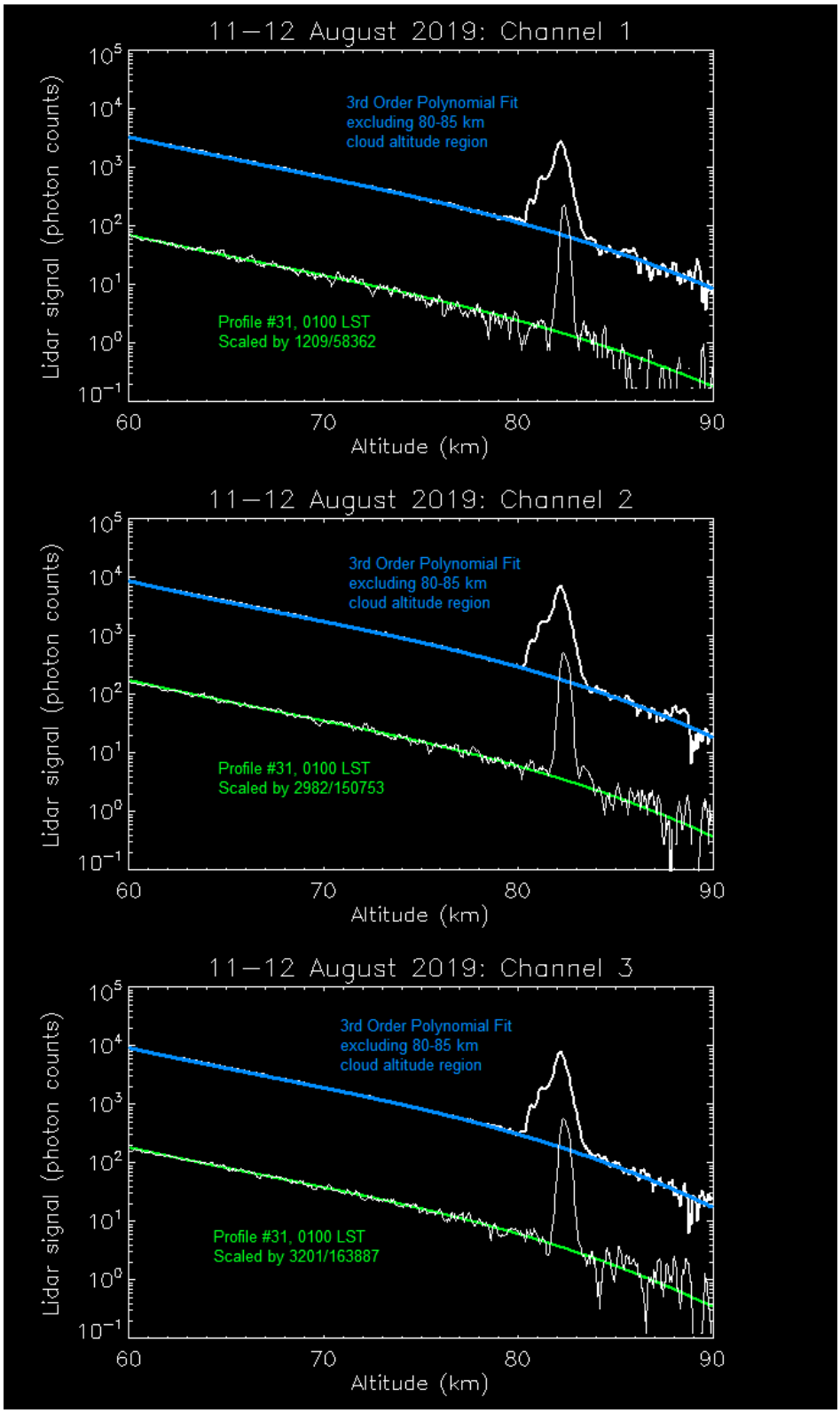

Figure 4.5. Lidar signal from 60-90 km in each Rayleigh receiver channel during NLC observations on 11-12 August 2019. The thick white profile shows the total lidar signal in each channel. The blue line shows the estimated Rayleigh scatter signal. The thin white profile shows the lidar signal of a single 6000-pulse integrated profile at 0100 LST. The green line shows the scaled Rayleigh scatter estimate for the profile.

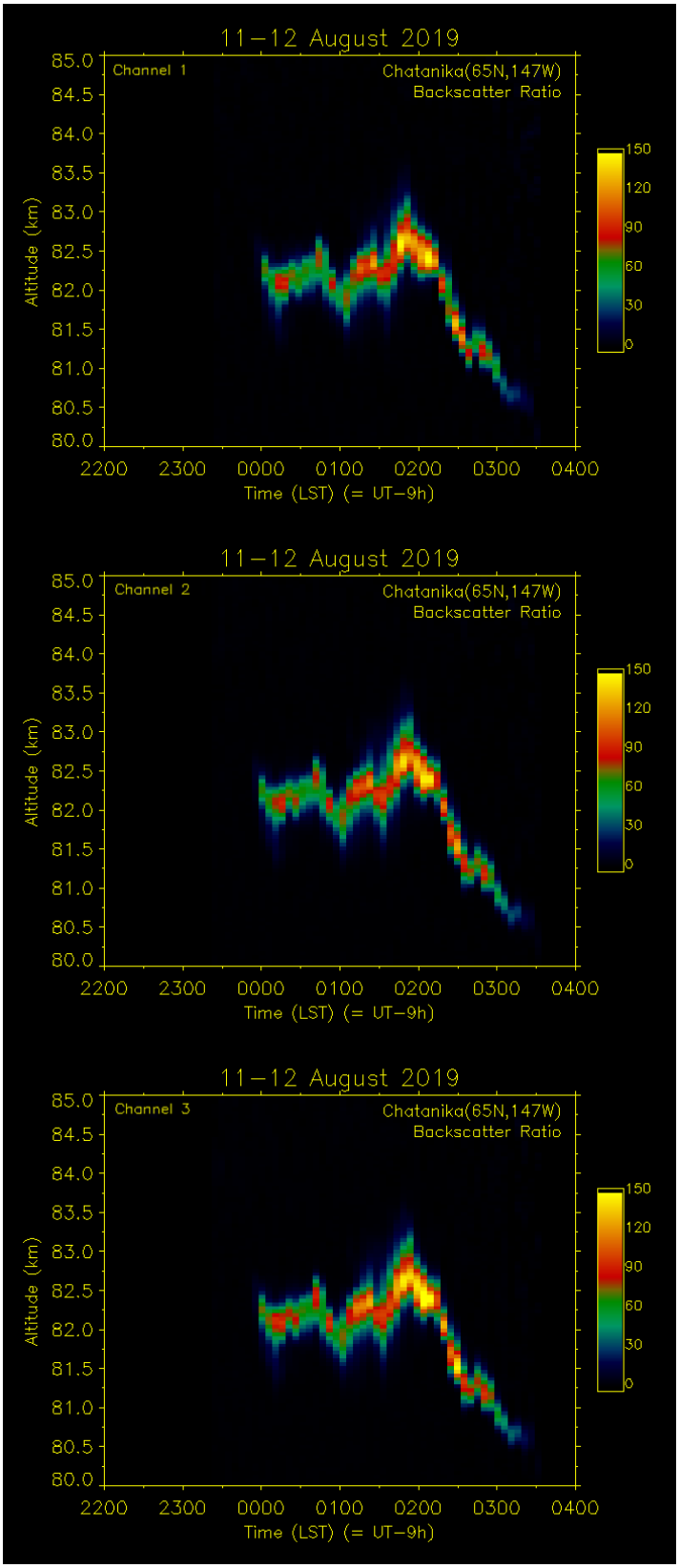

Figure 4.6. False color plots of backscatter ratio in each Rayleigh receiver channel for the noctilucent cloud observed on 11-12 August 2019.

4.3. Density and Temperature Retrievals

4.3.1. Temperature Retrieval from Relative Density

As introduced in Chapter 2, the RDTL system makes direct measurements of backscattered photons, and the total lidar signal at a certain altitude, z, is a sum of the signal due to the atmospheric density, N_s, the signal due to the background starlight, N_B, and the signal due to the dark current, N_D,

$$N(z) = N_S(z) + N_B + N_D \tag{4.1}$$

After the signal due to the background, N_B, and the signal due to the dark current, N_D, has been subtracted from the total signal, the remaining signal is the lidar signal proportional to atmospheric density, N_s. The lidar signal profiles are smoothed in altitude (typically over 2 km) and binned in time, and then used to calculate relative density profiles. The lidar signal is normalized at a bottom altitude (~30 km) to yield a relative density profile with height,

$$\frac{\rho(z_1)}{\rho(z_2)} = \frac{N_s(z_1)}{N_s(z_2)}\left(\frac{z_1}{z_2}\right)^2 \tag{4.2}$$

where ρ is atmospheric density (mol m^{-3}). The relative density equation highlights one of the greatest strengths of the lidar technique; the relative density measurement is independent of the laser system parameters, such as the laser power, and sky conditions, such as the transmission of the atmosphere.

The temperature profile is calculated from the relative density profile by assuming hydrostatic equilibrium (Equation 4.3) and that the ideal gas law (Equation 4.4) reasonably demonstrates the behavior of the atmosphere. The approximations are as follows,

$$\frac{\partial p}{\partial z} = -\rho(z)g(z) \tag{4.3}$$

$$p = \frac{\rho RT}{M} \tag{4.4}$$

where g is gravitational acceleration (9.8828 m s^{-2} at LRL [Thurairajah, 2009], p is the atmospheric pressure, ρ is the atmospheric density (mol m^{-3}), R is the ideal gas constant (8.3145 J K^{-1} mol^{-1}), T is the temperature (K), and M is the mean molecular weight of dry air (2.8964 x 10^{-2} kg mol^{-1}).

A temperature profile, $T(z)$, is then retrieved from the relative density profile by assuming hydrostatic equilibrium and integrating downward through the profile from an assumed temperature at the top altitude, z_0, of the profile,

$$T(z) = \frac{\rho(z_0)}{\rho(z)} T(z_0) + \frac{M}{R} \int_z^{z_0} \frac{\rho(r)}{\rho(z)}\, g(r) dr \tag{4.5}$$

where $T(z_0)$ is the initial assumed temperature. As the integration progresses further down in altitude, the first term in the temperature equation decreases, and any bias in temperature at a given altitude associated with the error in the initial assumed temperature diminishes.

4.3.2. Combining Low and High Channel Data

Previously, a composite temperature retrieval of the RDTL low-altitude and high-altitude channels was performed based on matching the vertical gradient in the relative densities between the low-altitude and high-altitude profiles. The lidar signal profiles of each channel were smoothed by 2 km and binned in time. Then the relative density and temperature profiles were retrieved for each channel individually. The relative density and temperature profiles of the low-altitude channel and the high-altitude channel were then combined at the altitude of where the vertical gradients in the relative densities were

closest, yielding a single relative density profile and a single temperature profile [Triplett, 2016]. This method resulted in a discontinuity at the combination altitude. Figure 4.7a shows an example of a discontinuity in the temperature profile retrieved by the density gradient combination method with RDTL data taken on December 22-23, 2018. The high-altitude temperature profile was seeded by a Sodium Resonance Wind Temperature Lidar (SRWTL) temperature measurement at 85 km [Li, 2019]. The low-altitude temperature profile was seeded by the high-altitude RDTL temperature profile at 70 km. The low-altitude and high-altitude temperature profiles were then combined at 66.0 km, and a discontinuity is evident in the composite temperature profile at this altitude.

A new retrieval method was established in the spring of 2019 to process the 26 nights of RDTL data taken with the three-channel receiver system during the winter of 2018-2019. The combination altitude in this method is defined as the altitude where the vertical gradient in the ratio of the lidar signals between the channels is closest to zero. First, the lidar signals from Channel 1, Channel 2, and Channel 3 are summed to create a high-altitude signal profile. The low-altitude signal profile is composed of the lidar signal from Channel 1 alone. The ratio of the high-altitude signal to the low-altitude signal is calculated. The altitude where the derivative in the lidar signal ratio is closest to zero is chosen as the combination altitude. The lidar signal in the low-altitude profile is scaled up to the lidar signal in the high-altitude profile, and the two lidar signal profiles are joined at the combination altitude. The composite lidar signal profile is then smoothed by 2 km. A relative density profile between ~30-85 km is then produced from the composite lidar signal profile. Finally, a temperature profile is produced by seeding the top altitude of the relative density profile with the SRWTL temperature. Figure 4.7b shows the temperature

profile produced with the signal combination method for the RDTL data taken with the three-channel receiver system on December 22-23, 2018. The low-altitude and high-altitude signal profiles are combined at 63.5 km.

The signal combination method produces a much smoother transition at the combination altitude and eliminates the discontinuity present in the previous combination method of density gradient agreement. The smoother transition over the combination altitude is aided by the 2 km signal smoothing that is performed after the low-altitude signal profile and the high-altitude signal profile have been combined. In the density gradient combination method, the 2 km signal smoothing was performed in the low-altitude signal profile and the high-altitude signal profile before the two temperature profiles were combined.

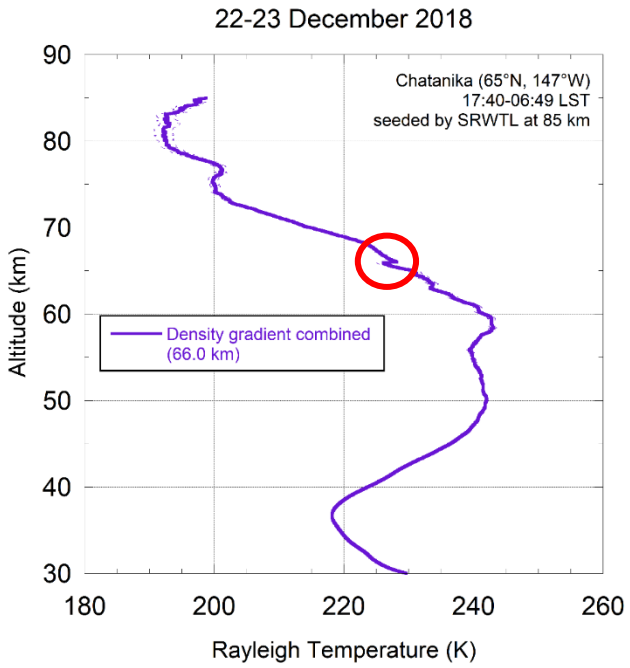

Figure 4.7a. Average Rayleigh temperature profile from three-channel observations on 22-23 December 2018. The Rayleigh temperature is retrieved by the density gradient agreement method of combining high-altitude and low-altitude channel data. A discontinuity is seen at the combination altitude of 66.0 km.

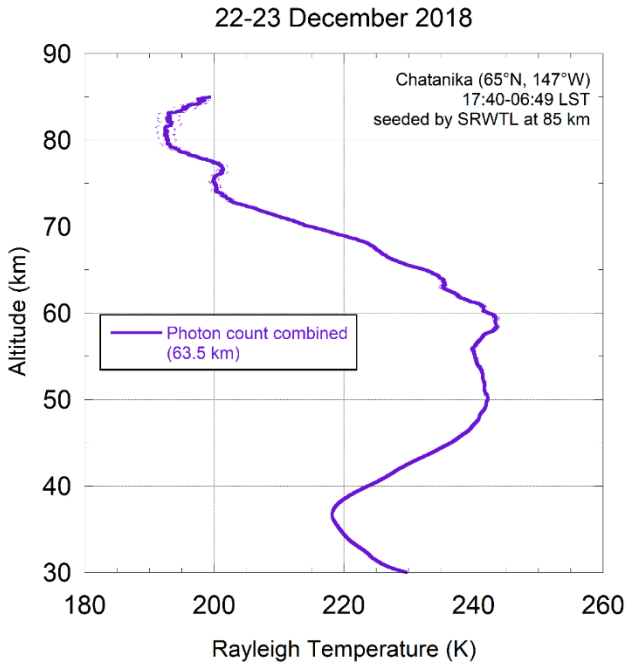

Figure 4.7b. Average Rayleigh temperature profile from three-channel observations on 22-23 December 2018. The Rayleigh temperature is retrieved by the signal ratio method of combining high-altitude and low-altitude channel data. The method results in a smooth profile over the combination altitude of 63.5 km.

4.3.3. Simultaneous RDTL and SRWTL Measurements

Previously, the assumed initial temperatures at the top of the profile were adopted from climatological models such as the Stratospheric Processes And their Role in Climate (SPARC) model [SPARC, 2002; Randel et al. 2004] and the MSIS model [MSIS, 2019], or direct measurements from rocket investigations at PFRR [Triplett et al., 2018]. In the fall of 2017, a sodium resonance wind temperature lidar (SRWTL) was deployed at PFRR. The SRWTL makes spectroscopic measurements of temperature in the sodium layer (~80-100 km) derived from the Doppler broadening of the sodium absorption spectrum [Li, 2019]. Besides extending the scope of science conducted at the lidar lab at PFRR, the SRWTL provides coincident temperature measurements to be used as the top altitude initial temperature for the RDTL data and avoids the use of assumed temperatures from climatological models.

Different seeding altitudes are compared to determine the seeding altitude that results in the best agreement between the RDTL temperature profile and the SRWTL temperature profile. Ideally, the RDTL temperature profile is extended as high as possible while maintaining good agreement with SRWTL temperatures within the altitude range of quality measurements. The RDTL temperature profiles at seeding altitudes of 85 km, 90 km, and 95 km are shown in Figure 4.8a-c along with the SRWTL temperature profile. The SRWTL temperature profile extends from 80 km to 112 km, but the bottom and top of the SRWTL profile is noisy due to the low resonance signal from the bottom and top edges of the sodium layer. The RDTL temperature profile seeded with the SRWTL temperature at 85 km shows the best agreement with the SRWTL temperature profile below the seeding altitude. As the seeding altitude increases to 90 km and 95 km, the

agreement between the RDTL temperature and the SRWTL temperature progressively diminishes. However, the difference in temperature between the SRWTL and RDTL profile seeded at 90 km is less than 5 K and is within the statistical error in temperature. Seeding altitude comparisons were also examined for 2-hour, 1-hour, and 15-minute integrated temperature retrievals and the most consistent seeding altitudes for these integrations are 83 km, 83 km, and 80 km respectively.

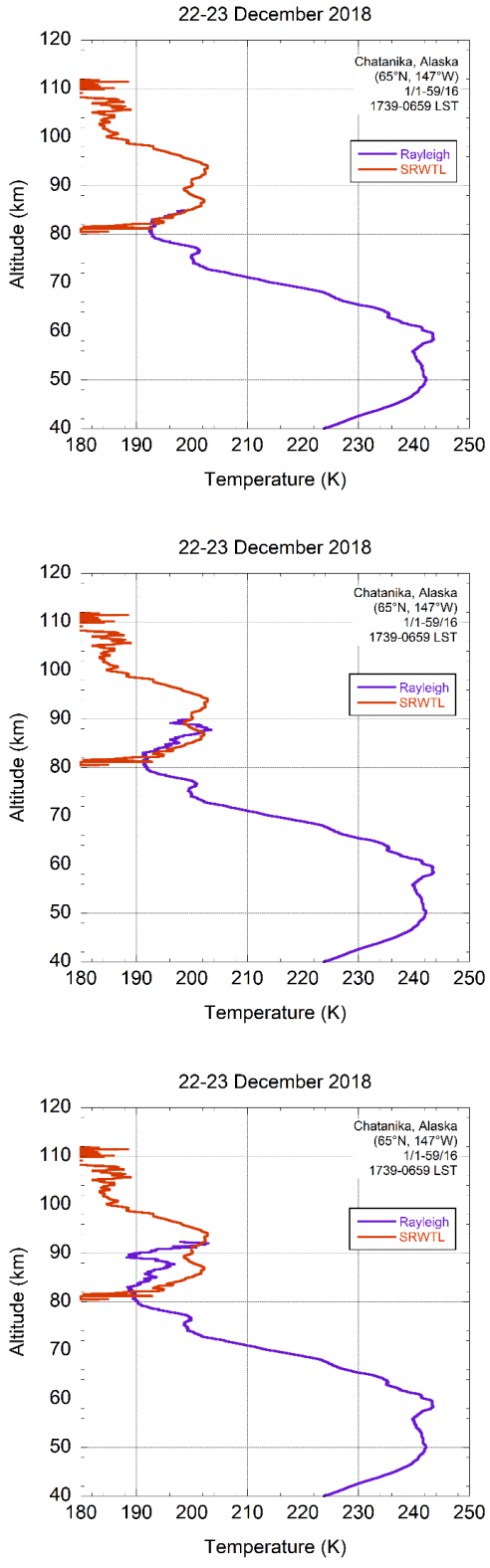

Figure 4.8a (top), 4.8b (middle), 4.8c (bottom). Average Rayleigh temperature profile from three-channel observations on 22-23 December 2018 seeded with the Sodium Resonance Wind Temperature Lidar temperature at 85 km (4.8a), 90 km (4.8b), and 95 km (4.8c).

The SRWTL temperatures from the sodium layer also make it possible to extend the RDTL relative density profile while assuming hydrostatic equilibrium. Given the RDTL relative density value at the bottom altitude, z_0, of the SRWTL temperature profile (~80 km), the relative density profile is extending upwards by integrating upward in height through the SRWTL profile and converting temperature to relative density. The relative density profile, $\rho(z)$, is determined by,

$$\rho(z) = \frac{T(z_0)}{T(z)}\,\rho(z_0)\exp\left(-\frac{M}{R}\int_{z_0}^{z}\frac{g(r)dr}{RT(r)}\right) \tag{4.3}$$

where $\rho(z_0)$ is the initial RDTL relative density at the top of the RDTL relative density profile and $T(z_0)$ is the initial SRWTL temperature at the bottom of the SRWTL temperature profile.

At the end of this process, a relative density profile from ~30 km to 120 km has been produced. The relative density profile is used to calculate absolute atmospheric density by initializing the bottom relative density value with an absolute density measurement from radiosonde data from the appropriate weather balloon launch which occurs every 12 hours at the Fairbanks airport [UWYO, 2018]. The radiosonde data provides absolute atmospheric density measurements up to an altitude typically between 25-35 km. The extended relative density profile is normalized to the top density value of the radiosonde data. In cases where the radiosonde measurement does not reach the bottom altitude of the lidar relative density profile, the radiosonde density is extrapolated upwards to 30 km. The result of the process described here is an absolute atmospheric density profile extending from ~30 km to over 100 km. Figure 4.9 shows the atmospheric density profile retrieved from RDTL and SRWTL data taken on December 22-23, 2018.

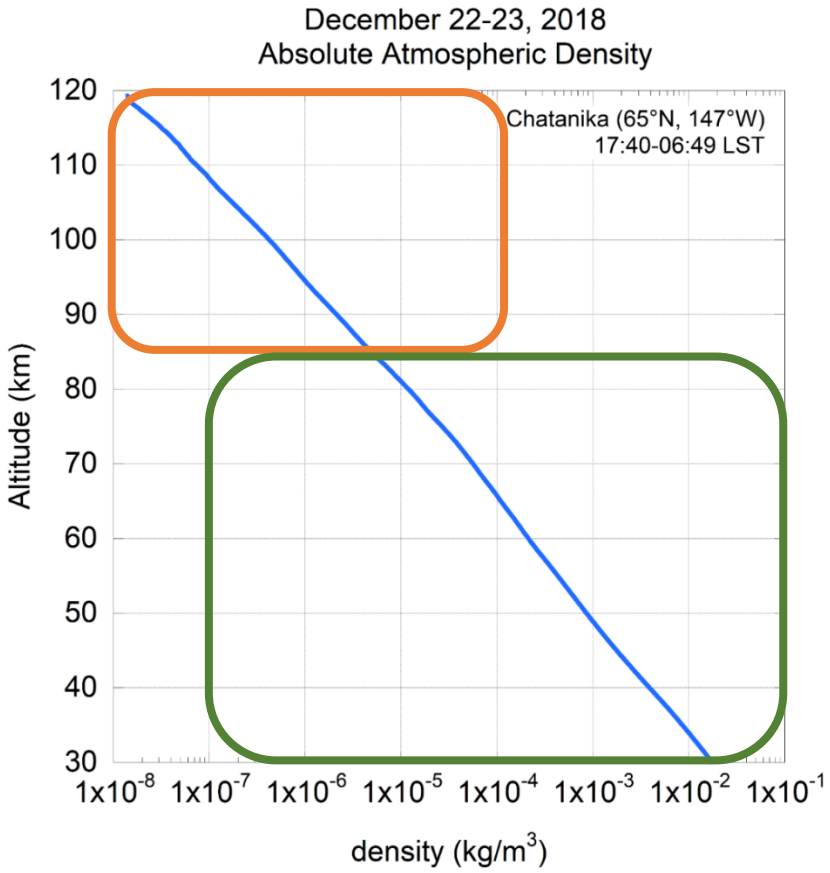

Figure 4.9. Average absolute density profile retrieved from Rayleigh lidar and Sodium resonance wind temperature lidar (SRWTL) observations on 22-23 December 2018. The absolute density profile was retrieved by seeding the lidar relative density profile with a radiosonde absolute density measurement at 30 km. The green outline shows the altitude range of the Rayleigh measurements and the orange outline shows the altitude range of the SRWTL measurements.

4.4 Summary and Conclusions

The RDTL system was upgraded to a three-channel receiver system in the summer of 2017. The receiver system is composed of one low-altitude channel and two high-altitude channels. RDTL data from observations on the night of December 22-23, 2018 and on the night of August 11-12, 2018 have been used to analyze the signal in each channel. Noctilucent cloud signal from the latter night is used to examine the difference in retrieved backscatter ratio values between the three channels. Data retrieval methods were developed to combine the lidar signal from the low-altitude and the high-altitude channels based upon the ratio of lidar signals between the two profiles. The deployment and operation of the SRWTL system since the fall of 2017 has enabled the seeding of the RDTL temperatures with a spectroscopic temperature measurement provided by the SRWTL system. The SRWTL temperatures are used to extend the RDTL relative density profile through the sodium layer (~80-120 km) assuming hydrostatic equilibrium. Using radiosonde data to normalize the relative density profile, absolute atmospheric density profiles from ~30 km to ~120 km can be obtained.

Chapter 5. Summary and Conclusions

In this thesis, I have presented a study focused on the noctilucent clouds (NLCs) that have been observed by Rayleigh lidar at the Lidar Research Laboratory (LRL) at Poker Flat Research Range (PFRR) in Chatanika, Alaska (65° N, 147° W). The studies include i.) a characterization of all NLCs observed by Rayleigh lidar at PFRR since 1997; ii.) a comparison of the lidar measurements with data from the Cloud Imaging and Particle Size (CIPS) instrument; iii.) an analysis of the meteorological conditions during the NLC lidar observations at Chatanika using microwave limb sounder (MLS) data; and iv.) a technical overview of the Rayleigh lidar three-channel receiver system at PFRR. The key conclusions from each study are summarized below.

i.) Characterization of NLCs at Chatanika

I have identified and characterized NLCs on 41 nights of high quality RDTL observations in NLC season in terms of their cloud duration, backscatter ratio (R), backscatter coefficient (BC), and integrated backscatter coefficient (IBC). The high quality observations have durations of at least 2.3 hours and an average signal per pulse of at least 0.3 counts through the night. Of the 41 high quality lidar observations, 21 observations include NLC detections and are considered significant under the condition that their IBC is greater than 3 times the error in their IBC. There are 20 nights with no NLCs detected. The frequency of occurrence of NLCs over Chatanika from a nightly perspective is 51%. In addition, there are a few nights where NLCs were not detected by the lidar but were visible to the north by ground observers at PFRR. The characteristics of NLCs at Chatanika have been reported in this thesis. The average cloud duration of

NLCs measured by lidar at PFRR is 99 minutes. The average maximum IBC is 8.10×10^{-7} sr^{-1}. The average maximum BC is 1.42×10^{-9} m^{-1} sr^{-1} and maximum BCs occur at an average altitude of 82.1 km. There is evidence that the brighter clouds occur at lower altitudes, indicating a growth-sedimentation mechanism where the ice crystals accumulate water content upon descent due to gravity. Also, there is some evidence that the brighter NLCs are also longer-lived clouds.

ii.) Comparison with CIPS

I used cloud detection and albedo data from the CIPS instrument to report the frequency of occurrence and brightness of NLCs over Alaska (60-70° N, 130-170° W) on the 48 hours around each lidar observation during NLC season (+/- 24 hours from local midnight). I also used the CIPS data to look at the frequency of occurrence and brightness of NLCs over Alaska across each NLC season where CIPS data was available and lidar observations were taken that summer. CIPS detects NLCs beginning in May and until the end of August. Each night of CIPS data was binned by 24 hours (+/- 12 hours from local midnight). The seasonality shows the frequency of occurrence increasing up to solstice and decreasing after solstice. In general, the positive NLC detections in the lidar data correspond to high values of frequency and brightness in the CIPS data, and the negative NLC detections in the lidar data correspond to near-zero values in frequency and brightness in the CIPS data. The CIPS data enables us to understand the lidar observations in the broader context of NLC activity over Alaska.

iii.) Environmental Analysis with MLS

I used MLS temperature and water vapor data to characterize the mesospheric environment during the NLC season lidar observations. The distribution between positive and negative NLC detections in the lidar data is most distinct in terms of corresponding frost point depression. At high temperatures relative to the frost point (>8 K above), there are no NLCs detected by lidar. At low temperatures relative to the frost point (>4 K below), there are always NLCs detected. There is a regime right above and below the frost point where we see both presence and absence of NLCs in the lidar data. When it comes to the impact of frost point depression on NLC brightness, there does not appear to be a strong relation. However, it may be difficult to extract such a relation due to the low number of lidar observations overlapping with MLS operation years since 2004. From meteor radar wind data, camera observations, and ground observations, we know that the southwestward wind often blows NLCs from the northeast over PFRR. By looking at the latitude data closest to PFRR at 64.7° N, it is evident that for the weaker NLCs (maximum IBC <50), most clouds are under subsaturated conditions, meaning that the meteorological conditions (specifically, temperature and humidity) at that latitude do not support stable cloud formation. A few of these weak clouds would have required amounts of water vapor that are much higher than naturally expected in the mesosphere. The saturation conditions improve as we move poleward. We conclude that the weaker clouds detected by the lidar are patches of NLC that have drifted south to warmer conditions and are not in equilibrium at the time of detection over PFRR. This may also explain why sometimes clouds are visible to the north of PFRR but do not appear overhead, even though the wind speeds are comparable to nights when NLCs have been observed. The

stability analysis helps us to understand the NLCs we have detected with lidar at Chatanika. Previously, it was assumed that an NLC detection meant that the environment was cold and wet enough for an ice cloud to be in equilibrium, and water content was even estimated based on this assumption. However, from this study and others in the field, we understand that it is possible to detect clouds which are not in equilibrium and are sublimating. Based on this study, I consider PFRR to be located in an interesting environment because it is close enough to the pole to frequently observe NLCs, but far enough south that it is not always in favorable conditions to yield NLC formation and equilibrium conditions in the mesosphere. This study has provided a framework for understanding our past NLC observations and consider the meteorology that might be playing out in future observations.

iv.) Signal Analysis of the Three-Channel Rayleigh Lidar System

I have described the RDTL three-channel receiver system and analyzed the signals in each channel using winter and summer data. I developed a new temperature and density retrieval method for the RDTL three-channel data. The new retrieval method combines the lidar signal between the channels and joins the low-altitude and high-altitude lidar signal profiles at the altitude where the vertical gradient of the ratio between the lidar signals is closest to zero. This method results in a smooth profile through the combination altitude and eliminates the discontinuity that existed in the previous method of combining the low-altitude and high-altitude temperature profiles based on the vertical gradient in relative densities. I have also developed the extension of the RDTL relative density profile by converting the sodium resonance wind temperature lidar (SRWTL)

temperature data to relative densities. Through this method, a relative density profile from ~30-120 km is created and radiosonde density data is used to yield an absolute density profile.

References

Backhouse, T. W. (1885). The luminous cirrus cloud of June and July, Meteorological Magazine, 20, 133.

Baumgarten, G., K. H. Fricke, & G. von Cossart. (2002). Investigation of the shape of noctilucent cloud particles by polarization lidar technique. Geophysical Research Letters. 29, 13.

Baumgarten, G., G. von Cossart, & J. Fiedler (2007). The size of noctilucent cloud particles above ALOMAR (69N, 16E): Optical modeling and method description, Advances in Space Research, 40, 772–784.

Berger, U. & U. von Zahn. (2007). Three-dimensional modeling of the trajectories of visible noctilucent cloud particles: An indication of particle nucleation well below the mesopause. Journal of Geophysical Research, 112, 1-10.

Björn, L.G. (1984). The cold summer mesopause. Advances in Space Research, 4, 4, 145-151.

Butler, C.J. (2006). Possible observations of noctilucent clouds by Thomas Romney Robinson. Royal Meteorological Society, 61, 5, 143-144.

Collins, R.L., M.C. Kelley, M.J. Nicolls, C. Ramos, T. Hou, T. E. Stern, K. Mizutani, & T. Itabe. (2003). Simultaneous lidar observations of a noctilucent cloud and an internal wave in the polar mesosphere. Journal of Geophysical Research 108, 8435.

Collins, R. L., M. J. Taylor, K. Nielsen, K. Mizutani, Y. Murayama, K. Sakanoi, & M. T. DeLand. (2009), Noctilucent cloud in the western Arctic in 2005: Simultaneous lidar and camera observations and analysis. Journal of Atmospheric and Solar Terrestrial Physics, 71, 446-452.

Dalin, P., et al. (2011). A comparison between ground-based observations of noctilucent clouds and Aura satellite data. Journal of Atmospheric and Solar Terrestrial Physics, 73, 2097-2109.

Deland, M. T., & G. E. Thomas, G.E. (2019). Evaluation of Space Traffic Effects in SBUV Polar Mesospheric Cloud Data. Journal of Geophysical Research- Atmospheres, 124, 4203-4221.

Deland, M.T., E. P. Shettle, G. E. Thomas, & J. J. Olivero. (2007). Latitude-dependent long-term variations in polar mesospheric clouds from SBUV version 3 PMC data. Journal of Geophysical Research, 112, D10315, doi:10.1029/2006JD007857.

Deland, M.T., E. P. Shettle, & G.E. Thomas. (2006). A quarter-century of satellite PMC observations. Journal of Atmospheric and Solar Terrestrial Physics, 68, 1, 9-29.

Donahue, T. M., B. Guenther, & J. E. Blamont. (1972). Noctilucent clouds in daytime: circumpolar particulate layers near the summer mesopause. Journal of the Atmospheric Sciences 29, 1205–1209.

Fiedler, J. & G. Baumgarten. (2018). Solar and lunar tides in noctilucent clouds as determined by ground-based lidar. Atmospheric Chemistry and Physics, 18, 16051-16061.

Fogle, B. T. (1966). Noctilucent Clouds, Ph.D. Dissertation, University of Alaska Fairbanks.

Fogle, B.T. (1964). Noctilucent clouds in the southern hemisphere, Nature, 204, 14-18.

Hamamatsu Photonics K.K. (2007). Photomultiplier Tubes. Retrieved from https://www.hamamatsu.com/resources/pdf/etd/PMT_handbook_v3aE.pdf.

Hansen, G., M. Serwazi, & U. von Zahn. (1989). First detection of a noctilucent cloud by lidar. Geophysical Research Letters, 16, 12, 1445-1448.

Hervig, M., R. E. Thompson,M. McHugh, L. L. Gordley, & G. M. Russell III. (2001). First confirmation that water ice is the primary component of polar mesospheric clouds. Geophysical Research Letters, 28, 971-974

Hervig, M. E., U. Berger, & D.E. Siskind. (2016). Decadal variability in PMCs and implications for changing temperature and water vapor in the upper mesosphere. Journal of Geophysical Research, 121, 2383-2392.

Holton, J. R., & M. J. Alexander. (2000), The role of waves in the transport circulation of the middle atmosphere, Atmospheric Science Across the Stratopause, *123*, 21–35.

Hultgren, K. & J. Gumbel. (2014). Tomographic and spectral views on the lifecycle of polar mesospheric clouds from Odin/OSIRIS. Journal of Geophysical Research: Atmospheres.

Jensen, E.J., G. E. Thomas. (1994). Numerical simulations of the effects of gravity waves on noctilucent clouds. Journal of Geophysical Research, 99 (D2), 3421–3430.

Jesse, O. (1889). Die leuchtenden Nachtwolken. Astronomische Nachrichten, 121, 7.

Jesse, O. (1896). Die Höhe der leuchtenden Nachtwolken. Astronomische Nachrichten, 140, 3347.

Kelley, M.C. et al. (2010). Radar, lidar, and optical observations in the polar summer mesosphere shortly after a space shuttle launch, Journal of Geophysical Research, 115, A05304, doi:10.1029/2009JA014938.

Kirkwood, S., & K. Stebel. (2003). Influence of planetary waves on noctilucent clouds occurrence over NW Europe. Journal of Geophysical Research, 108, 8440.

Leslie, R.C. (1885). Sky glows. Nature 32, 245.

Li, J. (2019). Lidar and Radar Studies of Turbulence, Instabilities, and Waves in the Arctic Middle Atmosphere. (Ph.D. dissertation), University of Alaska Fairbanks.

Livesey, N.J., et al. (2018). Version 4.2x Level 2 data quality and description document. JPL, D-33509 Rev. D.

Lübken, F.-J. (1999). Thermal structure of the Arctic summer mesosphere. Journal of Geophysical Research, 104(D8), 9135-9149.

Lübken, F-J. (2018). On the anthropogenic impact on long-term evolution of noctilucent clouds, Geophysical Research Letters 45, 6681-6689.

McClintock, W.E., et al. (2009). The cloud imaging and particle size experiment on the Aeronomy of Ice in the mesosphere mission: Instrument concept, design, calibration, and on-orbit performance, Journal of Atmospheric and Solar-Terrestrial Physics, 71, 340-355.

Merkel, A.W., Rusch, D.W., Palo, S.E., Russell III, J.M., & Bailey, S.M. 2009, Mesospheric planetary wave effects on global PMC variability inferred from AIM-CIPS and TIMED-SABER for the northern summer 2007 PMC season. Journal of Atmospheric and Solar Terrestrial Physics. 71, 381-391.

Mizutani, K. T. Itabe, M. Yasui, T. Aoki, Y. Murayama, & R.L. Collins. (2000). Rayleigh and Rayleigh Doppler lidars for the observations of the Arctic middle atmosphere, IEICE Transactions on Fundamentals of Electronics, Communications & Computer Sciences, E83-B, 2003.

Morris, R., & D. Murphy. (2008). The polar mesosphere. Physics Education, 43, 366.

Murphy, D.M., & T. Koop. (2005). Review of the vapour pressure of ice and supercooled water for atmospheric applications. Quarterly Journal of the Royal Meteorological Society, 131, 1539-1565.

MSIS. (2019), Virtual Ionosphere, Thermosphere, Mesosphere Observatory (VITMO) MSIS-E-90 Atmosphere Model, Accessed in 2019, Available at http://omniweb.gsfc.nasa.gov/vitmo/msis_vitmo.html

Papoulis, A. (1984), Probability, random variables, and stochastic processes, 576, McGraw-Hill, New York.

Randel, W., P. Udelhofen, E. Fleming, M. Geller, M. Gelman, K. Hamilton, D. Karoly, D. Ortland, S. Pawson, R. Swinbank, F. Wu, M. Baldwin, M.-L. Chanin, P. Keckhut, K.

Labitzke, E. Remsberg, A. Simmons, and D. Wu. (2004). The SPARC intercomparison of middle-atmosphere climatologies, Journal of Climate, 17(5), 986-1003.

Rapp, M., & G. E. Thomas. (2006). Modeling the microphysics of mesospheric ice particles: Assessment of current capabilities and basic sensitivities. Journal of Atmospheric and Solar-Terrestrial Physics, 68, 715-744.

Rapp, M., F.-J Lübken, A. Müllemann, G. E. Thomas, & E. Jensen. (2002). Smallscale temperature variations in the vicinity of NLC: experimental and model results. Journal of Geophysical Research, 107, 4392.

Russell., J.M., III, et al. (2009). Aeronomy of Ice in the Mesosphere (AIM): Overview and early science results, Journal of Atmospheric and Solar-Terrestrial Physics, 71, 289-299.

Schröder, W. (1999). Were Noctilucent Clouds Caused by the Krakatoa Eruption? A Case Study of the Research Problems before 1885. Journal of the American Meteorological Society, 80, 10, 2081-2086.

Schröder, W. (1968). Zur Charakteristik der Leuchtenden Nachtwolken wahrend der Jahre 1963-1967. Gerlands Beitr. Geophysiks. 77, 441.

SPARC. (2002), SPARC intercomparison of middle atmosphere climatologies, SPARC Rep 3., 96 pp.

Stevens, M. H., R. R. Meier, X. Chu, M. T. DeLand, & J. M. C. Plane. (2005), Antarctic mesospheric clouds formed from space shuttle exhaust, Geophysical Research Letters, 32, L13810

Stevens, M. H., J. Gumbel, C. R. Englert, K. U. Grossmann, M. Rapp, & P. Hartogh. (2003). Polar mesospheric clouds formed from space shuttle exhaust, Geophysical Research Letters, 30, 1546, doi:10.1029/2003GL017249.

Strutt, J. W. (Lord Rayleigh). (1899). On the transmission of light through an atmosphere containing small particles in suspension, and on the origin of the blue of the sky, Philosophical Magazine 48, 375-384.

Taylor, M.J. et al. (2002). Mesospheric cloud observations at unusually low latitudes, Journal of Atmospheric and Solar-Terrestrial Physics, 64, 991-999

Theon, JS, & W. Nordberg. (1967). Temperature measurements in noctilucent clouds. Science, 157.

Thomas, G.E. (1996). Global change in the mesosphere-lower thermosphere region: has it already arrived? Journal of Atmospheric and Solar-Terrestrial Physics., 58, 1629-1656.

Thomas, G.E., J.J. Olivero, & E.J. Jensen. (1989). Relation between increasing methane and the presence of ice clouds at the mesopause. Nature, 338, 490-492.

Thurairajah, B., R. L. Collins, & K. Mizutani. (2009). Multi-year temperature measurements of the middle atmosphere at Chatanika, Alaska (65°N, 147°W), Earth, Planets and Space, 61(6), 755-764.

Triplett, C. C., J. Li, R. L. Collins, G. A. Lehmacher, A. Barjatya, D. C. Fritts, et al. (2018). Observations of Reduced Turbulence and Wave Activity in the Arctic Middle Atmosphere Following the January 2015 Sudden Stratospheric Warming. Journal of Geophysical Research, 123(23), 13,259-213,276. doi:10.1029/2018JD028788

Triplett, C. (2016). Rocket and Lidar Studies of Waves and Turbulence in the Arctic Middle Atmosphere. (Ph. D. dissertation), University of Alaska Fairbanks.

UWYO Dpt. of Atmospheric sciences (2019), Sounding Data, Accessed in 2019. Available at http://weather.uwyo.edu/upperair/sounding.html.

Vestine, E.H. (1934). Noctilucent Clouds. The Journal of The Royal Astronomical Society of Canada, 28, 249.

Witt, G. (1962). Height, structure and displacements of noctilucent clouds, Tellus, 14:1, 1-18.

Woodhouse, Iain. (2006) Introduction to Microwave Remote Sensing. CRC Press, Taylor & Francis.

Appendix A. False Color Plots of Noctilucent Clouds at Chatanika

A.1. Introduction

False color plots of backscatter ratio and backscatter coefficient with time and altitude are provided here for 21 noctilucent clouds (NLCs) detected by Rayleigh lidar at Poker Flat Research Range in Chatanika, Alaska from July 31-August 20 of 1998-2019. The lidar signal was processed through a 6000 laser pulse integration. The 21 NLCs have significant IBC values (IBC>3ΔIBC) at the 6000 pulse resolution. The time is given in Local Standard Time (UT-9 h). Plots of backscatter ratio for each observation are shown on the left panel. Plots of backscatter coefficient for each observation are shown on the right panel in units of $x10^{-10}$ m^{-1} sr^{-1}. The 21 nights of significant NLC observations are: August 4-5, 1999; August 16-17, 2001; August 20-21, 2001; August 3-4, 2002; August 6-7, 2003; August 9-10, 2005; August 18-19, 2005; August 1-2, 2006; August 2-3, 2006; August 8-9, 2006; August 10-11, 2007; August 16-17, 2007; July 31-August 1, 2010; August 3-4, 2010; August 8-9, 2012; August 10-11, 2012; August 13-14, 2012; August 6-7, 2013; August 10-11, 2018; August 7-8, 2019; and August 11-12, 2019.

The 20 nights of lidar observations from July 31-August 31 of 1999-2019 that did not detect an NLC are: August 31-September 1, 1999; August 14-15, 2002; August 27-28, 2002; August 7-8, 2003; August 29-30, 2003; August 8-9, 2005; August 10-11, 2005; August 5-6, 2006; August 8-9, 2007; August 9-10, 2007; August 11-12, 2008; August 19-20, 2008; August 11-12, 2009; August 21-22, 2010; August 11-12, 2011; August 18-19, 2011; August 3-4, 2015; August 5-6, 2017; July 31-August 1, 2018; and August 19-20, 2019.

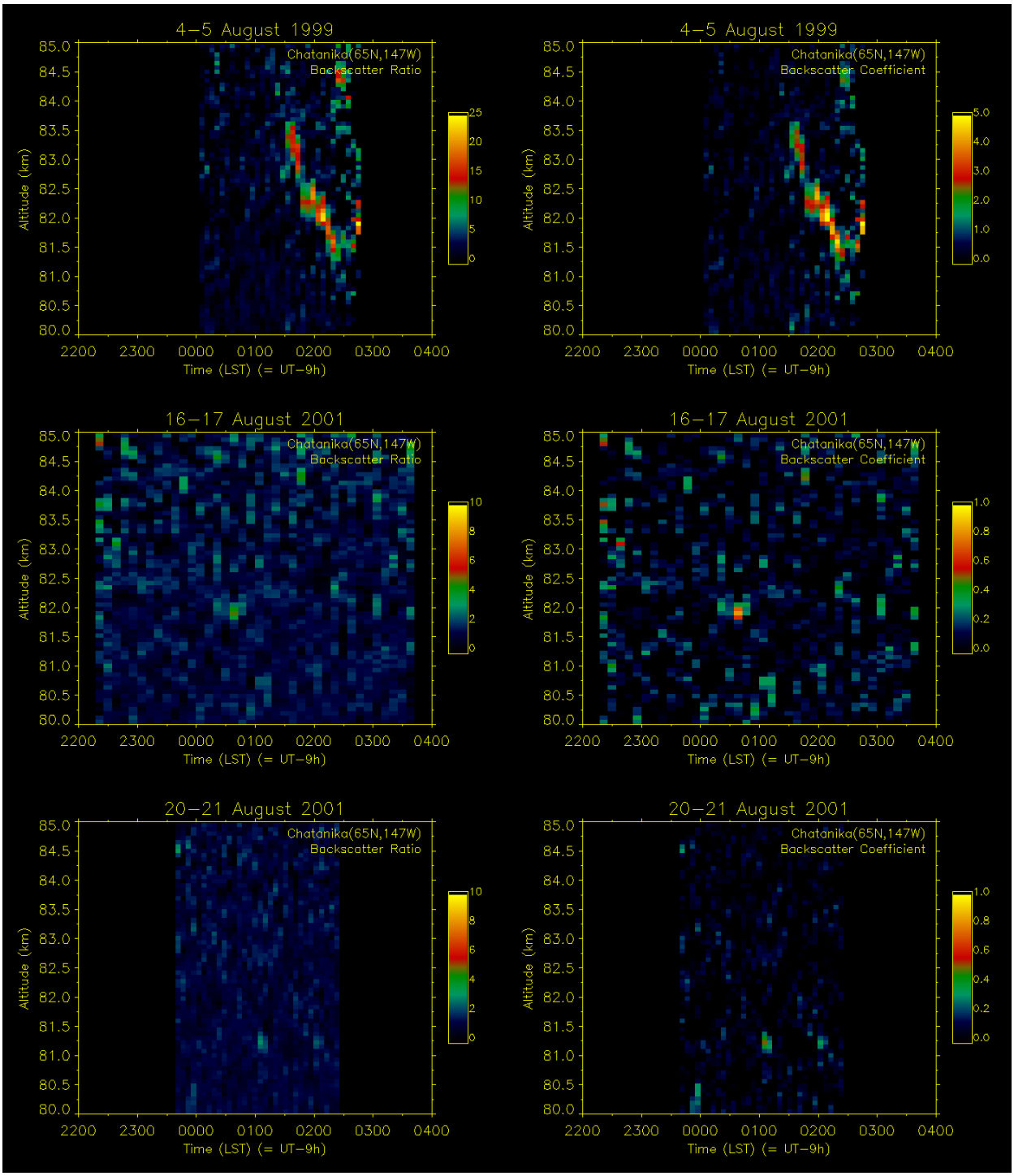

Figure A.1a. (top left) Backscatter ratio on August 4-5, 1999. Figure A.1b. (top right) Backscatter coefficient on August 4-5, 1999. Figure A.2a. (middle left) Backscatter ratio on August 16-17, 2001. Figure A.2b. (middle right) Backscatter coefficient on August 16-17, 2001. Figure A.3a. (bottom left) Backscatter ratio on August 20-21, 2001. Figure A.3b. (bottom right) Backscatter coefficient on August 20-21, 2001.

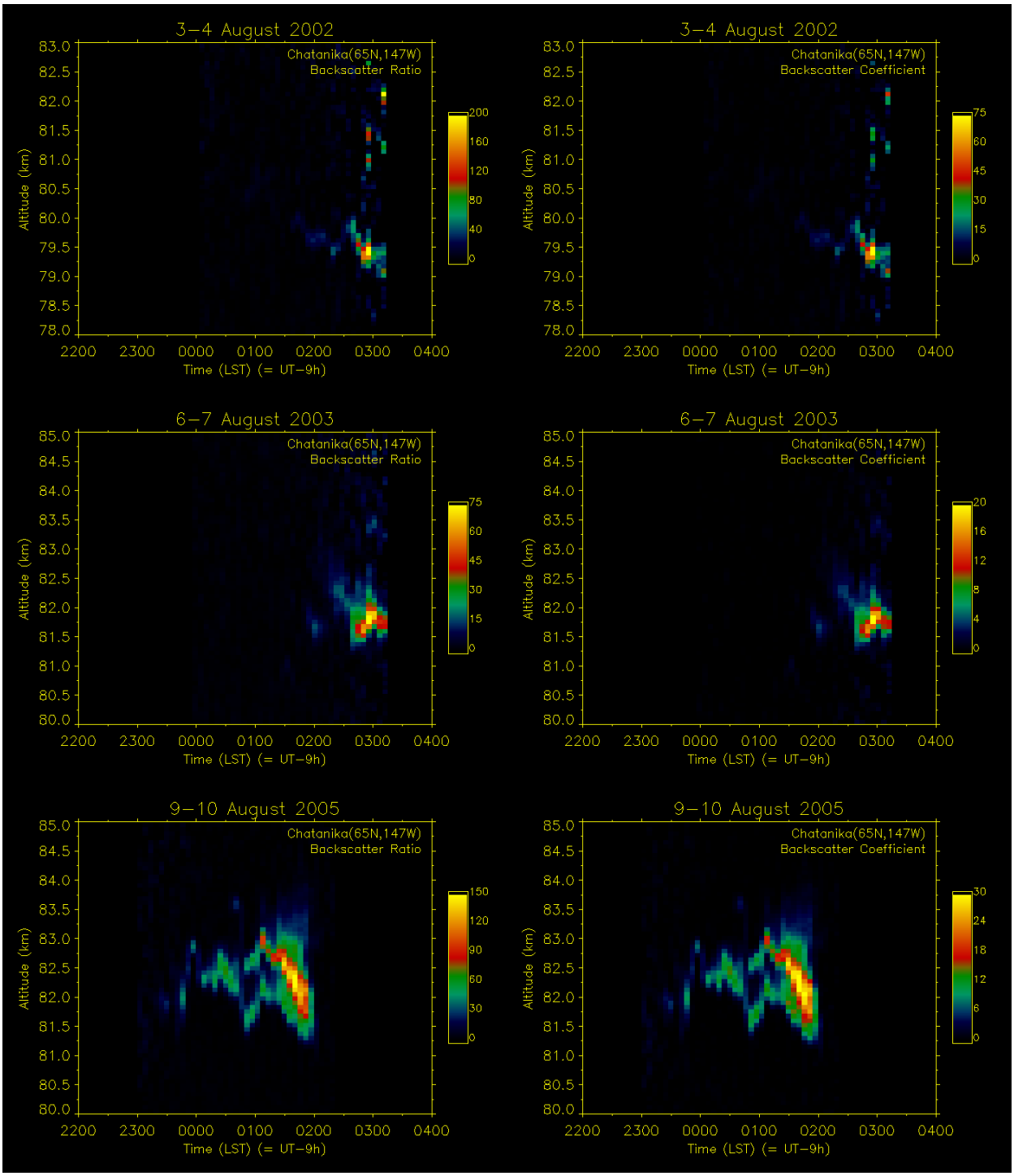

Figure A.4a. (top left) Backscatter ratio on August 3-4, 2002. Figure A.4b. (top right) Backscatter coefficient on August 3-4, 2002. Figure A.5a. (middle left) Backscatter ratio on August 6-7, 2003. Figure A.5b. (middle right) Backscatter coefficient on August 6-7, 2003. Figure A.6a. (bottom left) Backscatter ratio on August 9-10, 2005. Figure A.6b. (bottom right) Backscatter coefficient on August 9-10, 2005.

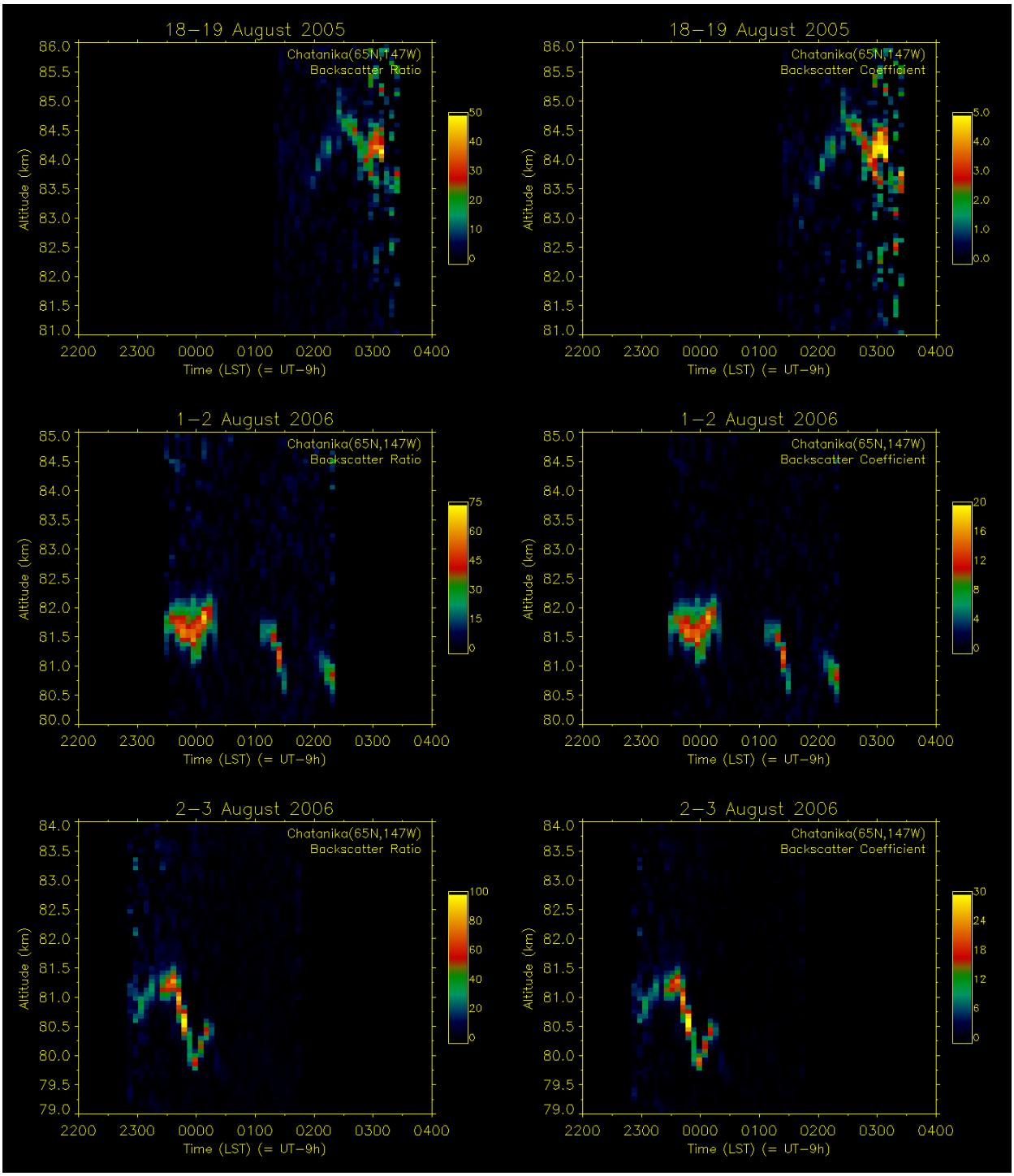

Figure A.7a. (top left) Backscatter ratio on August 18-19, 2005. Figure A.7b. (top right) Backscatter coefficient on August 18-19, 2005. Figure A.8a. (middle left) Backscatter ratio on August 1-2, 2006. Figure A.8b. (middle right) Backscatter coefficient on August 1-2, 2006. Figure A.9a. (bottom left) Backscatter ratio on August 2-3, 2006. Figure A.9b. (bottom right) Backscatter coefficient on August 2-3, 2006.

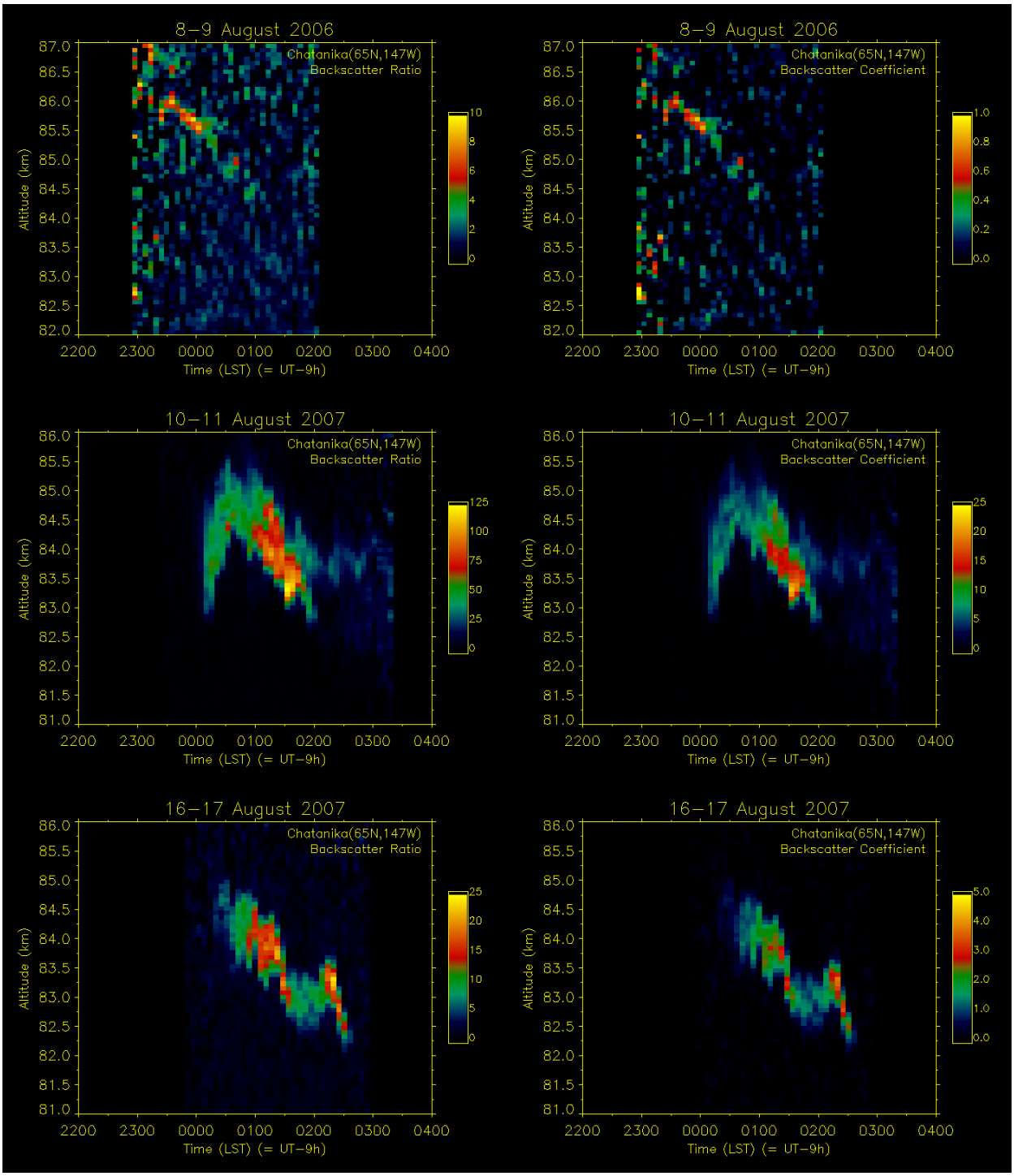

Figure A.10a. (top left) Backscatter ratio on August 8-9, 2006. Figure A.10b. (top right) Backscatter coefficient on August 8-9, 2006. Figure A.11a. (middle left) Backscatter ratio on August 10-11, 2007. Figure A.11b. (middle right) Backscatter coefficient on August 10-11, 2007. Figure A.12a. (bottom left) Backscatter ratio on August 16-17, 2007. Figure A.12b. (bottom right) Backscatter coefficient on August 16-17, 2007.

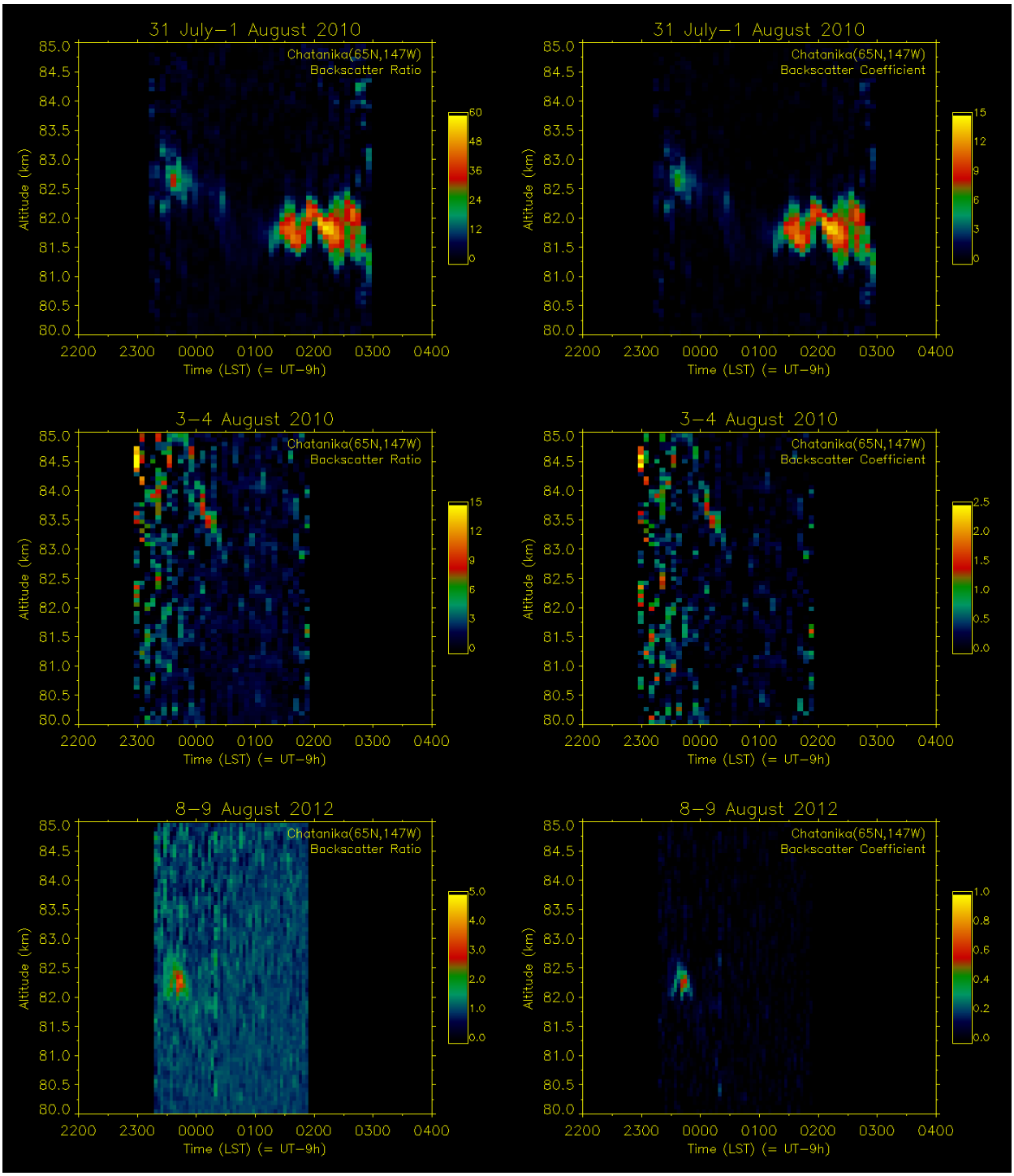

Figure A.13a. (top left) Backscatter ratio on July 31-August 1, 2010. Figure A.13b. (top right) Backscatter coefficient on July 31-August 1, 2010. Figure A.14a. (middle left) Backscatter ratio on August 3-4, 2010. Figure A.14b. (middle right) Backscatter coefficient on August 3-4, 2010. Figure A.15a. (bottom left) Backscatter ratio on August 8-9, 2012. Figure A.15b. (bottom right) Backscatter coefficient on August 8-9, 2012.

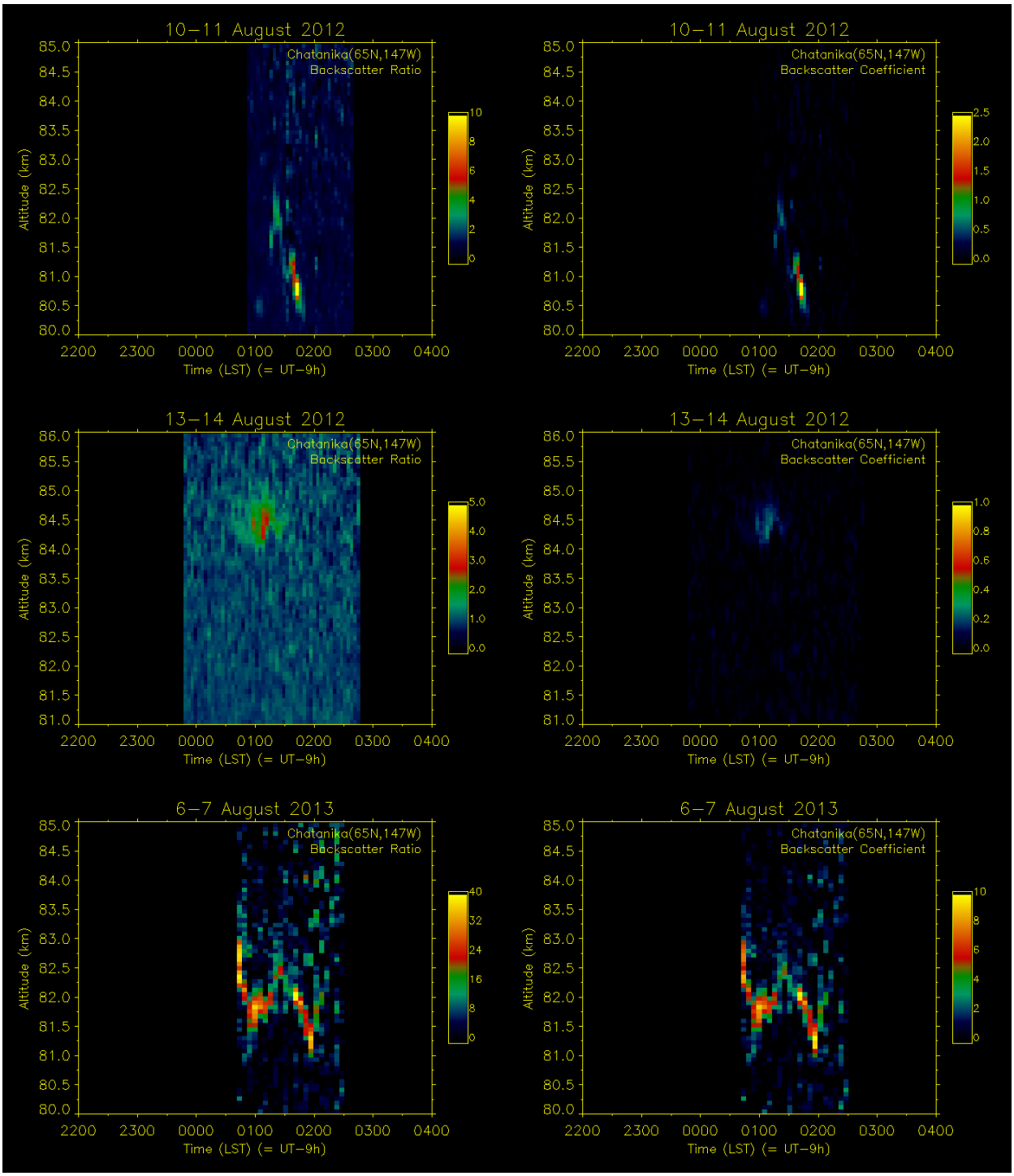

Figure A.16a. (top left) Backscatter ratio on August 10-11, 2012. Figure A.16b. (top right) Backscatter coefficient on August 10-11, 2012. Figure A.17a. (middle left) Backscatter ratio on August 13-14, 2012. Figure A.17b. (middle right) Backscatter coefficient on August 13-14, 2012. Figure A.18a. (bottom left) Backscatter ratio on August 6-7, 2013. Figure A.18b. (bottom right) Backscatter coefficient on August 6-7, 2013.

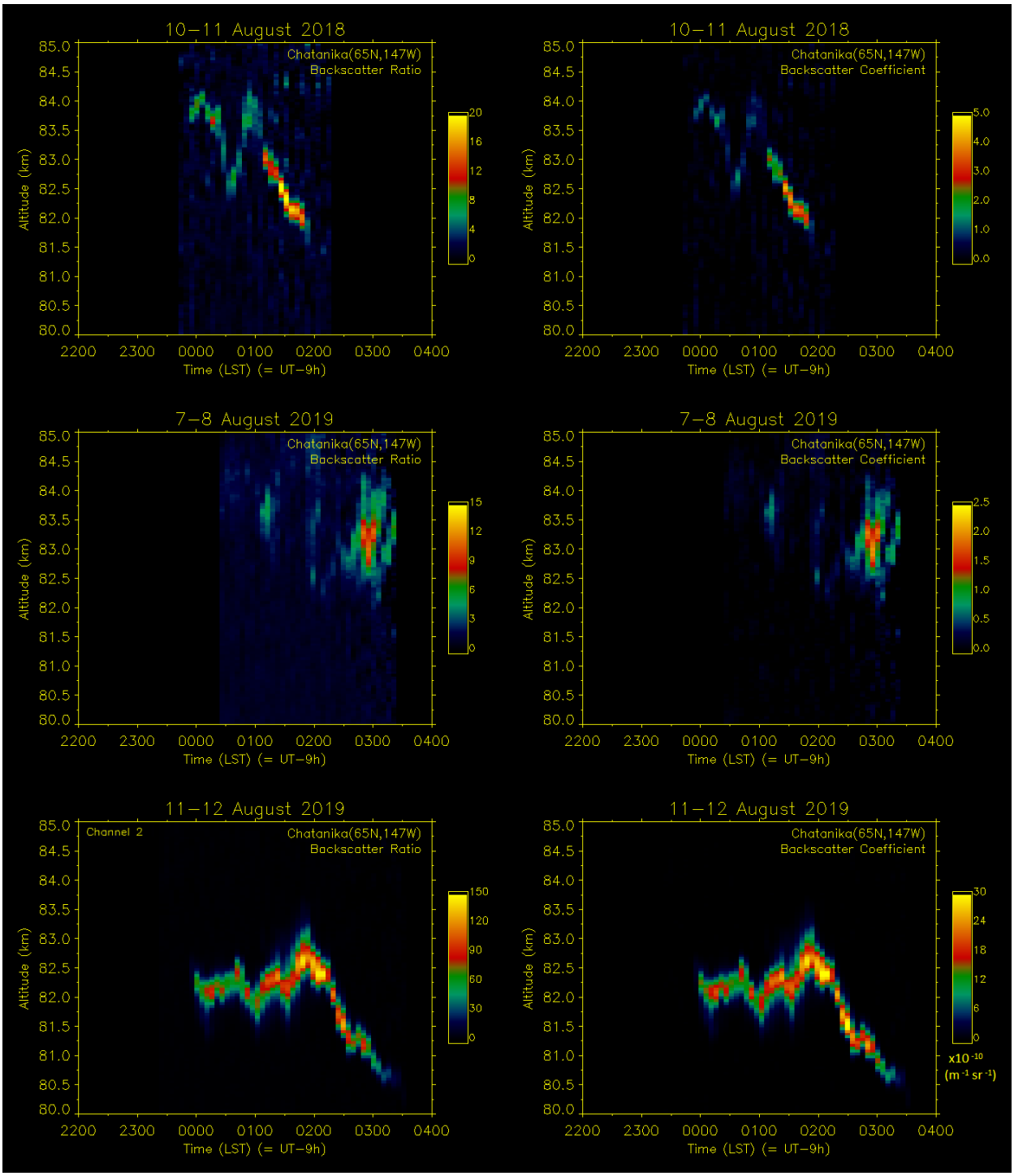

Figure A.19a. (top left) Backscatter ratio on August 10-11, 2018. Figure A.19b. (top right) Backscatter coefficient on August 10-11, 2018. Figure A.20a. (middle left) Backscatter ratio on August 7-8, 2019. Figure A.20b. (middle right) Backscatter coefficient on August 7-8, 2019. Figure A.21a. (bottom left) Backscatter ratio on August 11-12, 2019. Figure A.21b. (bottom right) Backscatter coefficient on August 11-12, 2019.

Appendix B. Comparison of Rayleigh Scatter Signal Fitting Methods

B.1. Introduction

As described in Chapter 2, it is necessary to estimate the Rayleigh scatter signal for lidar observations of NLCs since the signal in the cloud altitude region is due to both Rayleigh scatter and aerosol scatter. While analyzing the lidar data presented in this thesis, it was discovered that a fitting method previously used to estimate the Rayleigh scatter signal causes an underestimate in the backscatter ratio. The fitting method used prior to November 2019 was a linear fit over the natural logarithm of the summed lidar signal from 68-72 km. The linear fit was extrapolated upwards to 90 km. This linear fit was not a good fit over the high altitudes (80-90 km) and cut above the base of the cloud signal. This caused some of very weak NLC observations to have no significant (>3ΔIBC) IBC values even though NLC signatures were present in the raw signal profiles.

To attain a more accurate estimate, a new fitting method was established. In this method, a third-order polynomial is fit over the natural logarithm of the summed signal from 60-90 km, excluding the cloud altitude region (80-85 km). This method results in a more accurate estimate of the Rayleigh scatter signal. A comparison of the two fitting methods for 20 NLC lidar detections is provided here. The NLC detection on August 6-7, 2013 is excluded since a unique linear extrapolated fitting was performed from 60-64 km due to the low-quality signal during the observation. For each of the figures below, the red profile is the range-scaled summed lidar signal. The white profile is the de-range-scaled summed lidar signal. The linear fit and the third-order polynomial fit are shown for both the range-scaled and de-range-scaled profiles. At the bottom of each plot, the peak fit ratio is given. The peak fit ratio is the ratio between the Rayleigh scatter signal

estimated by the polynomial fit (P) and the Rayleigh scatter signal estimated by the linear extrapolated fit (E) at the altitude where the peak backscatter ratio occurs.

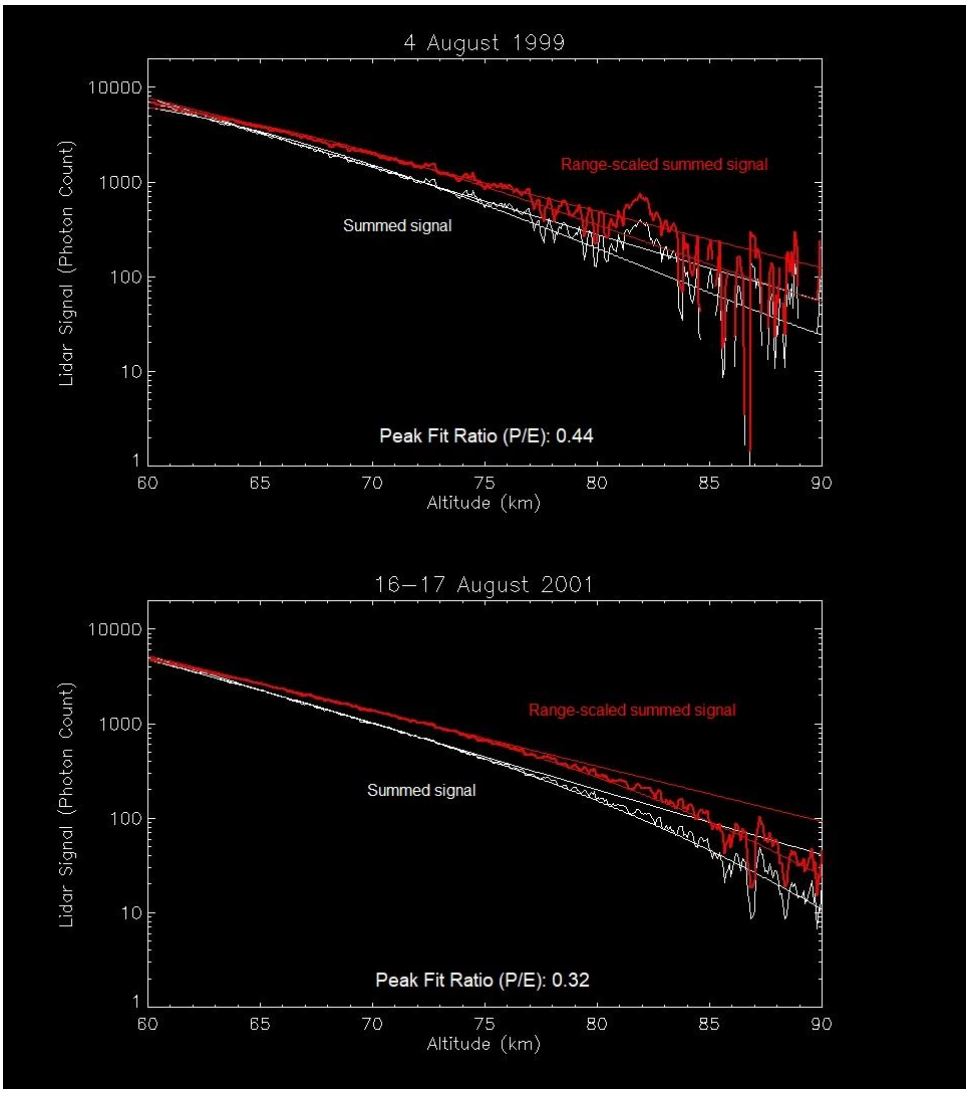

Figure B.1. (top) Rayleigh signal fitting method comparison for August 4-5, 1999. Figure B.2. (bottom) Rayleigh signal fitting method comparison for August 16-17, 2001.

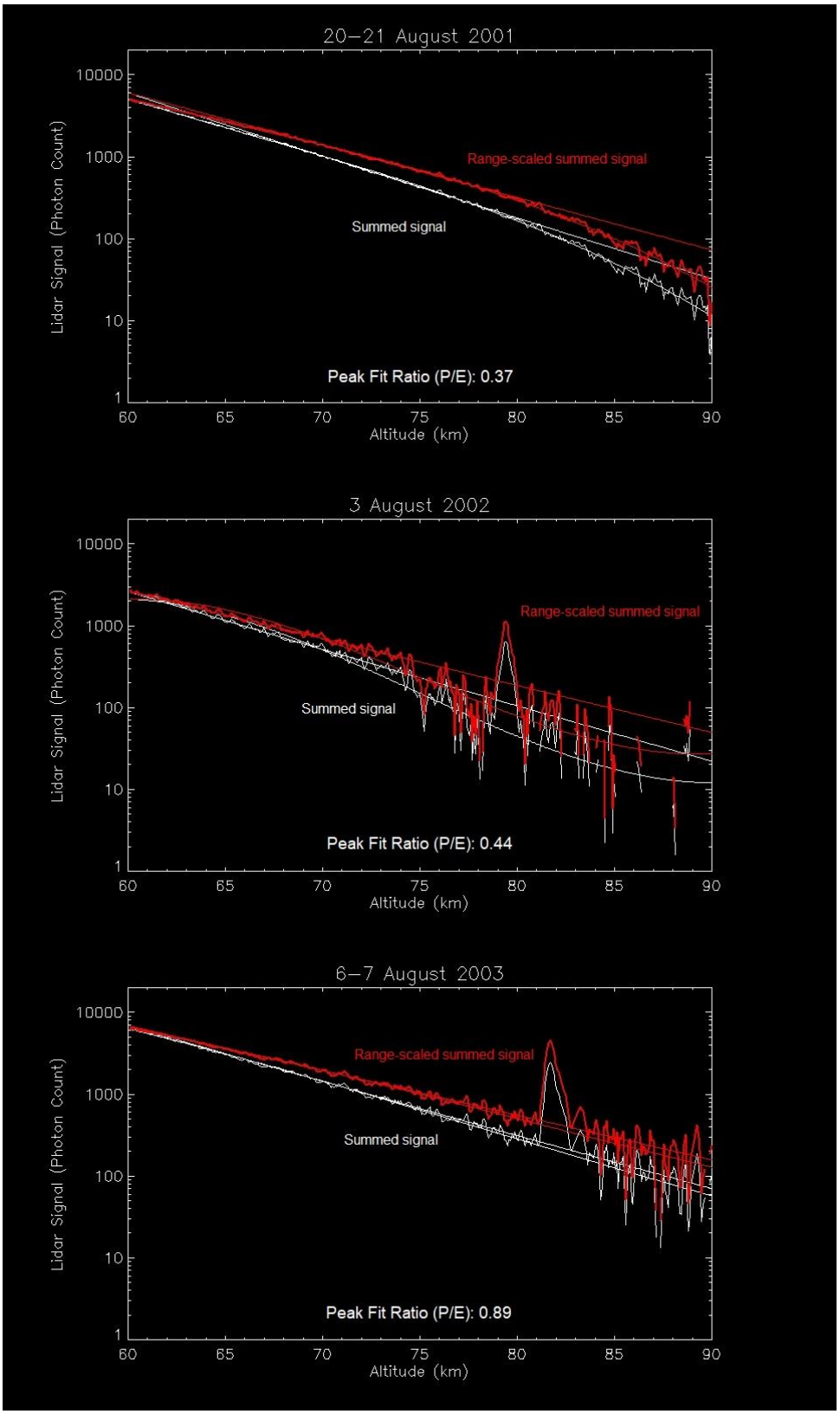

Figure B.3. (top) Rayleigh signal fitting method comparison for August 20-21, 2001. Figure B.4. (middle) Rayleigh signal fitting method comparison for August 3-4, 2002. Figure B.5. (bottom) Rayleigh signal fitting method comparison for August 6-7, 2003.

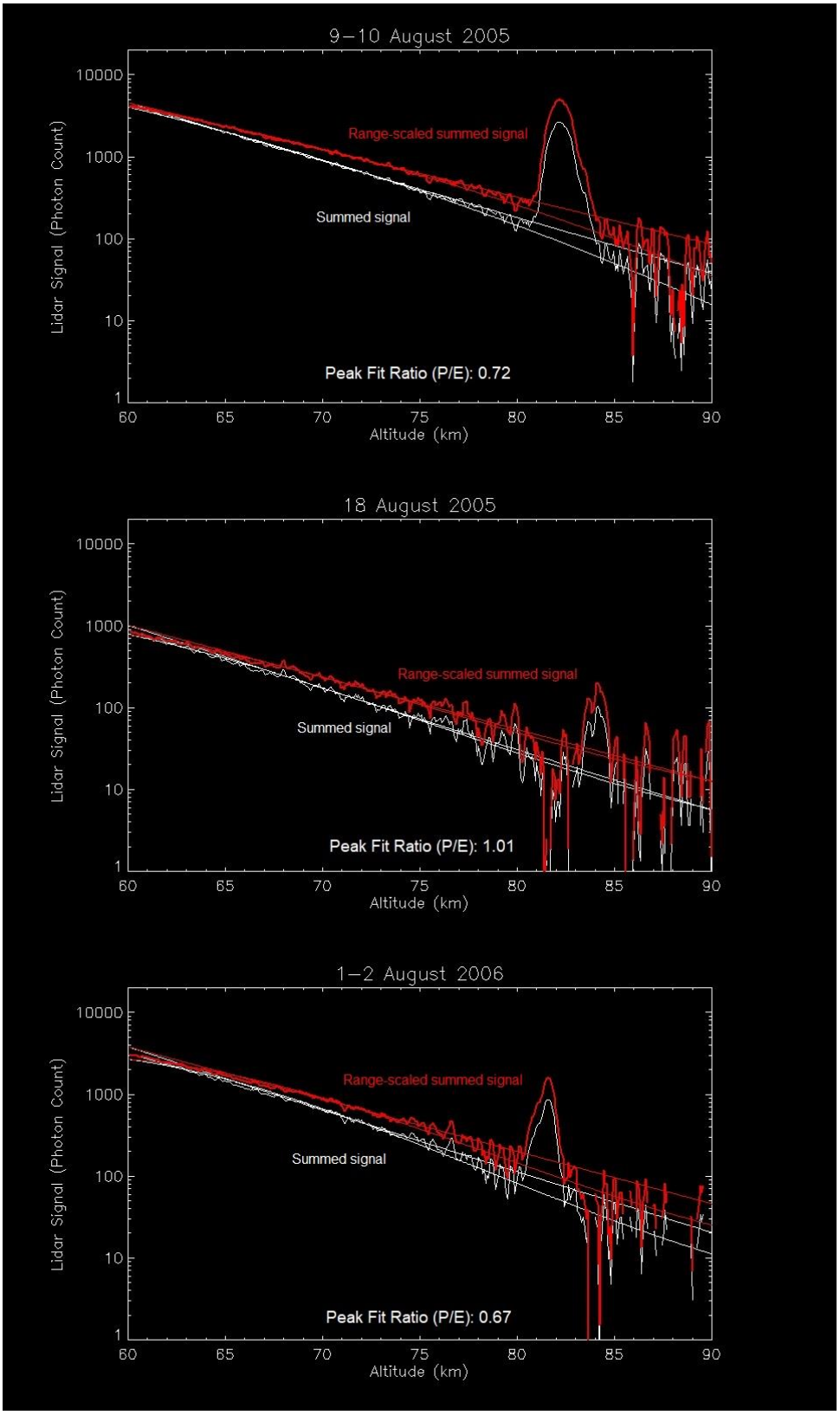

Figure B.6. (top) Rayleigh signal fitting method comparison for August 9-10, 2005. Figure B.7. (middle) Rayleigh signal fitting method comparison for August 18-19, 2005. Figure B.8. (bottom) Rayleigh signal fitting method comparison for August 1-2, 2006.

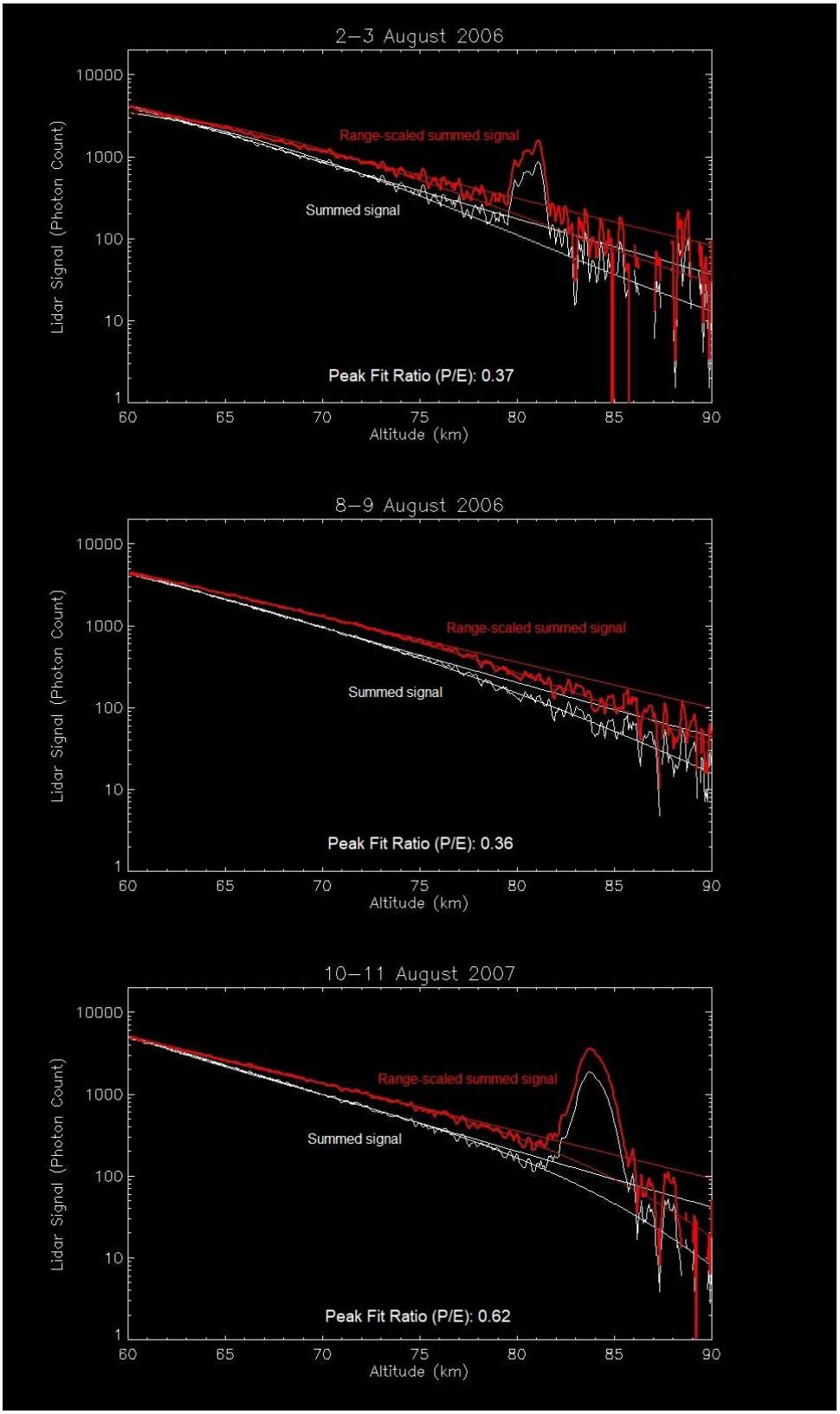

Figure B.9. (top) Rayleigh signal fitting method comparison for August 2-3, 2006. Figure B.10. (middle) Rayleigh signal fitting method comparison for August 8-9, 2006. Figure B.11. (bottom) Rayleigh signal fitting method comparison for August 10-11, 2007.

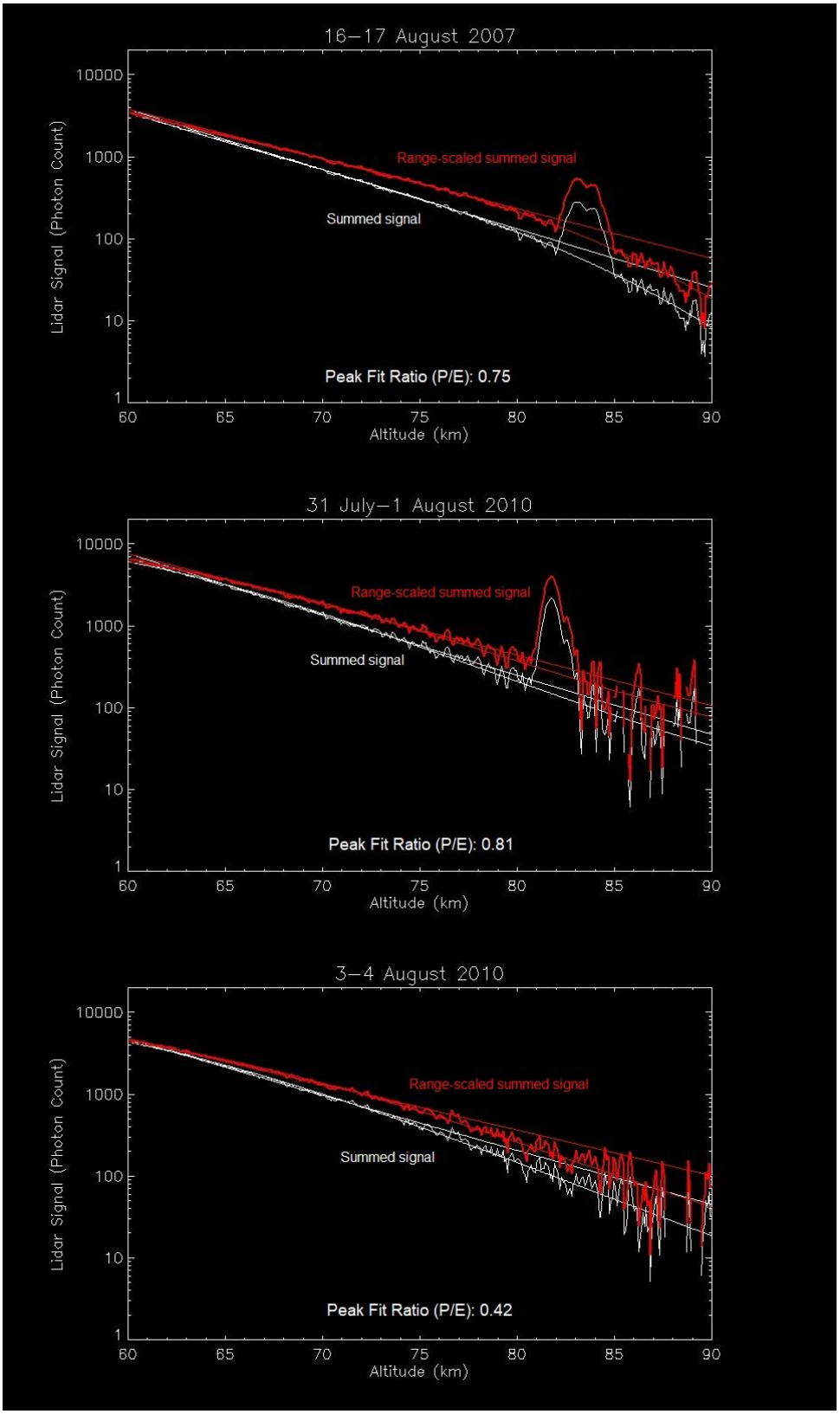

Figure B.12. (top) Rayleigh signal fitting method comparison for August 16-17, 2007. Figure B.13. (middle) Rayleigh signal fitting method comparison for July 31- August 1, 2010. Figure B.14. (bottom) Rayleigh signal fitting method comparison for August 3-4, 2010.

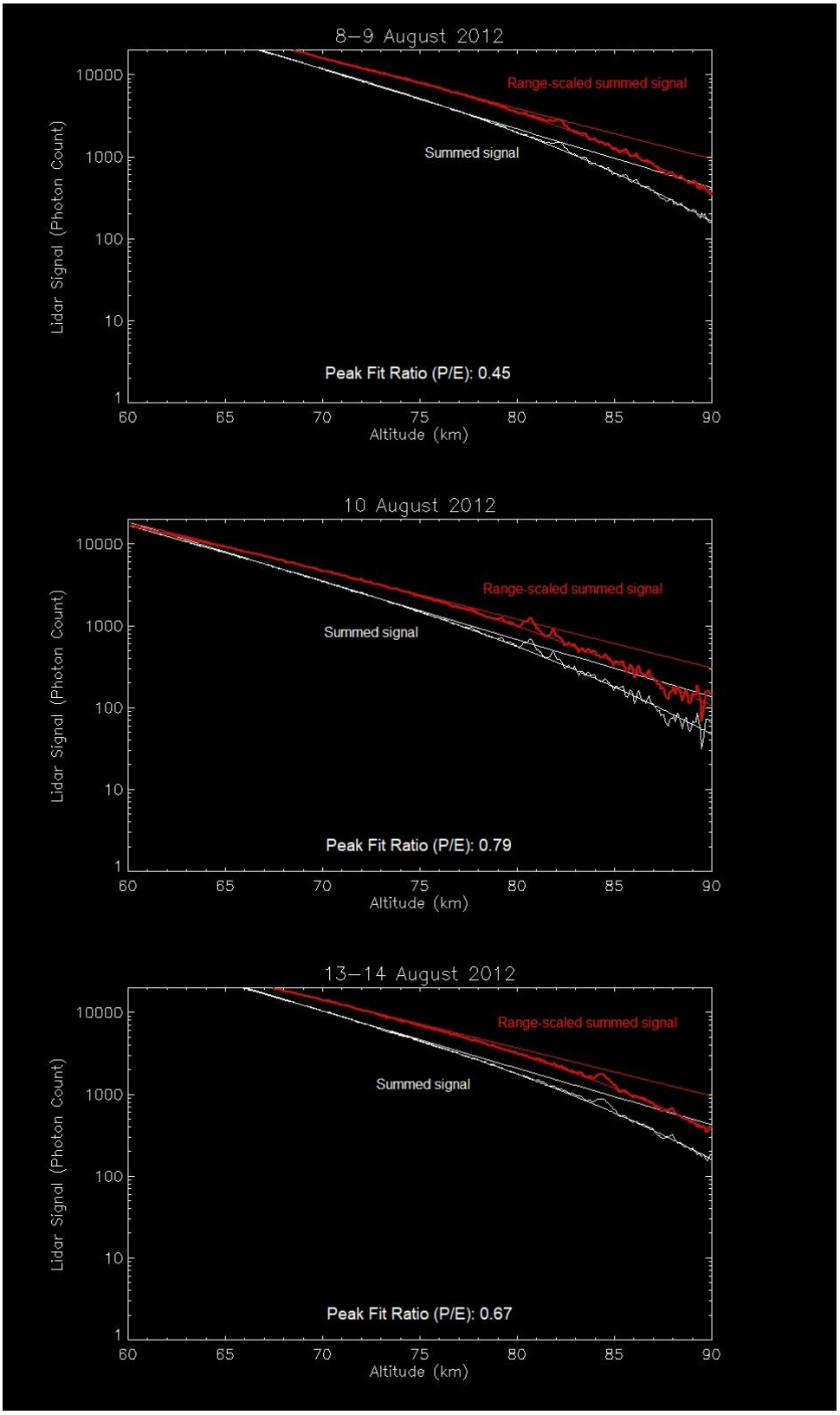

Figure B.15. (top) Rayleigh signal fitting method comparison for August 8-9, 2012. Figure B.16. (middle) Rayleigh signal fitting method comparison for August 10-11, 2012. Figure B.17. (bottom) Rayleigh signal fitting method comparison for August 13-14, 2012.

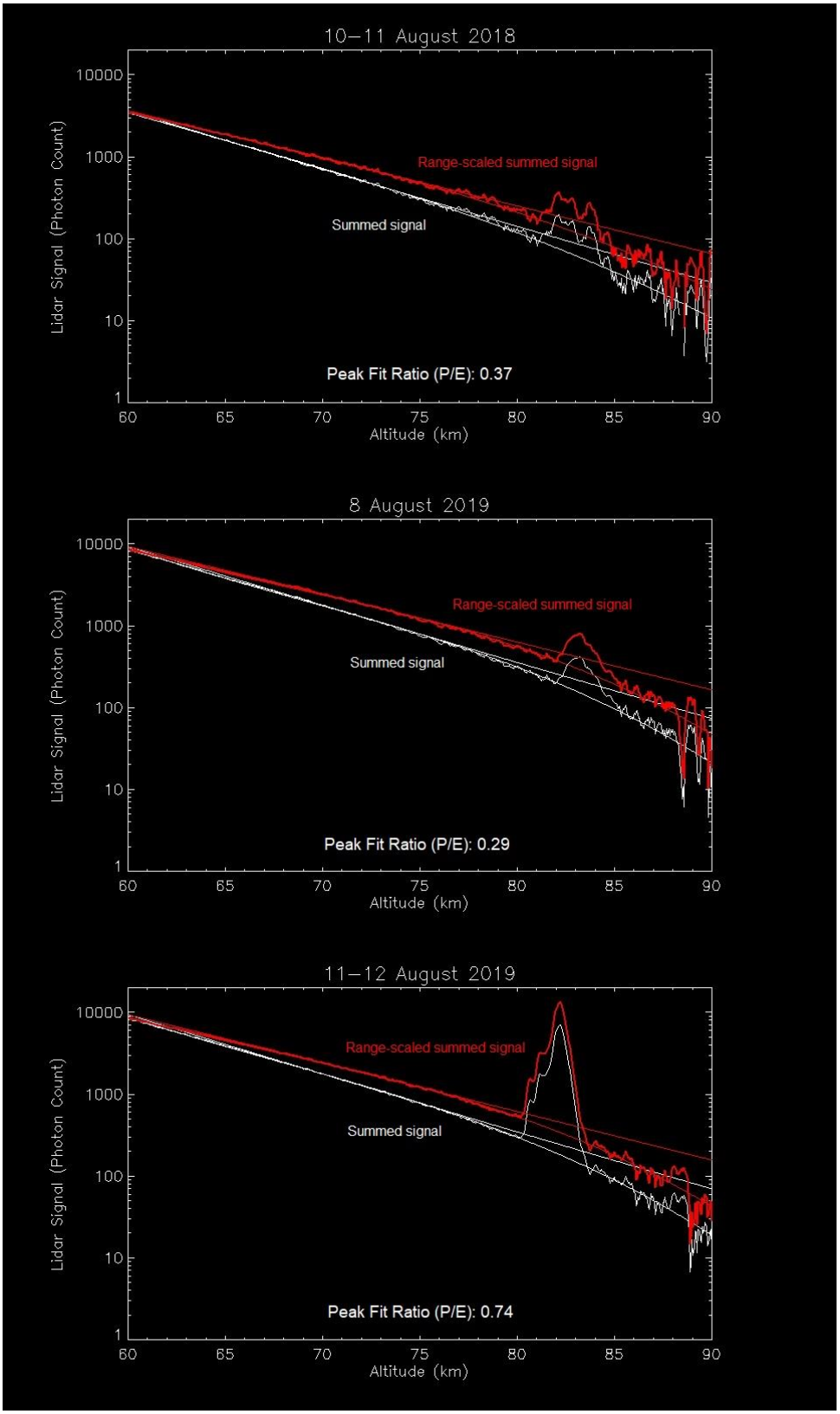

Figure B.18. (top) Rayleigh signal fitting method comparison for August 10-11, 2018. Figure B.19. (middle) Rayleigh signal fitting method comparison for August 7-8, 2019 (Channel 2). Figure B.20. (bottom) Rayleigh signal fitting method comparison for August 11-12, 2019 (Channel 2).